

Measurement of the spin structure function g_1^D of the deuteron and its moments at low Q^2

Krishna P. Adhikari, Sebastian E. Kuhn,
Alexander Deur, Lamiaa El Fassi, Hyekoo Kang, Sarah K. Phillips,
Marco Ripani, Karl Slifer, Raffaella De Vita, Gail E. Dodge,
Xiaochao Zheng

March 4, 2017

Contents

1	Introduction	4
1.1	Inclusive Electron Scattering	7
1.1.1	Kinematic Variables	7
1.1.2	Differential Cross Section and Structure Functions . . .	9
1.2	Moments of g_1 and Sum Rules	10
1.2.1	First moment Γ_1 of g_1	11
1.2.2	Generalized GDH Integral	13
1.2.3	Generalized Forward Spin Polarizability γ_0	15
2	EG4 run	17
3	Data Analysis Procedure	21
3.1	Raw Data Processing - Calibration and Reconstruction	22
3.2	Helicity States	24
3.3	Electron Identification	24
3.3.1	Electromagnetic Calorimeter Cuts	26
3.3.2	Cerenkov Counter Cuts	35
3.3.3	Minimum/Maximum Momentum cuts	41
3.3.4	Vertex-Z cuts	42
3.3.5	Fiducial Cuts	44
3.4	Data Quality and Stability Checks	51
3.5	Kinematic Corrections	54
3.5.1	Incoming Energy Loss Correction	54
3.5.2	Tracking Corrections	55
3.5.3	Momentum Correction	62
3.5.4	Outgoing Ionization Loss Correction	66
3.6	Cerenkov Counter (CC) Efficiency	67
3.6.1	Procedure	69

3.7	Pion Contamination Corrections	74
3.7.1	Method	74
3.8	e^+e^- -Pair Symmetric Contamination Corrections	77
3.9	Study of NH_3 Contamination of EG4 ND_3 Target	79
3.9.1	Procedure	79
3.9.2	Event Selection	80
3.9.3	Extracting the Contamination	82
3.9.4	Results and Conclusion	83
4	Monte Carlo Simulations and Extraction of g_1 and A_1F_1	85
4.1	Simulation and Approach to Analysis	85
4.1.1	Outline of the method	88
4.2	Radiative Corrections	90
4.3	“Standard” simulation	90
4.3.1	RCSSLACPOL	91
4.3.2	Event Generator	91
4.3.3	GSIM - CLAS Detector Simulation	94
4.3.4	GSIM POST PROCESSOR (GPP)	94
4.3.5	Finding the width of the real CLAS data elastic peak. .	97
4.4	Comparison of Data and Simulation	101
4.5	Method to Extract g_1 and A_1F_1	110
4.5.1	‘Variation’ of the standard simulation	110
5	Systematic Uncertainties	115
5.1	Model uncertainties	118
5.2	Combining uncertainties	120
5.2.1	Combining uncertainties from the two beam energies .	120
5.2.2	Combining uncertainties from the ten sources	121
5.2.3	Combining data from the two beam energies	121
6	Results	133
6.1	Extracted g_1 and A_1F_1	133
6.2	Moments of Deuteron Spin Structure functions	142
6.2.1	First moment of g_1 (Γ_1)	144
6.2.2	The extended GDH integral \bar{I}_{TT}	146
6.2.3	The Generalized Forward Spin Polarizability γ_0	148
7	Conclusions	151

¹ Chapter 1

² Introduction

³

⁴ A truly vast amount of data on the inelastic structure of the nucleon has
⁵ been accumulated since the late 1960s from both fixed target and colliding
⁶ beam experiments with polarized as well as un-polarized incident photons,
⁷ (anti)electrons, muons and (anti)neutrinos as well as (anti)protons on a vari-
⁸ ety of targets (both polarized and unpolarized) from hydrogen through iron
⁹ [1]. The initial measurements at SLAC confirmed the picture of the nucleon
¹⁰ as made up of partons (now identified with quarks and gluons). Since then
¹¹ more precise measurements have been conducted at several accelerators, im-
¹² proving our knowledge and understanding about the nucleon structure (both
¹³ spin-dependent and spin-averaged), and, at the same time, continuing to give
¹⁴ us new and sometimes very surprising results such as the original “European
¹⁵ Muon Collaboration (EMC)-Effect” [2], the violation of the Gottfried sum
¹⁶ rule [3, 4], and the so-called ”Spin-Crisis” [5, 6] (see below). **Will soon work**
¹⁷ **on the order of references/citations.**

¹⁸ With such a vast amount of experimental data available, a lot is now
¹⁹ known about the spin-averaged quark structure of the nucleon, but a lot less
²⁰ is known about the spin-structure of the nucleon in terms of its constituents
²¹ quarks and gluons [1]. In a simple non-relativistic model one would expect
²² the quarks to carry the entire spin of the nucleon, but one of the early more
²³ realistic theories that explained the partonic substructure of the nucleon,
²⁴ the Naive Parton Model (NPM), predicted that 60% of the nucleon spin is
²⁵ carried by the quarks [7].

²⁶ The polarized beam and target technologies have greatly advanced dur-
²⁷ ing the last three decades, and many subsequent experiments on nucleons

and some nuclei have contributed to the extraction of their spin structure functions g_1 and g_2 , which carry information on how the spin is distributed inside the target. One of the first experiments carried out at SLAC, in a limited kinematic region, seemed to confirm the predictions of the NPM. However, a subsequent, more precise measurement over a larger kinematic region performed by the EMC experiment at CERN reported that, contrary to the NPM predictions, only $12 \pm 17\%$ of the spin is carried by the quarks [5, 6]. This discovery of the so-called “spin crisis” sparked a large interest in measuring the spin content of the nucleon, giving birth to several experiments (completed, underway and proposed) around the globe. The theoretical developments of Quantum Chromodynamics (QCD) - the quantum field theory that describes the nuclear interaction between the quarks and gluons - have clarified our picture of the nucleon spin structure in great details. With the discovery of a unique QCD property known as “asymptotic freedom”, quarks are known to be essentially free at high energies (typically several GeV) allowing perturbative QCD (PQCD) calculations of testable predictions for processes involving high energy or high momentum transfers [8]. Verifying Bjorken sum rule, Reference to be added soon which relates results from inclusive, polarized deep inelastic scattering (DIS) to the axial coupling constant g_A of neutron beta decay, is a precise test of QCD in its spin sector. The DIS results have verified the Bjorken sum rule at the level of 10% accuracy and has shown that only about $30 \pm 10\%$ of the nucleon spin is carried by the quarks; the rest of the spin must reside either in gluons or orbital angular momentum of its constituents. Experiments to measure the gluon contribution are underway at Brookhaven National Laboratory (BNL) and CERN.

Probing nucleon structure on the other end of the energy scale (i.e. probing with low momentum transfers) provides information about long distance structure, which is also associated with static properties of the nucleon. In this low energy regime, however, QCD calculations with the established perturbative methods become difficult or even impossible because the strong coupling (α_s) becomes large. Thus perturbative expansions do not converge. In this energy regime, the partons become very strongly coupled to the point of being confined into hadrons which now emerge as the effective degrees of freedom for the interaction. Therefore, other methods must be relied on to make predictions in these non-perturbative energy scales. For example, effective theories such as chiral perturbation theory (χ PT) are used. There is also an intermediate region where neither of these approaches (PQCD or χ PT)

is expected to work. In this region, it is expected that lattice QCD methods will provide testable predictions in the near future. There are also some phenomenological models aimed at describing the entire kinematic range. The description of the low energy regime in terms of these theories and models is challenging and theories used here still face difficulties (see below). There are several predictions (for both nucleons as well as some light nuclei such as the deuteron and Helium-3) from these low energy theories and models on various observables which can be tested experimentally. Therefore, having high precision data at the lowest possible momentum transfer is necessary to test these predictions. In addition, new results will also help constrain future calculations and provide input for detailed corrections to higher energy data.

With that perspective and motivation, the “EG4” experiment (E06-017) for a precision double polarization measurement at low momentum transfer using both proton and deuteron targets and the Hall B CLAS detector was performed at Jefferson Lab. In addition to the usefulness of the measured deuteron data for testing theoretical predictions calculated for the deuteron itself, the data are also necessary for extracting neutron data in combination with similar data from the proton target. An experiment with the similar goal of probing the neutron at low momentum transfers but using ^3He was performed in Hall A [9]. However, to be able to control nuclear medium effects, neutron information must be extracted from both ^3He and ^2D . The data on the deuteron (and eventually on the neutron) will not only be useful to test the theoretical predictions at low but non-zero momentum transfers but they can also be extrapolated to the real photon limit, thus testing some long standing predictions such as the Gerasimov-Drell-Hearn (GDH) sum rule Reference to be added soon derived from general principles. The analysis of the deuteron data is the subject of this note.

In the future, we will extract information from the deuteron and proton data from the EG4 experiment to provide a self-consistent determination of the Bjorken sum, helping us to understand the transition from the partonic to hadronic descriptions of the strong interaction. The data will also be useful in studying the validity of quark-hadron duality in the spin sector, thus helping further to understand the transition from the partonic to hadronic pictures.

₉₉ **1.1 Inclusive Electron Scattering**

₁₀₀ High energy particle scattering processes provide very powerful microscopes
₁₀₁ to examine objects such as nuclei and nucleons. Scattering of leptons (most
₁₀₂ commonly electrons) is one of the most extensively used processes. For ex-
₁₀₃ ample, the scattering of high energy leptons off nucleons has played a key role
₁₀₄ in determining the partonic structure of the nucleons. Following are some of
₁₀₅ the advantages of lepton (and in particular electron) scattering:

- ₁₀₆ • Leptons interact through the electroweak interaction which is very well
₁₀₇ understood.
- ₁₀₈ • The interaction is relatively weak, thus allowing the use of perturbative
₁₀₉ QED.
- ₁₁₀ • In electron scattering, one can, moreover, control and vary the po-
₁₁₁ larization of the virtual photon (exchanged during the interaction) by
₁₁₂ changing the electron kinematics. This allows the separation of the
₁₁₃ charge and current interaction. Data from the scattering of polarized
₁₁₄ electrons by polarized targets allows one to examine the target's strong-
₁₁₅ interaction spin structure.
- ₁₁₆ • A great advantage of electrons is that they can be copiously produced
₁₁₇ in the laboratory relatively easily and at low costs, and since they are
₁₁₈ charged, they can readily be accelerated and detected. (It is not as
₁₁₉ easy and cheap to produce and handle the other lepton types.

₁₂₀ In this section, we discuss the process of inclusive electron scattering (in
₁₂₁ which only the scattered electron is detected ignoring the rest of the com-
₁₂₂ ponents of the final state after the interaction). In doing so, the relevant
₁₂₃ kinematic variables and related physical quantities to be measured or calcu-
₁₂₄ lated from the process will be introduced and some of their relations with
₁₂₅ one another will be deduced and discussed.

₁₂₆ **1.1.1 Kinematic Variables**

₁₂₇ A lepton scattering process, in which an incoming lepton represented by $l(p)$
₁₂₈ of four momentum $p = p^\mu = (E, \vec{k})$ scatters off a target $N(P)$ which is usually

¹²⁹ a nucleon or a nucleus at rest and with four momentum $P = P^\mu = (M, \vec{0})$,
¹³⁰ can simply be represented by

$$l(p) + N(P) \rightarrow l(p') + X(P') \quad (1.1)$$

¹³¹ where $l(p')$ and $X(P')$ represent the scattered lepton and the rest of the
¹³² final state (which can have any number of particles) with four momenta
¹³³ $p'^\mu = (E', \vec{k}')$ and $P'^\mu = (E_X, \vec{k}_X)$ respectively. The scattering angle which is
¹³⁴ the angle between the incident and outgoing path/direction of the electron
¹³⁵ is denoted by θ . The final (hadronic) state denoted by x is not measured,
¹³⁶ with only the scattered electron detected and measured by the detector(s).
¹³⁷ In the first order (Born) approximation of the process, a virtual photon is
¹³⁸ exchanged (as depicted in Fig (1.1)) whose four momentum is equal to the
¹³⁹ difference between that of the incident and the scattered electron and is given
¹⁴⁰ by $(p - p')^\mu = (\nu, \vec{q})$, where $\nu = (P \cdot q)/M$ and \vec{q} represent the energy and
¹⁴¹ 3-momentum transferred by the incident electron to the target $N(P)$.

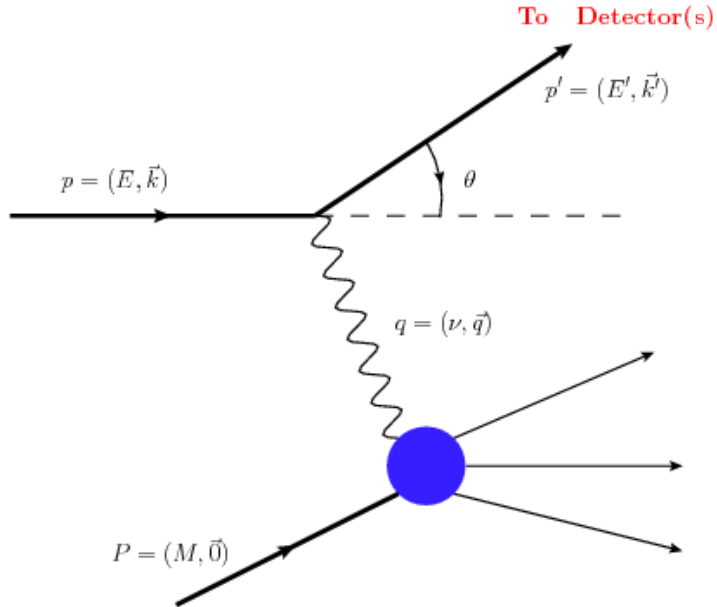


Figure 1.1: Lowest order (Born approximation) Feynmann diagram representing the process of inclusive lepton scattering

¹⁴² The kinematics of the scattering process, for a given beam energy E , can
¹⁴³ be completely described in terms of two of the following Lorentz invariant

144 variables.

$$\nu = E - E' \quad (1.2)$$

$$Q^2 = -q^2 \simeq 4EE' \sin^2 \frac{\theta}{2} \quad (1.3)$$

$$W = \sqrt{(P+q)^2} = \sqrt{M^2 + 2M\nu - Q^2} \quad (1.4)$$

$$x = \frac{Q^2}{2P \cdot q} = \frac{Q^2}{2M\nu} \quad (1.5)$$

$$y = \frac{q \cdot P}{p \cdot P} = \frac{\nu}{E} \quad (1.6)$$

145 where $Q^2 = -q^2$ is the negative of the squared four-momentum transferred
146 (with electron mass neglected in the expression for Q^2), which defines the
147 resolution of the electron probe; W is the invariant mass of the unmeasured
148 final state (x); x is known as the Bjorken scaling variable, which is also
149 interpreted as the momentum fraction carried by the struck quark (parton)
150 in the infinite momentum frame; M is the nucleon mass ≈ 0.939 GeV, and
151 lastly, y is the fraction of the energy that is lost by the lepton during the
152 process.

153 1.1.2 Differential Cross Section and Structure Functions

154

155 The differential cross section for the process of inclusive (polarized) elec-
156 tron scattering on (polarized) targets can be expressed, in the Born ap-
157 proximation, in terms of four dimensionless structure functions $F_1(x, Q^2)$,
158 $F_2(x, Q^2)$, $g_1(x, Q^2)$, and $g_2(x, Q^2)$, effectively parameterizing the internal
159 hadronic structure information into four response functions. For example,
160 in the case of the anti-parallel or parallel beam and target polarizations,
161 the spin-dependent (polarized) inclusive cross sections can be expressed as
162 follows:

$$\frac{d^2\sigma}{d\Omega dE'} = \left(\frac{d\sigma}{d\Omega} \right)_{Point} \left[\frac{2}{M} F_1(x, Q^2) \tan^2 \frac{\theta}{2} + \frac{1}{\nu} F_2(x, Q^2) \right. \\ \left. \pm 2 \tan^2 \frac{\theta}{2} \left[(E + E' \cos \theta) \frac{M^2}{\nu} g_1(Q^2, \nu) - \gamma^2 M^2 g_2(Q^2, \nu) \right] \right]^{(1.7)}$$

163 where “+” refers to anti-parallel beam helicity and target polarization,
 164 while “-” refers to the parallel case. And the Point cross section (for the
 165 lepton scattering from a Dirac particle - a spin-1/2 point particle of charge
 166 +e) given by

$$\left(\frac{d\sigma}{d\Omega} \right)_{Point} = \frac{\alpha^2 \cos^2 \frac{\theta}{2}}{4E^2 \sin^4 \frac{\theta}{2}} \frac{E'}{E} \quad (1.8)$$

167 with $\frac{E'}{E}$ being the recoil factor.

168 These kind of relationships allow the measurement of structure functions
 169 by measuring cross-sections corresponding to different combinations of beam
 170 and target polarizations. For example, one can extract the first two structure
 171 functions F_1 and F_2 from the unpolarized scattering experiments, whereas,
 172 the spin structure functions g_1 and g_2 can be measured in experiments with
 173 polarized electron beam and polarized targets and by measuring the cross
 174 section difference between the anti-parallel and parallel beam-target polar-
 175 izations.

176 1.2 Moments of g_1 and Sum Rules

177 Moments of structure functions are their integrals (over the complete x range)
 178 weighted by various powers of the variable x. The n^{th} moment of g_1 , for
 179 example, is given by

$$\Gamma_n(Q^2) = \int_0^1 g_1(x, Q^2) x^{(n-1)} dx \quad (1.9)$$

180 The moments allow the studies of the (Q^2 dependence of) fundamental
 181 properties of nucleon structure. For example, the first moment of xF_1 of a
 182 nucleon gives the total momentum or mass fraction carried by quarks and
 183 the first moment of g_1 gives the fraction of the nucleon spin contributed by
 184 the quark helicities. These integrals get their particular significance from
 185 the fact that they can be predicted from rigorous theoretical methods, such
 186 as in the sum rules derived from general assumptions or from the method of
 187 Operator Product Expansion, lattice QCD calculations and χ PT calculations

¹⁸⁸ ¹ (see Sec. ??). Their importance can be highlighted from the fact that it
¹⁸⁹ was the experimental tests of the sum rules involving the first moments of
¹⁹⁰ nucleon that led to the discovery of the original “spin crisis” and provided a
¹⁹¹ significant test of QCD in the spin sector [10].

¹⁹² In this section, three integrals are considered which have been calculated
¹⁹³ from the EG4 data on the deuteron - the first moment of g_1 (Γ_1), the gen-
¹⁹⁴ eralized GDH integral (\bar{I}_{TT}), and the generalized forward spin polarizability
¹⁹⁵ (γ_0).

¹⁹⁶ 1.2.1 First moment Γ_1 of g_1

¹⁹⁷ The first moment of g_1 is the integral of g_1 over the complete range of the
¹⁹⁸ Bjorken scaling variable x .

$$\Gamma_1(Q^2) = \int_0^1 g_1(x, Q^2) dx \quad (1.10)$$

¹⁹⁹ This moment gives, in the quark-parton model, the fraction of the nu-
²⁰⁰ cleon spin contributed by the quark helicities and enters directly into two
²⁰¹ historically important sum rules - Ellis-Jaffe sum rule and Bjorken sum rule.
²⁰² Measurements of the moment on the proton by the European Muon Collabo-
²⁰³ ration (EMC) in 1988 showed that the Ellis-Jaffe sum rule is violated, which
²⁰⁴ meant that the long held belief that all the proton spin is carried by quarks
²⁰⁵ is not true, thus, sparking the well known “spin crisis”. On the other hand,
²⁰⁶ measurements from SLAC, CERN, Fermilab, DESY, and more recently, from
²⁰⁷ JLab, have confirmed the Bjorken sum rule (which relates the difference of
²⁰⁸ the first moments of the proton and the neutron to the fundamental axial
²⁰⁹ coupling constant (g_A) of neutron beta decay) at the level of 10% accuracy,
²¹⁰ thus helping establish the QCD as the correct theory of the strong interac-
²¹¹ tions. The moment also enters into the virtual photon extension of another
²¹² famous sum rule - the GDH sum rule (see below).

²¹³ In addition, the moment is studied on its own right because it provides
²¹⁴ a powerful tool to test the validity of various theories and models in which
²¹⁵ it is calculable. In the past, it has been measured on proton, deuteron and

¹In contrast, the same is not true about the structure functions because presently their complete description based on QCD first principles has not been possible yet (especially in the low to intermediate momentum transfer regions due to the strong coupling property of QCD).

216 neutron (${}^3\text{He}$) at SLAC, CERN and DESY in the DIS region in order to
217 understand the quark spin contribution as well as to test the validity of the
218 Bjorken sum rule and hence QCD as a result [10]. Recently, it has also
219 been measured at JLab from DIS down to a fairly low Q^2 region. In the
220 intermediate and low momentum transfers, some phenomenological model
221 predictions are available, whereas in the very low Q^2 region, several chiral
222 perturbation theory (χPT) calculations are available.

223 **1.2.2 Generalized GDH Integral**

224 **GDH Sum Rule**

225 The Gerasimov-Drell-Hearn (GDH) sum rule [11, 12] relates the energy weighted
226 sum of a particle's photo-absorption cross sections to its anomalous magnetic
227 moment κ . For a target of arbitrary spin S , the sum rule is:

$$\int_{\nu_{th}}^{\infty} \frac{\sigma_P(\nu) - \sigma_A(\nu)}{\nu} = -4\pi^2 \alpha S \left(\frac{\kappa}{M}\right)^2 \quad (1.11)$$

228 where σ_P and σ_A are the photoabsorption cross sections with photon helicity
229 parallel and anti-parallel to the target spin respectively. M and κ represent
230 the target mass and anomalous magnetic moment respectively and S rep-
231 resents the target spin. The integration extends from the onset ν_{th} of the
232 inelastic region ² through the entire kinematic range and is weighted by the
233 inverse of the photon energy ν .

234 The sum rule for the proton has been measured (at various places such
235 as Mainz, Bonn, BNL and others) and verified to within 10% [13–16] and
236 some deuteron results exist from Mainz and Bonn, but there is very little or
237 no data available on neutron and other targets;

238 **Implications of the sum rule** The sum rule relates the static property
239 κ of a particle's ground state with the sum of the dynamic properties of
240 all the excited states. One deeper significance of this sum rule is that if a
241 particle has a non-zero anomalous magnetic moment, then it must have some
242 internal structure, and, therefore, a finite size, in order to have the excited
243 states (a point-like particle cannot have excited states). Because of the same
244 reason, the discovery of nucleon anomalous magnetic moments provided one
245 of the first strong indications that the nucleons had some intrinsic internal
246 structure.

247 In addition to the benefit of that implication, the sum rule and its exten-
248 sion to $Q^2 > 0$ provides an important testing ground for various theoretical
249 predictions based on QCD and its effective theories/models.

247²The pion photo-production threshold given by $\nu_{th} = m_\pi(1 + m_\pi/2M) \approx 150\text{MeV}$ marks the onset of the inelastic region for the nucleons, but for nuclei, the summation starts from the first nuclear excitation level

250 **Generalization of the GDH Sum (Rule)**

251 In order to investigate the “spin crisis” of the 1980’s, Anselmino *et al.* [17]
 252 proposed that the real photon ($Q^2=0$) GDH integral could be extended to
 253 electroproduction cross sections (finite Q^2) and that the experimental deter-
 254 mination of the extended integral would shed light on the transition from
 255 the perturbative to non-perturbative QCD. The idea was to use the virtual
 256 photoabsorption cross sections in place of the real photoabsorption cross sec-
 257 tions and proceed in exactly the same way as when deriving the real photon
 258 GDH sum rule. This extension depends somewhat on the choice of the vir-
 259 tual photon flux and on how the spin structure function g_2 is considered [18].
 260 In one extension the virtual photon flux given by $K = \nu$ is chosen and the
 261 real photoabsorption cross section difference in Eq. 1.11 are replaced by
 262 the corresponding virtual photoabsorption cross section difference $2\sigma_{TT}$. As
 263 a result, we get the following extended GDH integral (considering only the
 264 inelastic contribution starting from the pion production threshold) [10]

$$\bar{I}_{TT} = \frac{2M^2}{Q^2} \int_0^{x_0(Q^2)} dx [g_1(x, Q^2) - \frac{4M^2 x^2}{Q^2} g_2(x, Q^2)] \quad (1.12)$$

265 where $x_0(Q^2) = Q^2/(Q^2 + m_\pi(2M + m_\pi))$ is the pion production threshold
 266 that defines the onset of the inelastic region.

267 The integral can also be expressed in terms of the first moment of the
 268 product $A_1 F_1$ as follows:

$$\bar{I}_{TT} = \frac{2M^2}{Q^2} \int_0^{x_0(Q^2)} dx A_1(x, Q^2) F_1(x, Q^2) \quad (1.13)$$

269 where A_1 is the virtual photon asymmetry as given by:

$$A_1(x, Q^2) = \frac{\sigma_{\frac{1}{2}}^T - \sigma_{\frac{3}{2}}^T}{\sigma_{\frac{1}{2}}^T + \sigma_{\frac{3}{2}}^T} = \frac{g_1(x, Q^2) - \gamma^2 g_2(x, Q^2)}{F_1(x, Q^2)} \quad (1.14)$$

$$(1.15)$$

270 **1.2.3 Generalized Forward Spin Polarizability γ_0**

271 Polarizabilities are fundamental observables (quantities) that characterize the
 272 structure of composite objects such as nucleons or deuteron. They reflect the
 273 response to external perturbations such as external electromagnetic fields.
 274 Like the GDH sum, they are also integrals over the excitation spectrum of
 275 the target and their derivations rely on the same basic assumptions. At
 276 the real photon point, for example, the electric and magnetic polarizabilities
 277 α and β represent the target's response to external electric and magnetic
 278 fields respectively. The generalized polarizabilities represent the extensions
 279 of these quantities to the case of virtual photon Compton scattering. Because
 280 the integrals defining the polarizabilities involve weighting by some powers
 281 of $1/\nu$ or x , they converge faster than the first moments and thus are more
 282 easily determined from low energy measurements. In other words, they have
 283 reduced dependence on the extrapolations to the unmeasured regions at large
 284 ν , and higher sensitivity to the low energy behavior of the cross sections
 285 (particularly the threshold behavior), thus providing better testing grounds
 286 for theoretical predictions such as from χ PT and phenomenological models
 287 [18].

288 The GDH sum rule comes from the first term of the low energy expansion
 289 of the forward Compton amplitude [19]. Likewise, we get another sum rule
 290 from the second, i.e., the next-to-leading term (which is in the third power
 291 of ν). The second coefficient of the expansion is known as the forward spin
 292 polarizability γ_0 and by comparing the coefficients of the ν^2 terms on both
 293 sides (coming from the dispersion relations on the left side and from the low
 294 energy expansion on the right side) gives us the following expression for the
 295 polarizability [20]:

$$\gamma_0 = -\frac{1}{4\pi^2} \int_{thr}^{\infty} \frac{\sigma_{\frac{1}{2}} - \sigma_{\frac{3}{2}}}{\nu^3} d\nu \quad (1.16)$$

296 Now, by considering the case of forward scattering of a virtual photon and
 297 using the same general approach as for getting the generalized GDH sum rule,
 298 the $\mathcal{O}(\nu^3)$ (NLO) term in the low energy expansion of VVCS (doubly virtual
 299 Compton scattering) amplitude $g_{TT}(x, Q^2)$ gives the following generalization
 300 of the forward spin polarizability [21] [10]:

$$\begin{aligned}\gamma_0(Q^2) \equiv \gamma_{TT}(Q^2) &= \frac{16\alpha M^2}{Q^6} \int_0^{x_0} \left[g_1(x, Q^2) - \frac{4M^2 x^2}{Q^2} g_2(x, Q^2) \right] x^2 dx \\ &= \frac{16\alpha M^2}{Q^6} \int_0^{x_0} A_1(x, Q^2) F_1(x, Q^2) x^2 dx\end{aligned}\quad (1.18)$$

301 where $\alpha = \frac{e^2}{4\pi}$ is the fine structure constant. At large Q^2 , the g_2 dependent
 302 term in the integrand becomes negligible and γ_0 reduces to the third moment
 303 of g_1 [21].

304 In exactly the same manner, from the $\mathcal{O}(\nu^2)$ term of the low energy
 305 expansion of the VVCS amplitude $g_{LT}(x, Q^2)$ one gets another polarizability
 306 - the generalized longitudinal-transverse polarizability as follows:

$$\delta_0(Q^2) \equiv \delta_{LT}(Q^2) = \frac{16\alpha M^2}{Q^6} \int_0^{x_0} [g_1(x, Q^2) + g_2(x, Q^2)] x^2 dx \quad (1.19)$$

307 This latter polarizability is not considered here because we did not measure
 308 the transverse target configuration.

309 Because the generalized polarizabilities can be expressed with the mo-
 310 ments of the structure functions, it is possible to measure them using mea-
 311 surements of the structure functions. As stated earlier, because of the weight-
 312 ing by some powers of ν or x , these integrals converges more rapidly in energy
 313 than the GDH integral and therefore can more easily be determined by low
 314 beam energy measurements. These integrals are valuable because they shed
 315 light on the long distance (soft), non-perturbative aspects of the target struc-
 316 ture. The integrals are possible to be calculated using effective or approxi-
 317 mate theories such as χ PT and lattice methods. Thus the measurements of
 318 these quantities provide benchmark tests of such theories.

319 The first measurement of γ_0 for a proton target at the real photon point
 320 was done by the GDH experiment at Mainz [20]. Recently the JLab EG1b
 321 experiment has provided some finite Q^2 results for both deuteron (see Fig.
 322 ??) as well as nucleon targets [22].

³²³ **Chapter 2**

³²⁴ **EG4 run**

³²⁵ The deuteron target part of the EG4 experiment ran for about a month
³²⁶ in 2006, mostly with longitudinally polarized frozen $^{15}\text{ND}_3$ as the target. In
³²⁷ between these deuteron runs, some small amount of data was also collected on
³²⁸ carbon-12 and empty cell targets, which are important in various auxiliary
³²⁹ studies during the data analysis (such as their use in estimating nuclear
³³⁰ background while developing momentum corrections, estimating the length
³³¹ of the target material or estimating unpolarized background). A total of 113
³³² data runs (from run ID 51896 to 52040) were collected for the lower beam
³³³ energy (1.3 GeV) and 221 runs (from 51593 to 51867) for the 2.0 GeV case
³³⁴ (with each run consisting of about 3.0×10^7 event triggers) [23]. Each run
³³⁵ took about 2 hours and collected about 2 GB of data in raw format and
³³⁶ saved as about 20-30 BOS files (see next section). With the combination of
³³⁷ low beam energies and low scattering angles, low momentum transfers can
³³⁸ be measured down to about 0.02 GeV² within the kinematic coverage of the
³³⁹ resonance region ($1.08 < W < 2.0$ GeV.)

³⁴⁰ In addition to the use of low beam energies and low θ measurements, in
³⁴¹ order to maximize the statistics in the low momentum transfers, following
³⁴² measures were taken that were unique to the experiment:

- ³⁴³ • Used electron outbending torus field configuration to enhance the low
³⁴⁴ angle acceptance (so that more of very forward going electrons would
³⁴⁵ be bent towards and detected by the CLAS detector).
- ³⁴⁶ • Used (in the 6th sector¹) a newly built Cerenkov Counter (CC) (see
³⁴⁷ Figs. 2.1 and 2.2) that was designed to optimize electron detection in

¹For reasons of limited resources, only one new CC was built and the 6th sector alone

348 the outbending torus configuration such that the detection efficiency
349 would be better and more uniform than with the existing counters²
350 which were optimized for electron inbending configuration.

- 351 • To further enhance the low angle coverage, the polarized target was
352 placed in a more retracted position along the beam line i.e. at about
353 -101.0 cm upstream of the CLAS center.

354 Other than that the CLAS detector was used in the standard configuration
355 like in any other polarized target experiments using CLAS.

356 **New CC in the 6th Sector**

357 The Cherenkov Counters (CC) serve the dual function of triggering on elec-
358 trons and separating electrons from pions (or identifying charged particles).
359 These detectors use the light emitted by Cherenkov radiation (emission of
360 light when the charged particle travels faster than light in that medium)
361 to measure the particle velocity (and, therefore, $\beta = v/c$). The knowledge
362 of β combined with the particle momentum (from the tracking detectors)
363 determines the particle's mass, thus giving us information on the particle
364 identification. The index of refraction (n) is carefully optimized for the par-
365 ticle masses and momentum range of the experiments in question. Thresh-
366 old counters record all light produced, thus providing a signal whenever β is
367 above the threshold $\beta_t = 1/n$. In the standard configuration, CLAS uses one
368 Cherenkov threshold detector in each of the six sectors in the forward region
369 from 8° to 45°.

370 The standard CLAS Cherenkov detectors (as shown by Figs. ?? and ??)
371 were designed such that their optics, geometry, module position and mir-
372 ror orientation were optimized for low rate high Q^2 experiments that mostly
373 use(d) electron in-bending torus fields. The design was a compromise between
374 the desired kinematic coverage and the complexities of the CLAS detector
375 system including the effect of the torus field. As a consequence, light col-
376 lection is constrained causing the number of photoelectrons to be strongly

was used to detect the scattered electrons

²The standard CLAS Cherenkov detectors were designed such that their optics, geometry, module position and mirror orientation were optimized for low rate high Q^2 experiments that mostly use(d) electron in-bending torus fields. The design was a compromise between the desired kinematic coverage and the complexities of the CLAS detector system including the effect of the torus field.

377 dependent on scattering angles, and making the detection efficiency non-
378 uniform, and strongly reduced in some regions (for example, up to 30% drop
379 in the middle of the sector and at forward angles) [20]. While it would still be
380 possible to detect electrons, the use of the existing CC would mean that the
381 absolute cross-section measurement would require large and complex correc-
382 tions which are difficult to evaluate. That would significantly contribute to
383 the systematic uncertainties, thus not meeting the proposed high accuracy
384 requirement of the measurements.

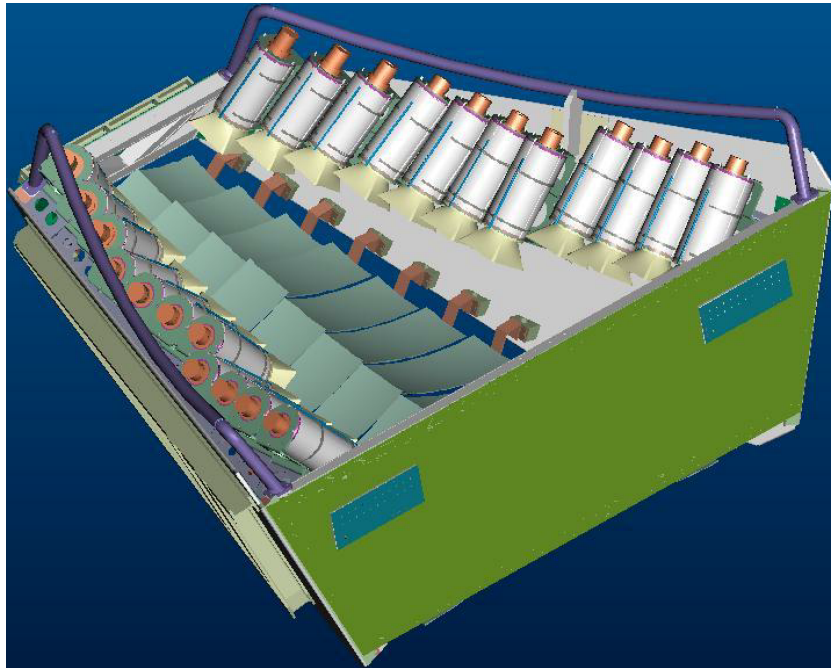


Figure 2.1: The new Cherenkov counter (courtesy of INFN, Genova)

385 In order to avoid having all those CC-related issues in the new measure-
386 ments, a new gas threshold cherenkov counter (designed and built by INFN
387 - Genova, Italy) was installed in the sixth sector. This new CC detector (see
388 Fig. 2.1 for its CAD rendition) is specifically optimized for the out-bending
389 field configuration, which is necessary to reach the desired low momentum
390 transfer (measurements down to 6 degrees). The detector uses the same ra-
391 diator gas (C_4F_{10} - perfluorobutane) and the same gas flow control system
392 as the old one, but it uses a different design. In the new CC, the number
393 of CC-modules is now 11 instead of the 18 in the standard ones. In order

394 to maximize the light collection, a single reflection design (see Fig. 2.2(b))
 395 using spherical mirrors is used (the standard CC used double relections from
 396 elliptical and hyperbolic mirrors). The geometry, the size, the mirror size,
 397 position, and orientation, the dimensions as well as the assembly of the mod-
 398 ules were optimized for the experiment and the performance study was done
 399 using a complete GEANT simulation [20].

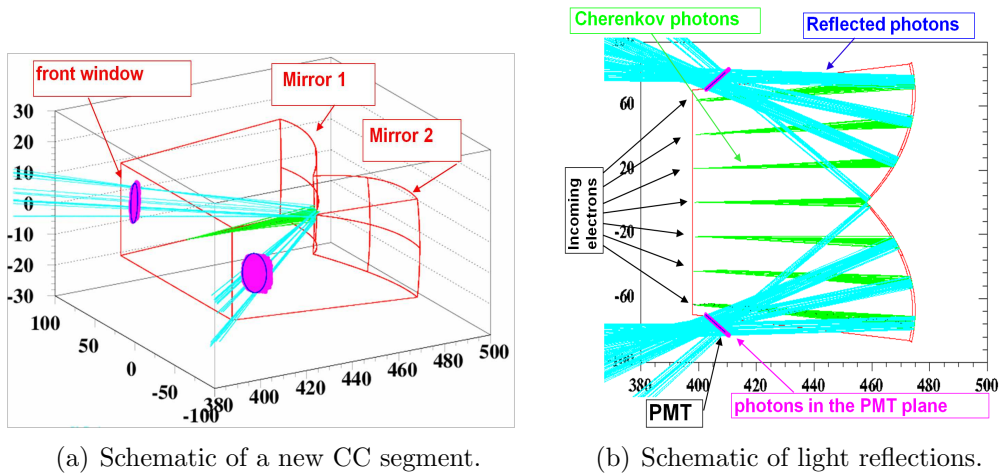


Figure 2.2: Schematic of a new CC segment showing the arrangements of the mirrors, PMTs and the light reflections (courtesy of INFN, Genova).

400 **Chapter 3**

401 **Data Analysis Procedure**

402 The goal of this data analysis is to extract the spin structure function g_1 for
403 the deuteron and evaluate its moments. Since the product $A_1 F_1$, which is
404 proportional to σ_{TT} , directly enters sum rules for the real photon point, which
405 leads to the generalized GDH integral (\bar{I}_{TT}) and the generalized forward spin
406 polarizability (γ_0) being expressed in terms of the first and third moments of
407 the product $A_1 F_1$, we decided also to extract the product $A_1 F_1$ using exactly
408 the same procedure as for g_1 .

409 The extraction of both g_1 and $A_1 F_1$ depend directly on the measurement
410 of the following polarized cross-section difference:

$$\Delta\sigma_{||} = \frac{d^2\sigma^{\downarrow\uparrow}}{d\Omega dE'} - \frac{d^2\sigma^{\uparrow\uparrow}}{d\Omega dE'} = \frac{1}{N_t} \cdot \left[\frac{N^+}{N_{e^-}^+} - \frac{N^-}{N_{e^-}^-} \right] \cdot \frac{1}{P_b P_t} \cdot \frac{1}{\Delta\Omega} \cdot \frac{1}{\eta_{detector}} \quad (3.1)$$

411 where,

- 412 • N_t = Number of deuteron nuclei in the target
- 413 • $N^{+/-}$: Number of scattered electrons (off deuteron only) for each helicity state (+/-).
- 414 • $N_{e^-}^{+/-}$: Number of incident electrons for +/- helicity states
- 415 • $P_b P_t$ = Product of the beam and target polarizations
- 416 • $\Delta\Omega = \sin\theta \cdot \Delta\theta \cdot \Delta\phi$: The solid angle for the given kinematic bin. This term includes the “detector acceptance”.

419 • $\eta_{detector}$ accounts for the detector efficiencies
420 The data analysis to extract the physics quantities involves accurately
421 measuring each of these quantities, either separately or in some combined
422 form. To do so, the data must be properly reconstructed, calibrated and
423 corrected to build all the scattering events during the experiment. Since
424 the reconstructed events include a wide range of physical processes in ad-
425 dition to the electron-deuteron scattering process that we are interested in,
426 proper event selection cuts must be applied. In this chapter, all these steps
427 from the data reconstruction and calibration through the extraction of g_1 are
428 described.

429

430 **3.1 Raw Data Processing - Calibration and**
431 **Reconstruction**

432 The raw data recorded by the CLAS DAQ system, which consists of ADC
433 and TDC values registered by various detector components as well as the
434 beam related information such as beam helicity and Faraday Cup readings,
435 are organized into banks (with each bank carrying data belonging to a par-
436 ticular detector component or some part of it) and saved in special format
437 (BOS) files. These raw data are next processed with a standard CLAS soft-
438 ware package called RECSIS, which analyzes and combines the matching bits
439 and pieces of the raw information to reconstruct particles and events that
440 produced them. Such reconstruction produces output data that consist of
441 event and particle IDs, particle positions and energies and momenta (in the
442 lab frame CLAS coordinate system), and also some static particle properties
443 such as charge and mass. The reconstruction program uses geometric pa-
444 rameters and calibration constants (from the CLAS Calibration Database)
445 for the detector in order to properly process and transform the raw data into
446 the reconstructed tracks.

447 The first part of the data processing is the detector calibration. In this
448 phase, a small sample (about 10%) of raw data (uniformly selected over the
449 entire run period to ensure time stability verification) is chosen and the en-
450 ergy and time calibration constants are adjusted to give the correct behavior
451 while constantly monitoring related variables. This is done separately for
452 each run period to consider the different running conditions, the possibility

453 of unwanted changes in hardware that may have occurred, as well as drift
454 of detector response over time. This process of adjusting the calibration
455 constants and reconstructing the data is repeated until a desired level of ac-
456 curacy is reached. Once that level is reached, the calibration constants are
457 “frozen” and the final reconstruction is done. The resulting output is saved
458 in especial formats¹.

459 These saved data provided the starting point for our higher level data
460 analysis as described in this dissertation. The details of the calibration and
461 reconstruction process can be found in [24].

462 The iterative work of data reconstruction and detector calibration, which
463 was a very computing intensive and time consuming, was done by R. De
464 Vita - one of the EG4 collaborators from INFN, Genova, with good expertise
465 on CLAS data reconstruction - soon after the data collection was completed
466 (from 2006-2007). The data from this “Pass1” reconstruction was first an-
467 alyzed as part of the Ph. D. dissertations by three graduate students, but
468 during these analyses, a few anomalies² in reconstruction were observed which
469 were later tracked down to a mixing up of codes from two EG4 sub-packages
470 for the reconstruction software. After the mix-up was sorted out, a new pass
471 (Pass2) of reconstruction was performed by L. El Fassi (still using the same
472 calibration constants as used by the Pass1 reconstruction). The data from
473 this latest pass of reconstruction was used for the analysis reported in this
474 note

¹Two especial data formats - BOS and ntuple (h10) - were used

²The anomalies observed in the pass1 analysis were the discretized reconstruction of vertex and wrong reconstruction of track positions in DC1.

475 **3.2 Helicity States**

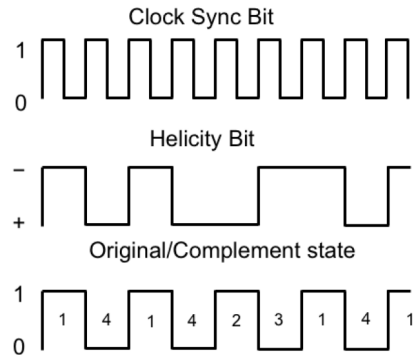


Figure 3.1: Different data signals sent from the injector that monitor the helicity states of beam electrons. (Fig. courtesy of N. Guler [22]).

476 As we saw from Eq. 3.1, the physics extraction depends on measurements of
477 the number of events in the two (+/-) electron helicity states. The CEBAF
478 accelerator provides the polarized electrons in closely and equally spaced
479 bunches. These bunches are further grouped into “buckets” according to
480 their helicity states, which are alternated pseudo-randomly at the injector
481 with a frequency of 30 Hz. The information on the helicity state of each of
482 the buckets and the total integrated charge contained in it is injected into the
483 DAQ data stream immediately after the helicity flip. Using a combination of
484 different types of sequence control signals sent from the injector (see Fig. 3.1),
485 it is possible to determine which helicity state a particular event belonged
486 to, which then can be used to label the helicity state of the event in the data
487 stream, together with the total beam charge of the state.

488 **3.3 Electron Identification**

489 In CLAS electron-scattering experiments, the scattered electron defines the
490 timing of each event. In addition, in inclusive measurements, the scattered

491 electron is the only particle to be detected and measured. So, it is particu-
492 larly important to make sure that electrons are well measured and properly
493 identified and are not contaminated with misidentified particles such as neg-
494 ative pions (π^-) or lost by being misidentified.

495 The process of identifying the primary scattered electrons starts by first
496 rejecting all those particle candidates which are not the first entries (i.e., the
497 trigger particles) in the event bank. The remaining sample of the candidates
498 is refined further by rejecting those with positive charges. Then, the sample
499 is further refined by applying a set of cuts that are listed and described below.
500 An electron candidate is considered good if it passes all of these cuts.

501 1. Good Electron Cuts

- 502 (a) **Cut on particle charge:** $q=-1$
- 503 (b) **Detector status cuts:**
 - 504 i. **DC status:** $dc>0$; $dc_part>0$
 - 505 ii. **SC status:** $sc>0$; $sc_part>0$
 - 506 iii. **EC status:** $ec>0$; $ec_part>0$
 - 507 iv. **CC status:** $cc>0$; $cc_part>0$
(For simulated data, all of the above except those on CC
508 variables are used.)
- 510 (c) **Electromagnetic Calorimeter Cuts** (see Sec. 3.3.1)
- 511 (d) **Osipenko cuts** Cuts on CC angle θ , ϕ and time matching be-
512 tween CC and other detectors. (see Sec. 3.3.2)
- 513 (e) **Cut on minimum number of photoelectrons** (see Sec. 3.3.2)

514 2. Good Event Cuts

- 515 (a) **Cut on minimum number of particles detected and recon-
516 structed in the event:** $gpart>0$
- 517 (b) **Minimum/maximum momentum cuts** (see Sec. 3.3.3)
- 518 (c) **Sector cut** $dc_sect = 6$; $cc_sect = 6$ (to select electrons from the
519 sector where the low momentum Cherenkov detector was installed)
- 520 (d) **Scattering vertex-z cuts** (see Sec. 3.3.4)
- 521 (e) **Fiducial cuts** (see Sec. 3.3.5)

522 This data analysis relied on comparing the experimental data with a
523 Monte-Carlo simulated data set that was as realistic as practically possible.
524 Thus, we also have to analyze the simulated data in the same way as the
525 experimental data. In the ideal situation, all cuts would be the same for
526 both experimental and simulated data. However, we could not make our
527 simulation match perfectly with our experimental data. Therefore, some of
528 the data selection cuts are defined separately for the two cases and sometimes
529 separately even for different Q^2 bins (to make sure we have the same fractions
530 of events in corresponding kinematic bins for both type of data).

531 **3.3.1 Electromagnetic Calorimeter Cuts**

532 The EC cuts consist of two different cuts applied together. One of these
533 is on the sampling fraction i.e. the fraction of the energy deposited in the
534 calorimeter, and the other is on the energy fraction deposited in the inner
535 part of the calorimeter.

536 **Cuts on EC sampling fraction**

537 While moving through the EC, charged pions are minimum ionizing particles
538 in the momentum range detectable by CLAS. On the other hand, each elec-
539 tron deposits its total energy E_{tot} in the EC³ by producing electromagnetic
540 showers. Therefore, the sampling fraction E_{tot}/p should be independent of
541 the momentum for electrons (in reality there is a slight dependence).

³Because some of the deposited energy is in the lead part of the EC rather than the scintillator, only a fraction of the electron energy is detected in the EC.

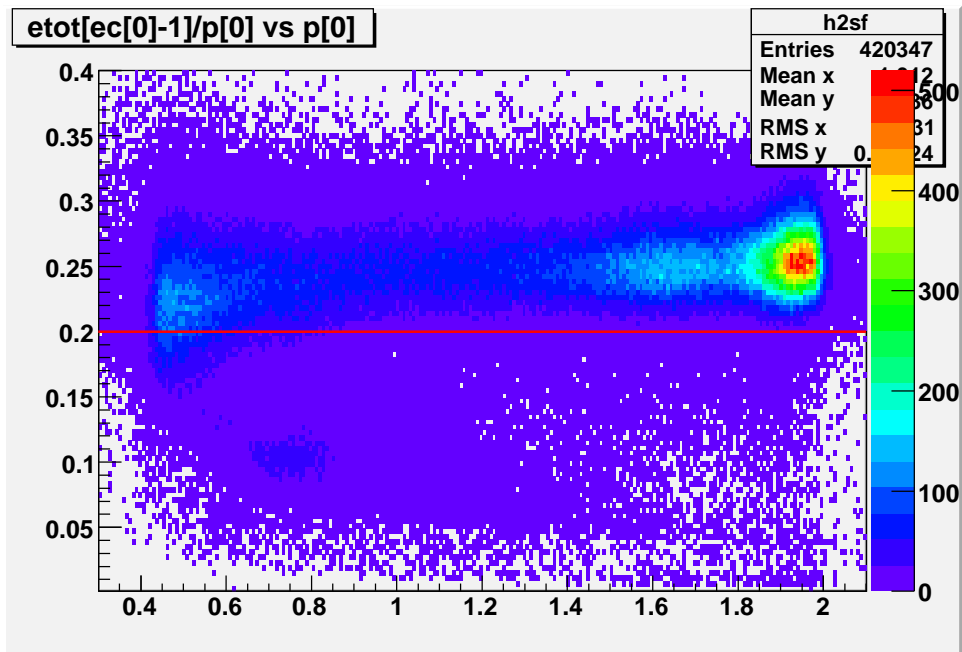


Figure 3.2: An example of the cut on the EC sampling fraction (2.0 GeV data). The plots shows the distribution of the sampling fraction (in Y-axis) plotted against the particle momentum (in X-axis). The brighter stripe above about 0.2 in the energy fraction are due to the electrons whereas those below are the pions.

542 For the EC in CLAS, the electron sampling fraction ($etot/p$) is about 0.25
543 and pions give signals that are mostly below 0.2 (see Fig. 3.2 or others that
544 follow). Therefore, a lower cut of $etot/p > 0.2$ is usually chosen to reject
545 most of the pions without significantly losing good electrons. However, in
546 our low beam energy experiment, few pions are produced and the electron
547 peaks are cleaner in lower kinematic bins as can be seen in the low Q^2 bins
548 of Fig. 3.3. Therefore, a Q^2 bin dependent cut of $etot/p > (\mu - 3\sigma)$ was
549 chosen, where μ and σ are the Gaussian fit parameters representing the mean
550 and standard deviation of the distribution in the corresponding Q^2 bin. The
551 choice of 3σ was decided by looking at the sampling fraction distributions in
552 each of the Q^2 bins and making sure that no pion signal was observed in any
553 of the bins.

554 On simulated data also, a corresponding 3σ cut was applied by first re-
555 peating the exact same procedure to get the corresponding values of μ and
556 σ from the simulated data. Using same- σ cuts in corresponding Q^2 bins of
557 both experimental and simulated data ensures that we had the same fraction
558 of data in corresponding bins from both experimental and simulated sides.

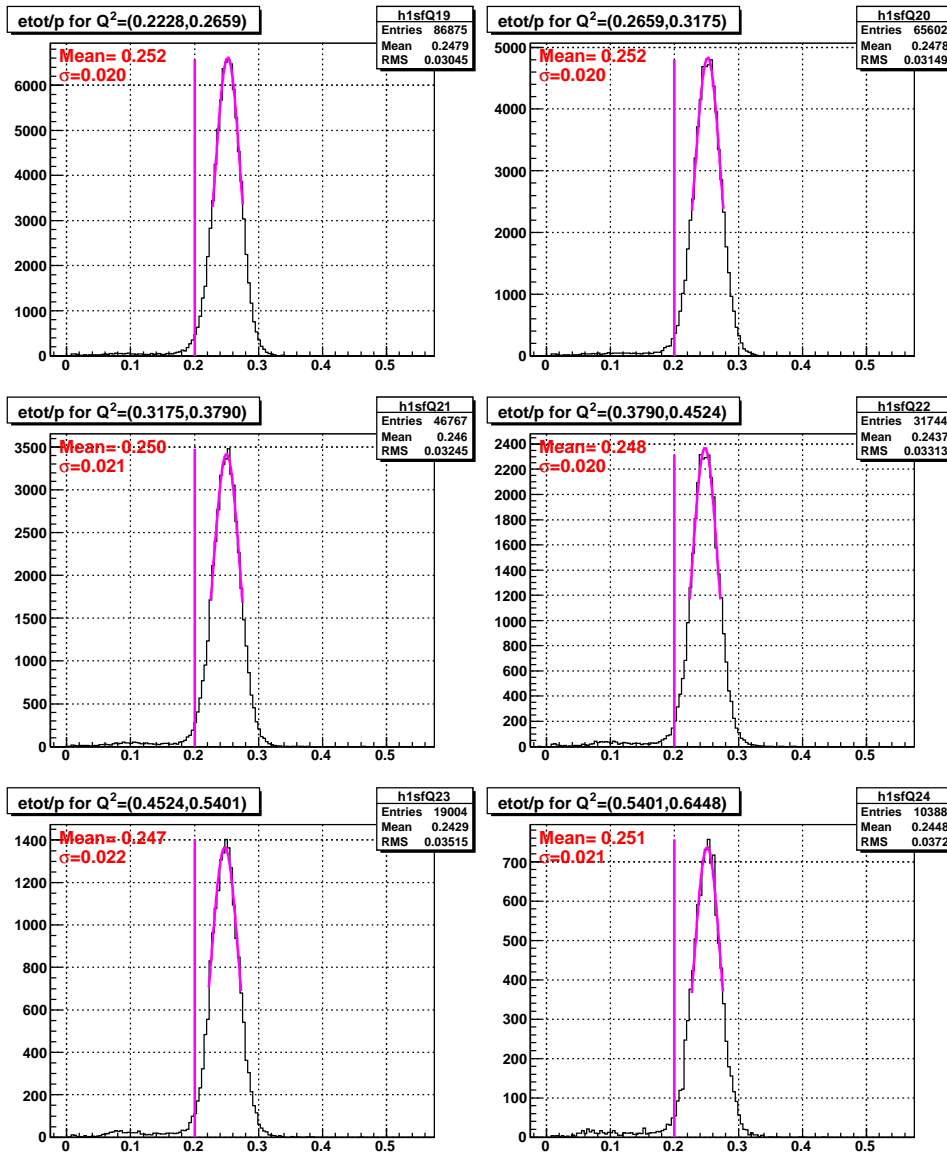


Figure 3.3: The Q^2 dependent cuts on the EC sampling fraction for 2.0 GeV experimental data. Events below the red lines are rejected.

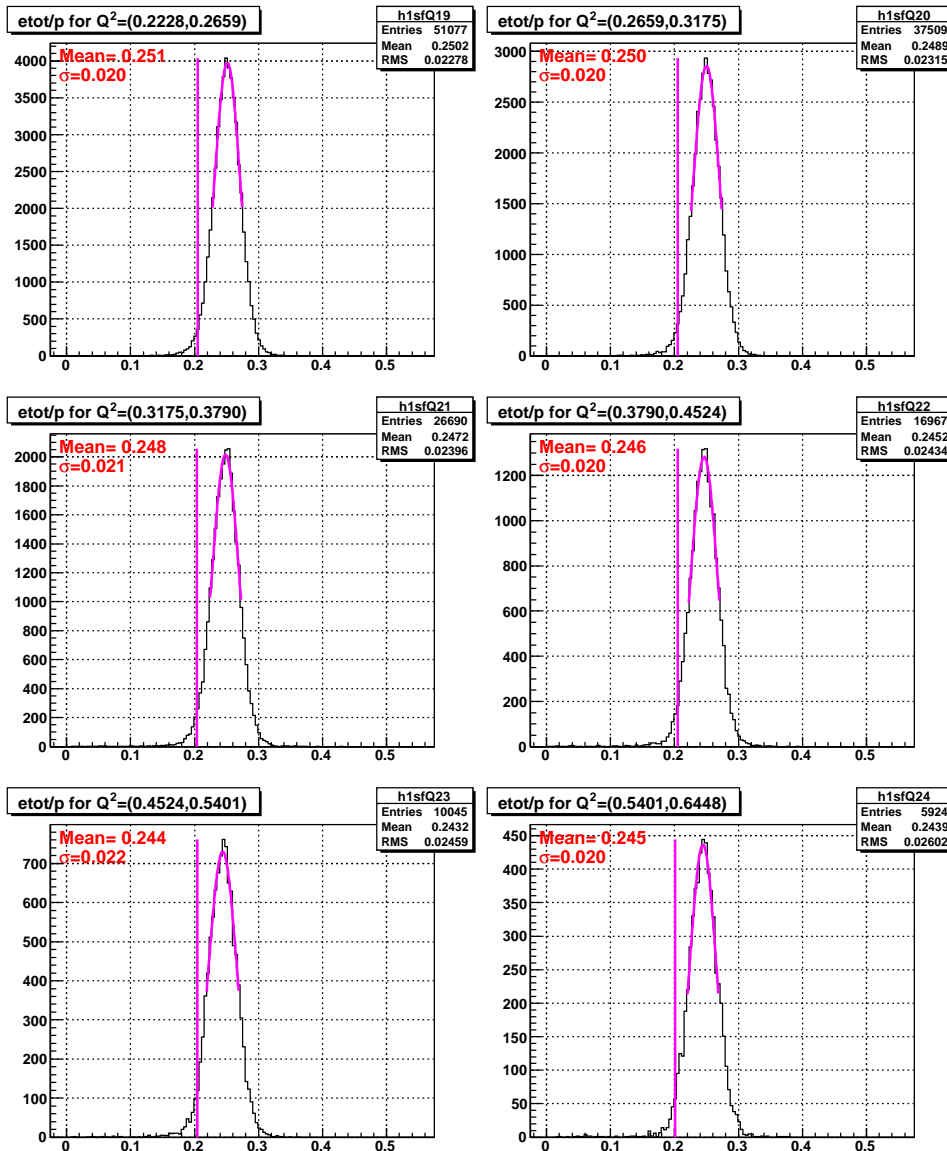


Figure 3.4: The Q^2 dependent cuts on the EC sampling fraction for 2.0 GeV simulation data. Events below the red lines are rejected.

559 Cuts on E_{in}

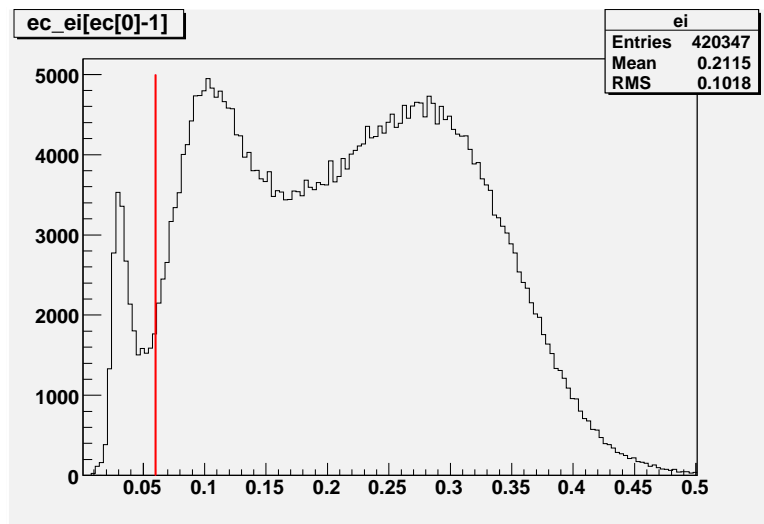


Figure 3.5: Energy deposited (GeV) in the inner EC and the cut (red line) used to reject pions (seen as a peak at about 0.03 GeV) from a sample of electron candidates of 2.0 GeV data.

560 Pions, which do not shower and are minimum ionizing particles in the
561 momentum range detected in CLAS, deposit only a small amount of energy
562 in the inner part of the EC, independent of their momentum. When E_{in} is

563 histogrammed, the small pion signal peak at about 0.03 clearly stands out
564 from the large electron sample, with little overlap in between. So, a universal
565 cut of $E_{in}=0.05$ on both data and simulation (as shown by figures 3.5, 3.6
566 and 3.7) safely rejects most of the pions from the electron candidate sample.

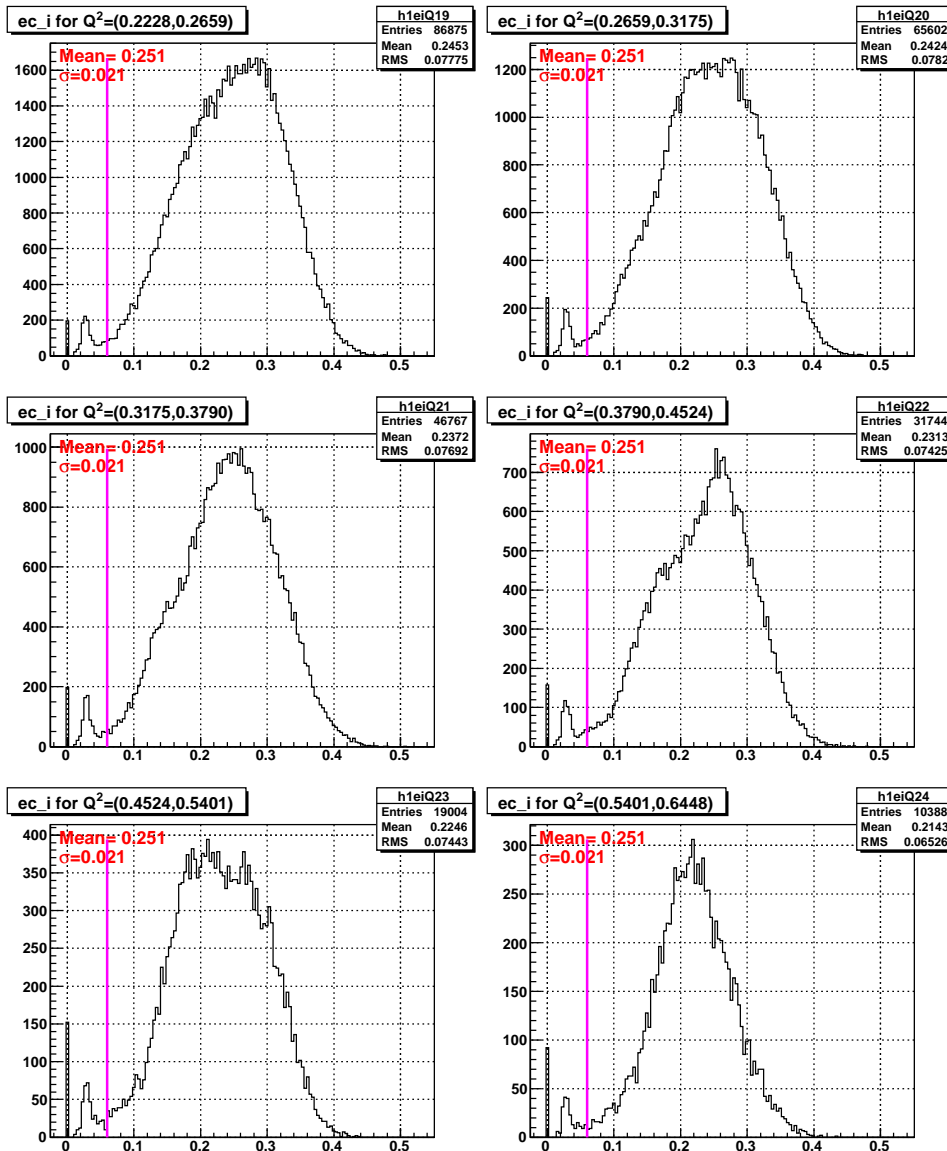


Figure 3.6: The EC-inner cut on a sample of 2.0 GeV experimental data in various Q^2 bins.

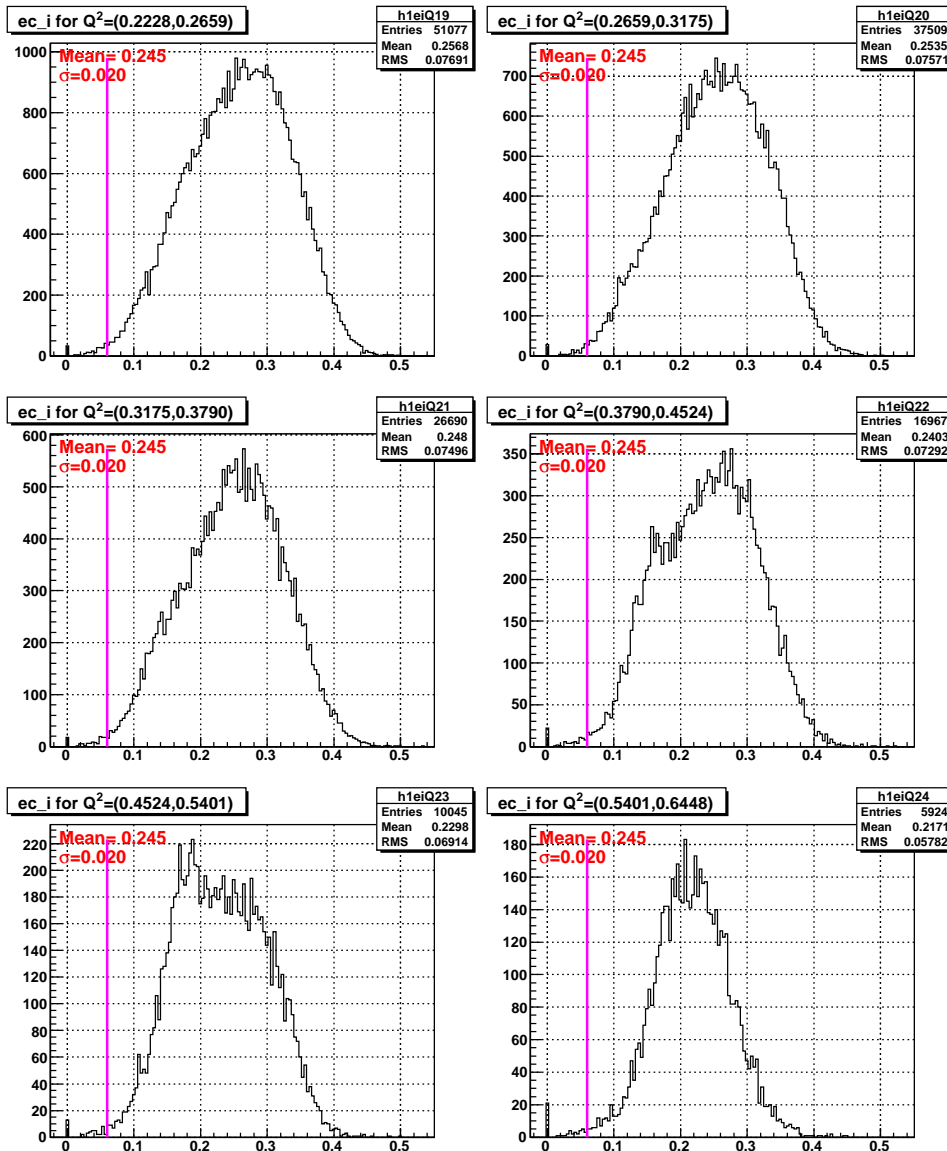


Figure 3.7: The EC-inner cut on a sample of 2.0 GeV simulation data in various Q^2 bins.

567 **3.3.2 Cerenkov Counter Cuts**

568 **Osipenko (CC Geometry and Time Matching) Cuts**

569 As discussed in section 2the new EG4-dedicated CC consists of 11 modules
570 each consisting of a pair of mirrors and PMTs. The segments are placed
571 along the CLAS polar angle covering 15 to 45 degrees, i.e., the segments are
572 at different polar angular positions. During normal operation, the PMTs of
573 these segments may produce thermal noise that is equivalent to that produced
574 by one photo-electron passing through it. As a result, when a noise pulse in
575 the CC and a pion track measured by DC coincides within the trigger window
576 of the CLAS detector, the track gets registered as an electron candidate by
577 the event reconstruction program, thus contributing to the contamination of
578 electron candidates with the misidentified pion tracks. In fact, this turns out
579 to be the biggest source of pion contamination. In order to minimize such
580 contamination and help better identify electrons from pions, CC geometric
581 and time-matching cuts are applied.

582 This category of cuts for this experiment is mostly based on a similar
583 analysis done for another CLAS experiment by M. Osipenko [25].

584 The first requirement in the CC-matching is for the electron candidate
585 track (as reconstructed by DC) to have a corresponding signal in CC. In ad-
586 dition, the track needs to meet several matching conditions to be acceptable
587 as described in the next sections.

588 **CC θ Matching** As said above, the CC segments are at different average
589 polar angle positions (between 15 and 45 degrees), so in principle, one can
590 expect a one-to-one correspondence between the polar angle of the track (as
591 measured at the vertex) and the CC-segment. However, the torus magnetic
592 field bends the particles towards or away from the beamline, so it's more
593 convenient to use the CC projected polar angle θ_{proj} rather than the vertex
594 angle θ , where θ_{proj} is defined as the polar angle of the position vector defined
595 by the point of intersection of the track with the plane at which the CC
596 PMTs reside as reflected by the CC mirrors (another projected angle ϕ_{proj}
597 is the azimuthal angle of the same vector). These projected angles can be
598 uniquely calculated for each track based on the DC signals of the track as
599 well as the CC geometry information. To simplify the later analysis process,
600 these projected angles for each track were calcuated during the final data
601 reconstruction process and then saved in the output files just like all the other

602 information for the events and particles. Finally, for the actual electrons
 603 a one-to-one correspondence between θ_{proj} and the segment number can be
 604 established, which discriminates against background noise and the accidental
 605 pions (or any other negative charge candidates). For each segment, the θ_{proj}
 606 distribution (see Fig. 3.8) is fitted with a gaussian to determine its mean (μ)
 607 and width (σ) and then saved for future use in cuts. These fit parameters
 608 are then used during the data analysis to define these CC- θ -matching cuts.
 609 The events that have $\mu - 3\sigma < \theta_{proj} < \mu + 3\sigma$ pass this cut, and the others
 610 are rejected as not genuinely being electrons.

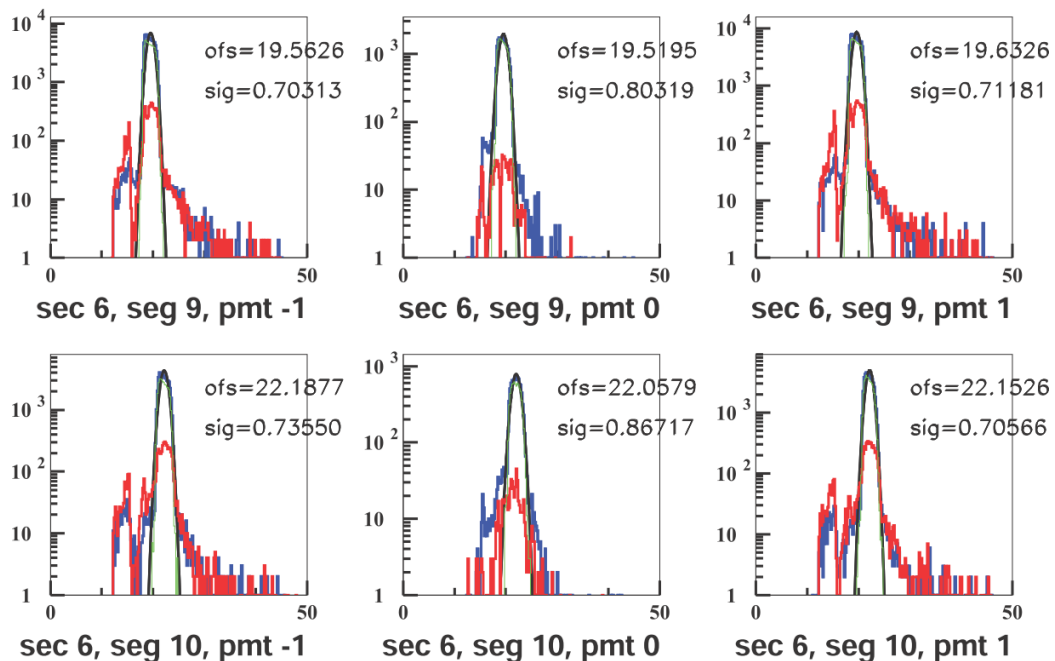


Figure 3.8: The θ_{proj} distributions in two (9th and 10th) of the CC-segments (figures used from [26]). Here, the first, second and third columns correspond to events that fired the left, both and the right PMTs respectively. The blue lines are for good electron candidates that pass the EC cuts as well as $Nphe > 2.5$. The red ones are for those that pass the EC cuts but with $Nphe < 2.5$ (thus likely pions), and the green are for those which pass both EC cuts and all Osipenko cuts. The Gaussian fits which are used to define the θ matching cuts are shown in black ("ofs" and "sig" in the panel refer to μ and σ , respectively). If the candidate falls outside $\pm 3\sigma$ limits given by the fit, θ_{proj} is taken as not matching with the corresponding segment and, therefore, the event is rejected.

611 **CC ϕ Matching** One can also have a one to one correspondence between
612 the other CC-projected angle ϕ_{proj} and the left or right PMT in the corre-
613 sponding CC-segment, because when the track is on the right side of the CC,
614 the right PMT should fire and vice versa. However, there are some excep-
615 tional cases of events which fire both PMTs. That happens when ϕ_{proj} of the
616 track is less than 4 degrees (when measured relative to the sector mid-plane),
617 in which case the Cerenkov light hits both PMTs but with less efficiency (be-
618 cause the Cherenkov photons are shared between the two). Fig. 3.9 shows
619 for two of the segments the ϕ_{proj} distributions and the Gaussian fits that are
620 used to define these cuts.

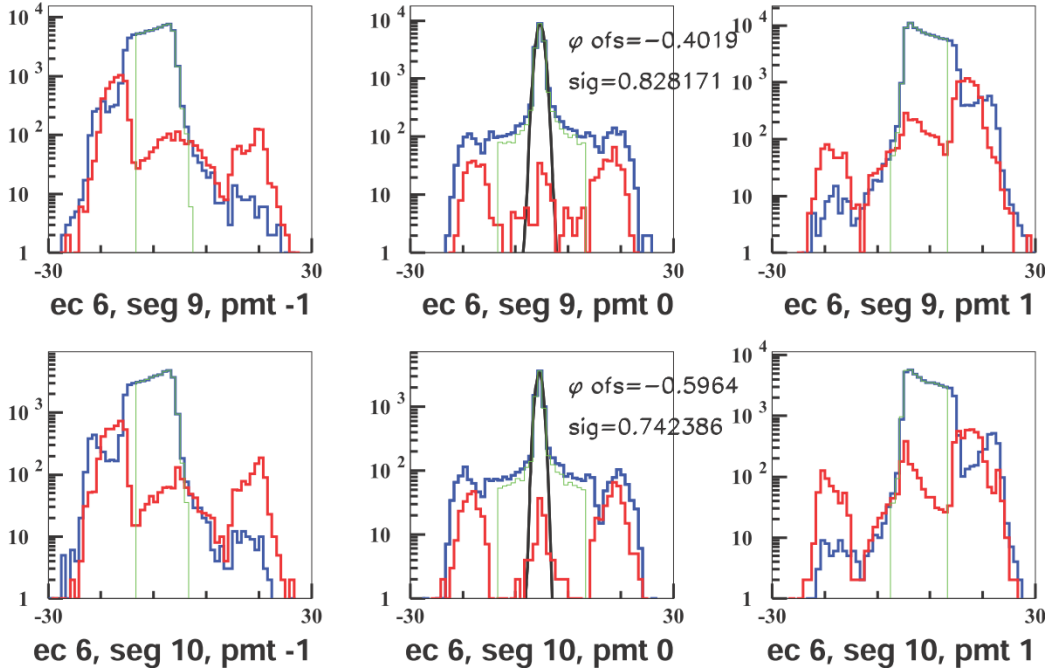


Figure 3.9: The ϕ_{proj} distributions in two (9^{th} and 10^{th}) of the CC-segments (figure used from [26]). Here, the first, second and third columns correspond to events that fired the left, both and the right PMTs respectively. The blue lines are for good electron candidates that pass the EC cuts as well as $Nphe > 2.5$. The red ones are for those that pass the EC cuts but with $Nphe < 2.5$ (thus likely pions), and the green are for those which pass both EC cuts and all Osipenko cuts. The Gaussian fits to the distributions that fired both left and right PMTs are shown in black ("ofs" and "sig" in the panel refer to μ and σ , respectively). If the candidate falls outside 3σ on the positive (negative) side but the left (right) PMT is fired, we take it as having left-right inconsistency and, therefore, the event is rejected. In other words, if $\theta < \mu - 3\sigma$ but $PMT = 1$, or if $\theta > \mu + 3\sigma$ but $PMT = -1$, the event is rejected.

621 **CC Time Matching** The difference ΔT between the track time recorded
 622 on a CC segment and the corresponding time recorded on the TOF (or SC),
 623 corrected for the path length from the CC to the TOF, is used to define one of
 624 the time-matching cuts $\Delta t_{SC-CC} > -6.0\text{ns}$ which was chosen to reduce pion
 625 contamination without losing too many electron candidates (see Fig 3.10).
 626 Likewise, the time between CC and EC is also used to define another cut
 627 $\Delta t_{EC-CC} > -6.0\text{ns}$ (see Fig 3.11) to further reduce the pion contamination.

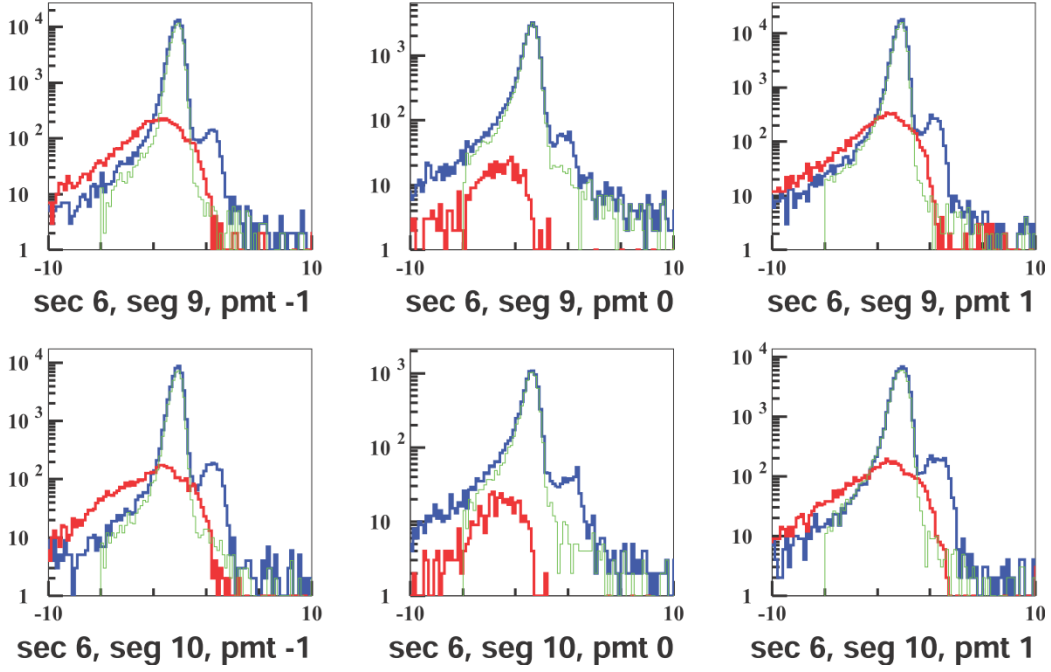


Figure 3.10: The Δt_{SC-CC} distributions for two of the CC-segments (figure used from [26]). Here, the first, second and third columns correspond to events that fired the left, both and the right PMTs respectively. The blue lines are for good electron candidates that pass the EC cuts as well as $Nphe > 2.5$. The red ones are for those that pass the EC cuts but with $Nphe < 2.5$ (thus likely pions), and the green are for those which pass both EC cuts and all Osipenko cuts. The $\Delta t_{SC-CC} > -6.0\text{ns}$ cut was chosen to reduce pion contamination without losing too many electron candidates. (The small peaks at about +3 ns are due to particles hitting PMTs directly.)

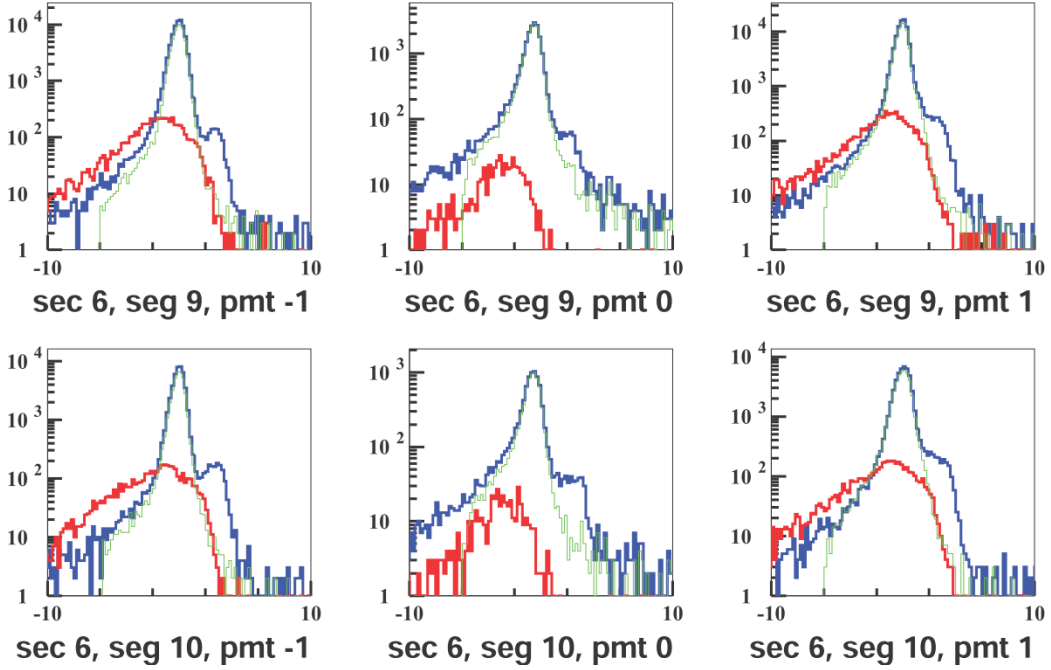


Figure 3.11: The Δt_{EC-CC} distributions for two of the CC-segments (figure used from [26]). Here, the first, second and third columns correspond to events that fired the left, both and the right PMTs respectively. The blue lines are for good electron candidates that pass the EC cuts as well as $Nphe > 2.5$. The red ones are for those that pass the EC cuts but with $Nphe < 2.5$ (thus likely pions), and the green are for those which pass both EC cuts and all Osipenko cuts. The $\Delta t_{EC-CC} > -6.0\text{ns}$ cut was chosen to reduce pion contamination without losing too many electron candidates. (The small peaks at about +3 ns are due to particles hitting PMTs directly.)

628 Cut on Minimum Number of Photoelectrons

629 The “nphe” variable in the data ntuple which represents the ADC signal from
 630 the CC converted to “number of photoelectrons” and multiplied by 10 is also
 631 used to discriminate electrons from pions and the background. The number
 632 of photoelectrons produced in CC by an electron is typically between 5 and 25
 633 or between 50 and 250 in the units of nphe, where the electronic background
 634 and negative pions produce signals equivalent to one photo-electron (or 10 in
 635 nphe units) and so a cut is determined somewhere between these two regions
 636 based on the shapes and sizes of the electron and pion peaks. In our case,

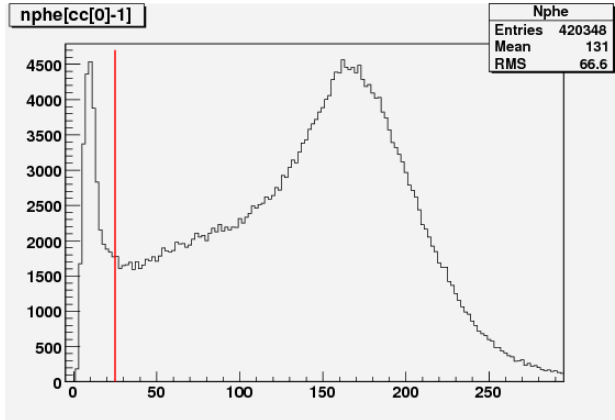


Figure 3.12: The cut (the red straight line at 25) on the number of photo-electrons produced in CC times 10 (from 2.0 GeV data). The signals below the red line are mostly pions and noise and above the line are mostly electrons.

637 we chose to have the cut $Nphe > 25$ as depicted by the straight line in Fig.
 638 3.12.

639 3.3.3 Minimum/Maximum Momentum cuts

640 A study [27] of the inclusive cross section at various beam energies in CLAS
 641 developed a parametrization of the low momentum cut p_{min} as a function of
 642 the calorimeter low trigger threshold (in milli-Volts)

$$p_{min} \text{ (MeV)} = 214 + 2.47 \times EC_{threshold} \text{ (mV)} \quad (3.2)$$

643 The low threshold for EC-total energy for EG4 was 65 mV [28], so, the
 644 minimum momentum cut was determined to be at: $p_{min} = 0.37 \approx 0.4 \text{ GeV}$.
 645 In addition, another minimum cut of $p_{min} = 0.2 * E_{beam}$ was added, so the
 646 actual minimum cut amounted to the larger of those two. Likewise, the
 647 momentum cannot be more than that of the beam energy (in natural units),
 648 therefore, the upper cut on the momentum is: $p_{max} = E_{beam}$.

649 Fig. 3.13 shows the momentum distribution of the electron candidates
 650 for the 2 GeV data and the minimum and maximum cuts.

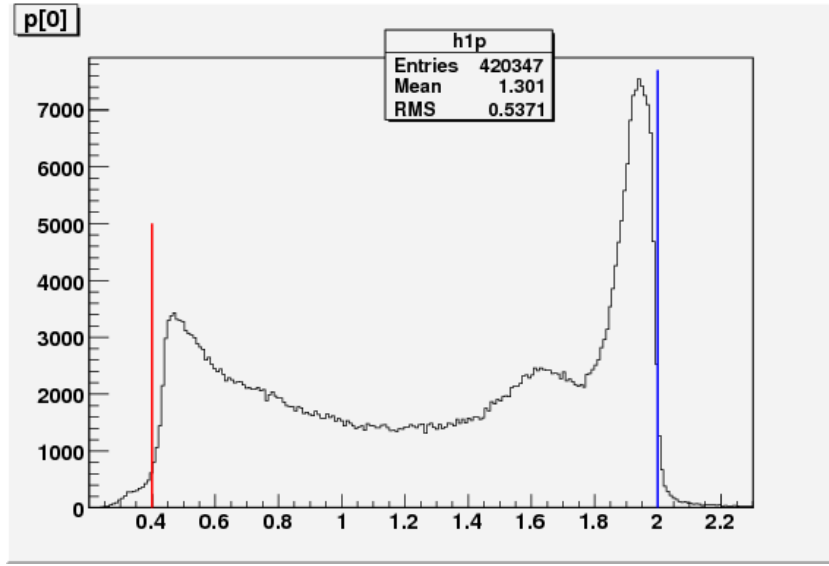


Figure 3.13: The maximum and minimum momentum cuts (on 2.0 GeV ND₃ data).

651 3.3.4 Vertex-Z cuts

652 In the EG4 experiment, the ND₃ polarized target was of 1 cm long and was
 653 placed at ($x = 0$, $y = 0$, $z = -100.93$ cm) in the CLAS coordinate system.
 654 Since the beam electrons have to go through a few foils before reaching the
 655 target as well as the detector, we want to reject electron tracks with vertices
 656 outside the target volume. For this purpose, use a cut on the reconstructed
 657 vertex co-ordinate “ v_z ”. However the vertex resolution demands reasonably
 658 wide “ v_z ” cuts so as not to lose too many good events. That is why the
 659 distribution of “ v_z ” was studied and based on the position and width of
 660 the distribution as well as our knowledge of the location of various foils and
 661 target materials, the cuts on “ v_z ” were decided. It was seen (see Figs. 3.14
 662 and 3.15) that the resolutions get worse and the distributions get wider as
 663 we go to lower Q^2 values, so again Q^2 dependent cuts were chosen for both
 664 data and simulation with the cuts tightening as Q^2 increases.

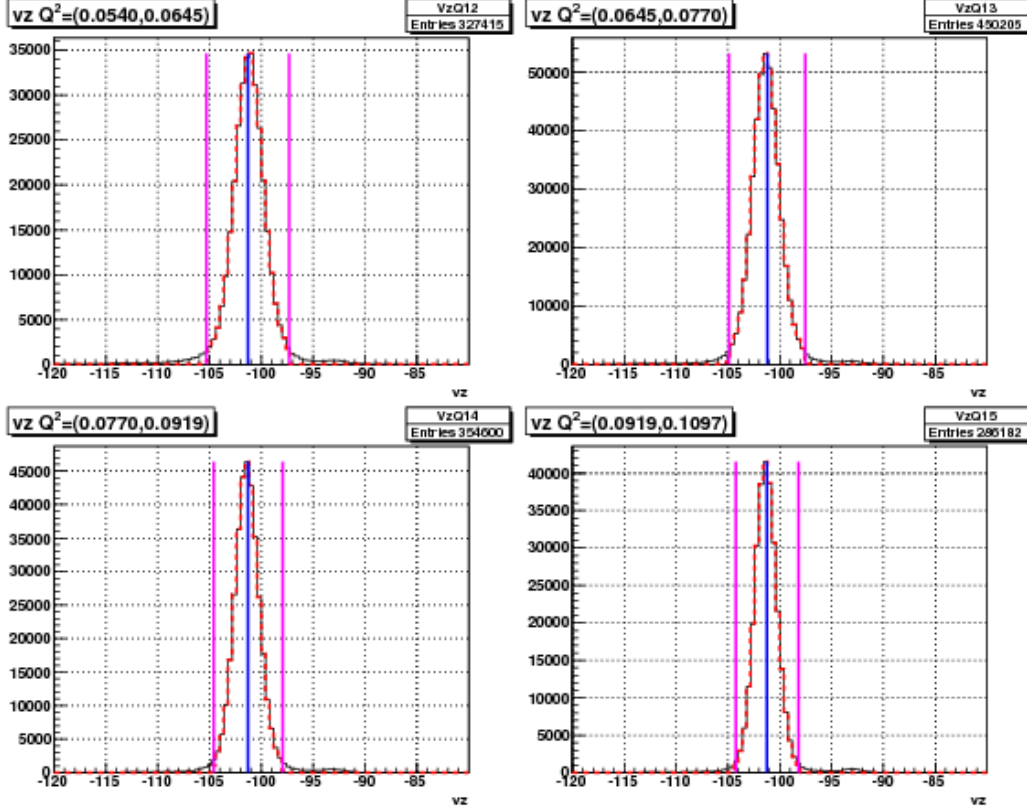


Figure 3.14: 2.0 GeV data showing the Q^2 dependent v_z -cuts (the magenta lines on the left and right of the peaks) in some of the Q^2 bins. The continuous black line represents events before applying all the other event selection cuts (except on v_z) and the thicker dotted red line are the events after the cuts. The blue lines are the centers of the distributions, from which the cuts are 3 times σ away on each side, where σ is the standard deviation for the distribution in the given Q^2 bin (both the central value and the σ are determined during the cut development studies).

665 As in the case of EC variables, the reconstructed “ v_z ” distribution in
 666 the simulation does not come out quite the same as in the experimental
 667 data . To have the same fraction of events in the corresponding Q^2 bins as
 668 in the experimental data, a separate set of cuts (determined based on the
 669 distributions of both types of data) had to be used for simulation. For this
 670 purpose, the Gaussian fit parameters μ and σ (representing the mean and
 671 standard deviation) for all the Q^2 bins were tabulated separately for both

672 data and simulation and separate sets of $\pm 3\sigma$ cuts were determined for all
 673 bins. For example, if μ_q and σ_q were the two Gaussian fit parameters for the
 674 q^{th} Q^2 bin of either data or simulation, then the lower and upper cuts for
 675 “ v_z ” for that data set in the given Q^2 bin would be $\mu_q - 3\sigma_q$ and $\mu_q + 3\sigma_q$
 676 respectively (as shown by the magenta vertical lines in Figs. 3.14 and 3.15).

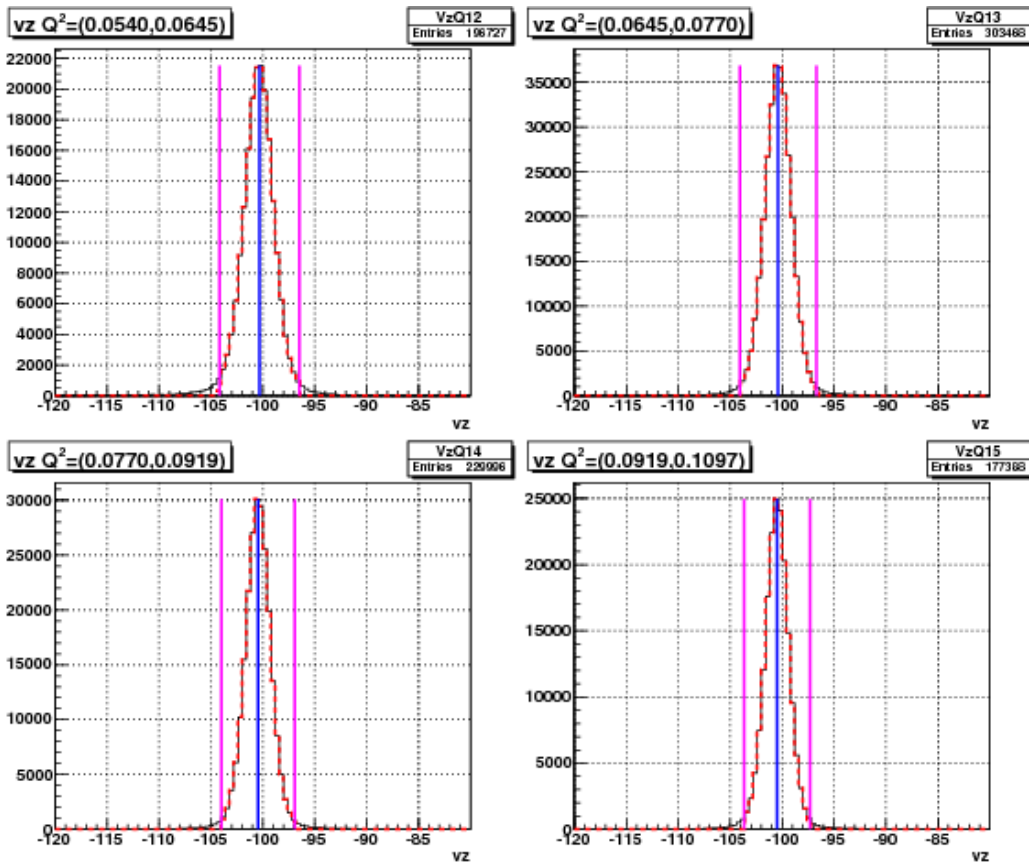


Figure 3.15: Q^2 dependent v_z -cuts on simulation data (similar to Fig. 3.14).

677 3.3.5 Fiducial Cuts

678 Similar to the cuts discussed so far, we also had to match the region of good
 679 efficiency of the physical detector with the corresponding region from the
 680 simulation. For the experimental and simulation data to be comparable,
 681 they must have the same detector acceptance. Two event variables polar

682 angle (θ_{vtx}) measured at the vertex and the azimuthal angle ϕ_{DC1} measured
 683 at the drift chamber layer 1 are chosen to define the good efficiency regions of
 684 the detector. The reason for the choice of the variable θ_{vtx} should be obvious
 685 because it is directly related with the kinematic variables Q^2 and W used in
 686 the analysis. However, due to the momentum dependent rotational effect of
 687 the magnetic field on the reconstructed azimuthal angle (ϕ_{vtx}) at the vertex,
 688 the angle ϕ_{DC1} is preferred over ϕ_{vtx} to define the fiducial region because
 689 that allows the easy selection (rejection) of the events which passed through
 690 and got detected by the more (less) reliable central (marginal) regions of
 691 the Cerenkov Counters. After a careful and extensive study of the event
 692 distributions on both data and simulation, we arrived at four sets of fiducial
 693 cuts in terms of the variables θ_{vtx} , ϕ_{DC1} and the torus current normalized
 694 inverse momentum i.e., $I_{torus}/(2250p)$.

695 The first set of fiducial cuts (see Fig. 3.16) were determined by comparing
 696 regular and EC-only data (which were taken using triggers that didn't
 697 involve CC) and selecting cuts such that regions with relatively darker spots
 698 (reflecting very low CC-efficiency) were rejected.

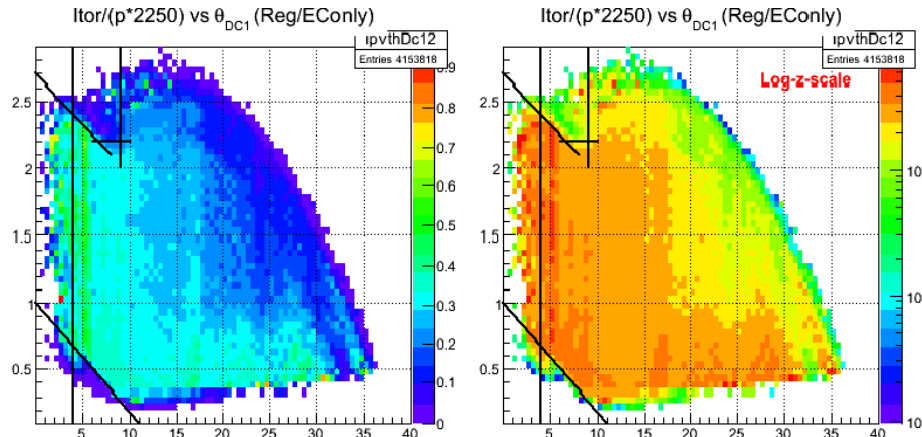


Figure 3.16: Fiducial cuts determined by comparing the distributions of regular and EC-only **experimental data** as a function of $I_{torus}/(2250p)$ and θ_{DC1} . Here in the top panels, we see distributions of ratios of the regular and EC-only data respectively in linear and log scales in the color axis respectively. Inefficient regions of the CC are excluded using the indicated cuts.

699 The second set of cuts came from a similar comparison between the regu-
 700 lar and EC-only data in the $I_{torus}/(2250p)$ vs θ_{vtx} (instead of θ_{DC1}) space (see

701 Fig. 3.17) .

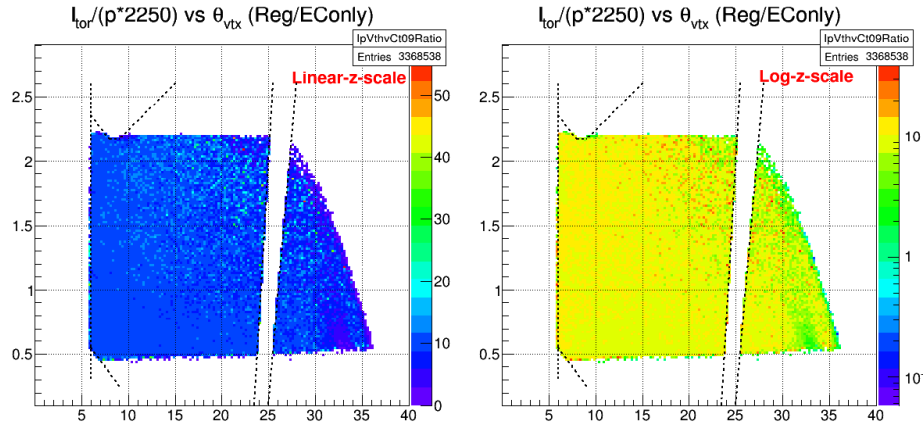


Figure 3.17: Fiducial cuts determined by comparing the distributions of regular and EC-only **experimental data** as a function of $I_{torus}/(2250p)$ and vertex angle θ_{vtx} . Here, the vertical cut near $\theta_{vtx}=25$ degrees is to avoid the region of low efficiency possibly due to dead wires in DC.

702 The third set of cuts came from a comparison between the experimental
703 and the corresponding simulated data as shown in the Fig. 3.18. as indicated
704 by various straight lines in the two plots.

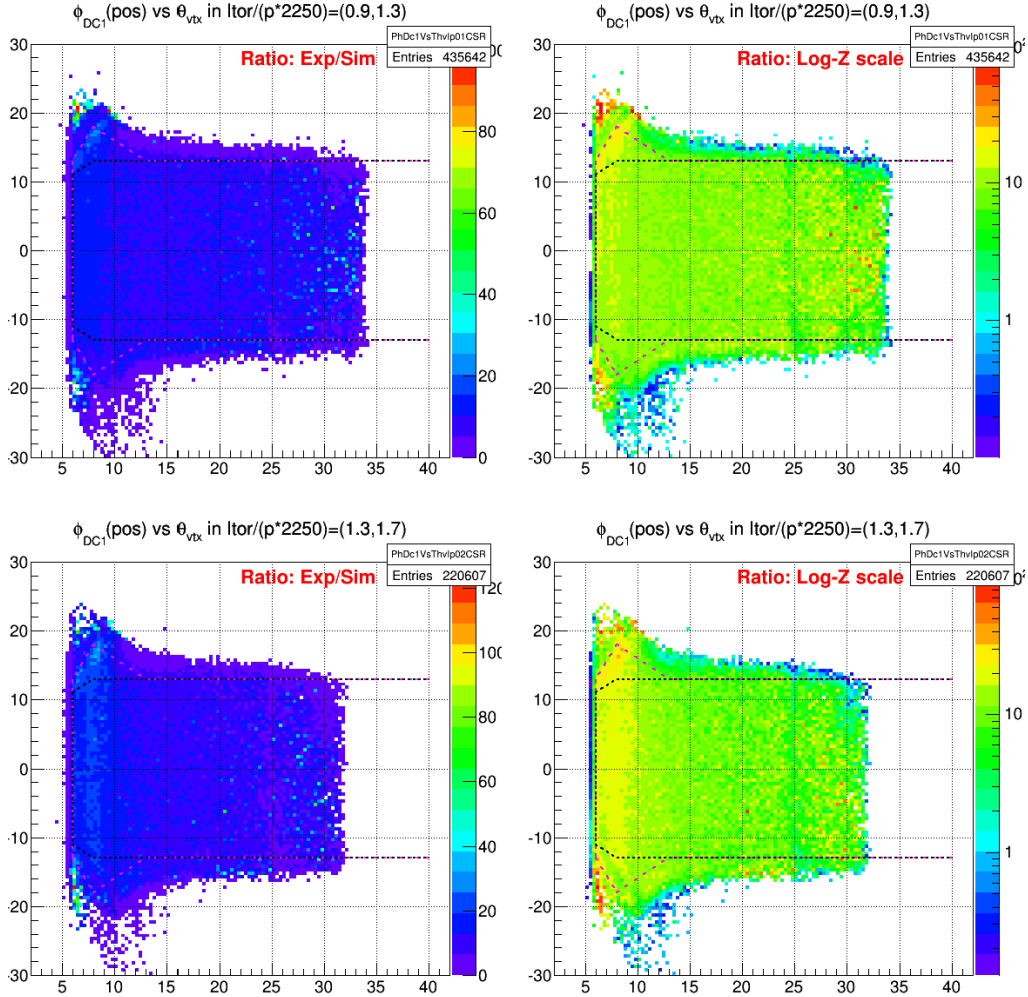


Figure 3.18: Distribution (in two of six bins of $I_{torus}/(2250p)$) of ratios of **experimental** and **simulated** data (for 2.0 GeV) (both in linear and log-z scales) as a function of vertex angle θ and azimuthal angle ϕ_{DC1} as measured by the track position at the first drift chamber layer (angles in degrees). The dotted lines indicate the fiducial cuts for accepting good electrons.

705 Lastly, further sets of cuts were developed based on the distribution of average
 706 number of photo electrons (nphe) as recorded by the Cerenkov Counter
 707 (CC) (see Fig. ??).

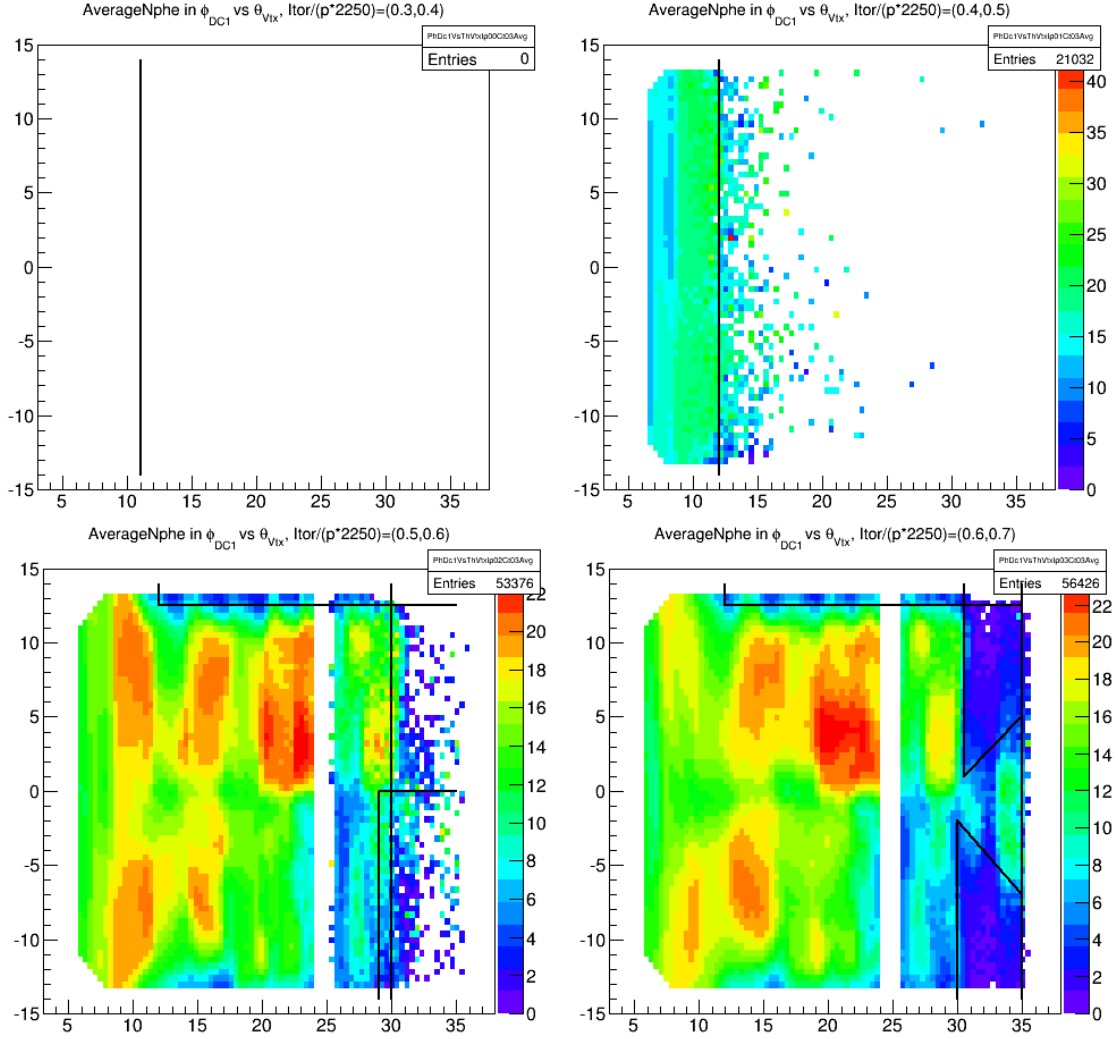


Figure 3.19: Average Nphe distributions as a function of ϕ_{DC1} (along Y-axis) and θ_{vtx} (along X-axis) in first four bins of $\frac{I_{tor}}{p \cdot 2250}$. The black lines show the cuts that reject the very low CC-inefficiency regions.

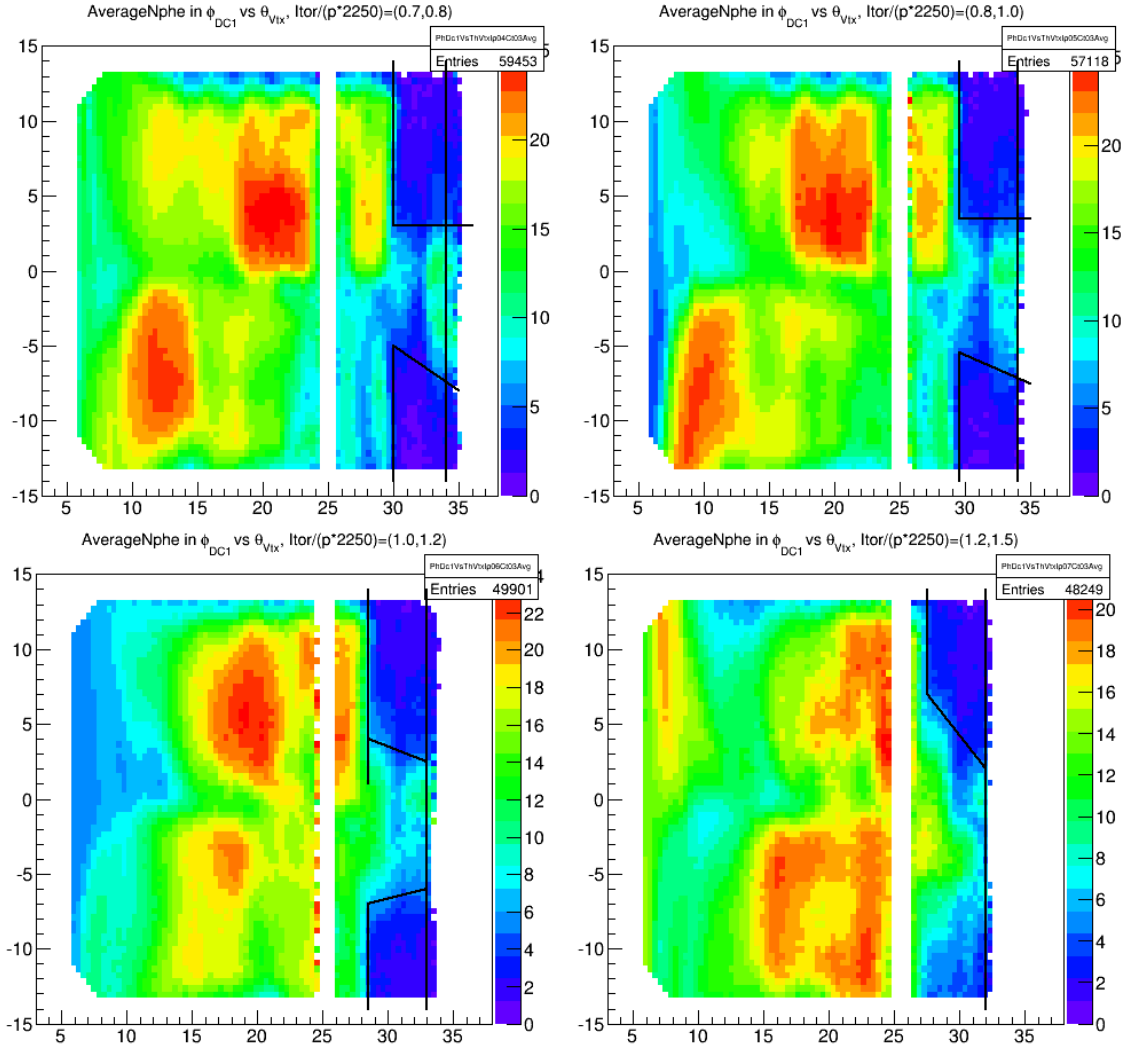


Figure 3.20: Average Nphe distributions as a function of ϕ_{DC1} (along Y-axis) and θ_{vtx} (along X-axis) in next four bins of $\frac{I_{tor}}{p \cdot 2250}$. The black lines show the cuts that reject the very low CC-inefficiency regions.

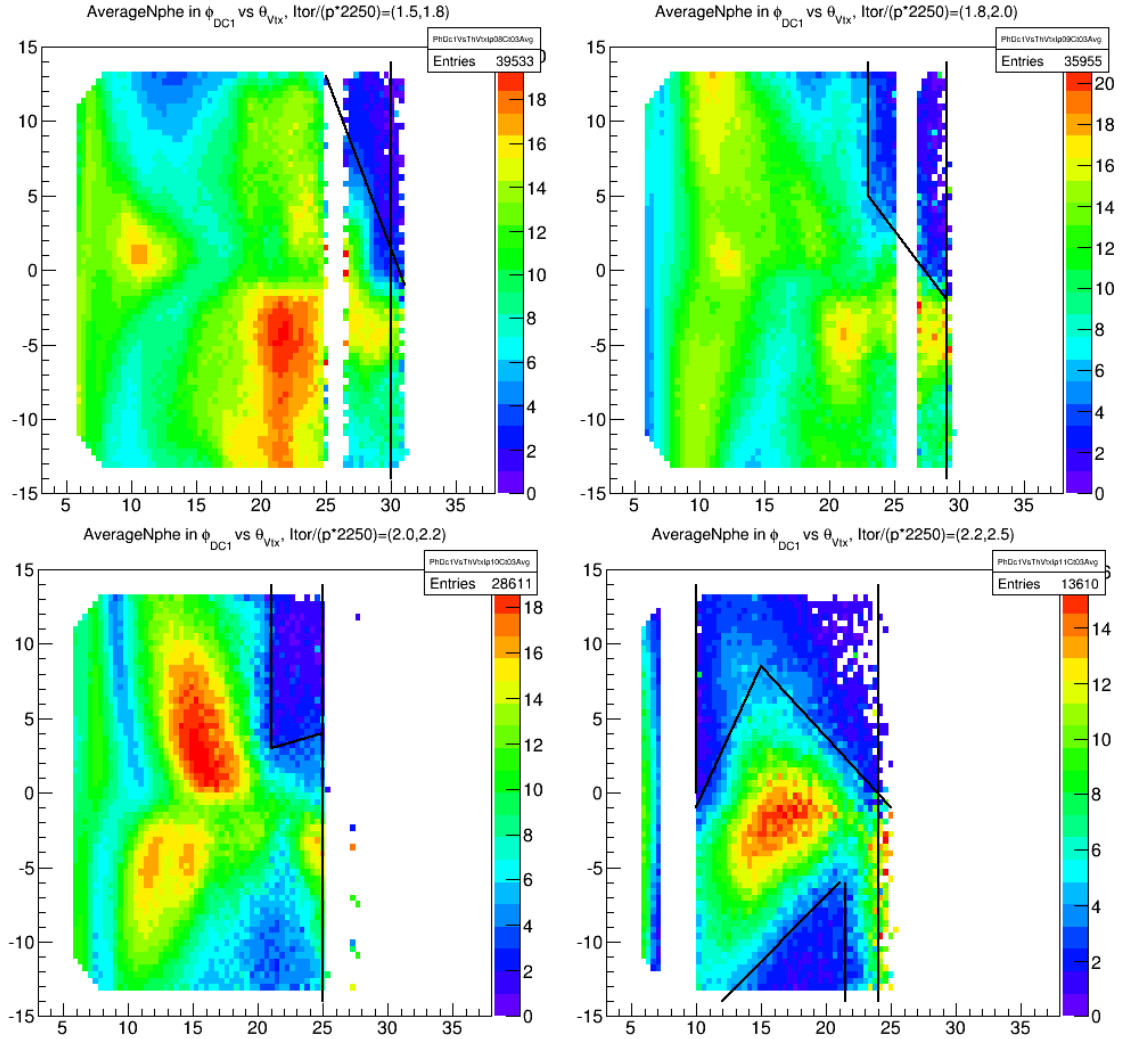


Figure 3.21: Average Nphe distributions as a function of ϕ_{DC1} (along Y-axis) and θ_{vtx} (along X-axis) in last four bins of $\frac{I_{tor}}{p \cdot 2250}$. The black lines show the cuts that reject the very low CC-inefficiency regions.

708 3.4 Data Quality and Stability Checks

709 With an available set of good event/electron selection cuts, beam charge
710 (measured by Faraday cup) normalized total event counts (sometimes also
711 known as event “yield”), as well as polarization dependent differences, were
712 calculated for each of the data files for all the runs and then plotted against
713 the run number to study the data quality and stability as shown by Figs.
714 3.22, 3.23 and 3.24.

715 If nothing unusual happened or if the experimental conditions are not
716 changed, then it is expected that the event yield as well as the count differ-
717 ences remain constant over time. Therefore, the graphs of these event counts
718 plotted versus time or run number (which also roughly reflect the flow of
719 time) should indicate the stability and quality of the data collected. For
720 example, Fig. 3.22 shows such a total yield plot for all the data files from
721 the 2.0 GeV beam energy data set on deuteron target. We can see that these
722 data runs display some features of instability over the full period of time, but
723 stability over short time periods. For example, all the data with run numbers
724 below about 51610 show significantly higher event yield than the runs after
725 that run (possibly due to beam-target misalignment as indicated by raster
726 magnet ADC values in Fig 3.24).

727 Likewise, the stability of the polarized count differences in the elastic
728 region ($0.9 \text{ GeV} < W < 1.0 \text{ GeV}$) as well as separately in the delta (Δ)
729 resonance region were studied by plotting them versus the same run numbers
730 (here the elastic and Δ -resonance regions are considered separately, because
731 the spin asymmetries in these two regions have opposite signs, which would
732 have decreased the observed difference if combined. To further enhance the
733 sensitivity of the observation, the difference of the count differences measured
734 in the elastic and Δ -resonance regions as given by

$$\Delta N_{elastic} - \Delta N_{\Delta-res} = \frac{1}{P_b P_t} \left[\left(\frac{N^+}{FC^+} - \frac{N^-}{FC^-} \right)_{elastic} - \left(\frac{N^+}{FC^+} - \frac{N^-}{FC^-} \right)_{\Delta} \right] \quad (3.3)$$

735 were plotted (see Fig. 3.23). It was observed that this elastic normalized
736 count difference (which is what really matters to our analysis, in the end)
737 was much more stable than the total yield.

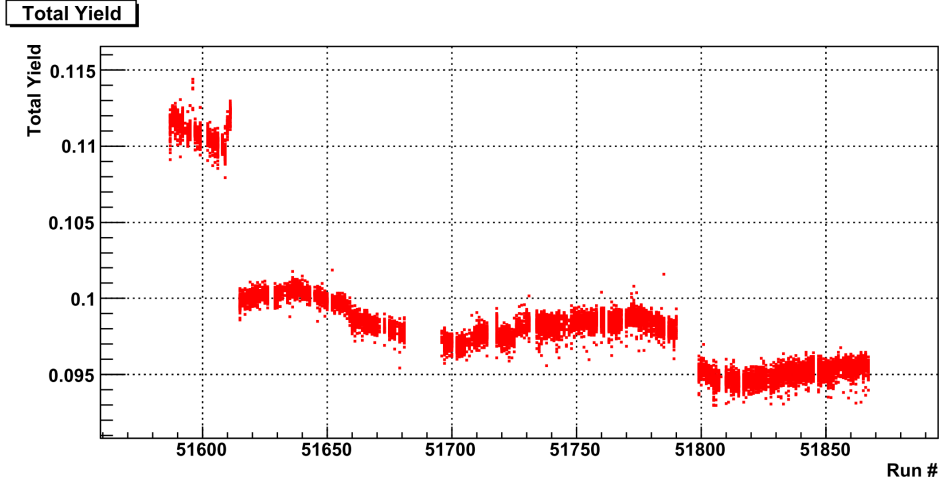


Figure 3.22: Total normalized yield ($= \frac{N^+ + N^-}{FC^+ + FC^-}$) for 2.0 GeV ND₃ runs.

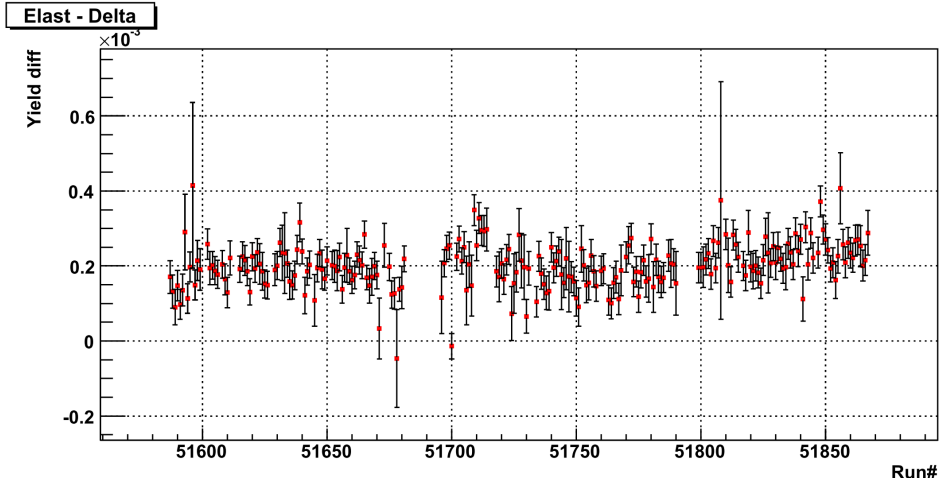


Figure 3.23: Polarized yield differences (Eq. 3.3) normalized with $P_b P_t$ and BPM/F-cup for elastic peak minus that for the Δ peak for the 2.0 GeV ND₃ runs.

738 The same was also repeated for the other variables such as the root-
 739 mean-square of the ADC values (see Fig. 3.24) which carry information on
 740 the X and Y coordinates of the beam at the interaction vertex, thus their
 741 plots giving us somewhat more direct information on whether there was any
 742 misalignment between the beam and the target.

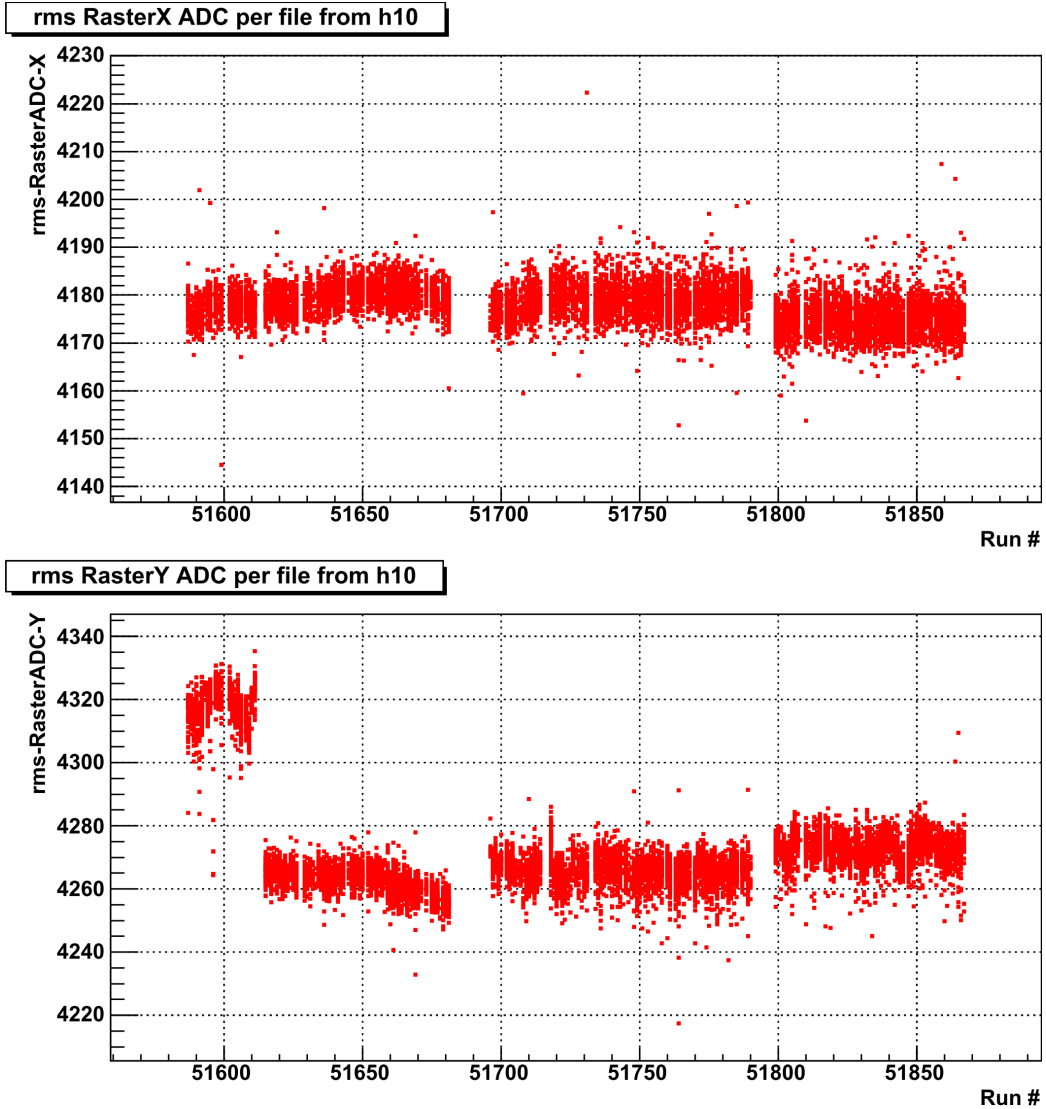


Figure 3.24: Root-mean-square of the ADC values for the raster magnet currents in the directions X and Y. The distributions show a larger raster size in the y-direction for the first group of runs, indicating that the beam may have been hitting the edges and the walls of the target or other more dense structure support materials, thus explaining the higher total yield for the corresponding runs as shown by the Fig. 3.22. This does not affect our final analysis because these off-target materials are not polarized and, hence, do not contribute to the polarization dependent count difference (ΔN) used in the final analysis.

743 Based on the studies of these quality and stability plots, the data runs
744 were divided into subgroups with each beam energy data set. In each sub-
745 group, the data showed more stability than over the whole run period for
746 the given beam energy. For example, in case of the 2.0 GeV deuteron data,
747 the runs were divided into four distinct sub groups corresponding to the four
748 separate bands as seen in the Fig. 3.22. These subgroups were later treated
749 and analyzed separately to get the corresponding normalized polarized count
750 differences (with all data runs from each subgroup combined together). After
751 the initial combination within the subgroups, they were again combined into
752 the grand total by properly considering the half-wave-plate status, and the
753 target polarization directions.

754 **3.5 Kinematic Corrections**

755 The reconstructed event vertices and associated particle 4-momenta are slightly
756 off from their true values for several reasons. First, RECSIS does not take
757 into account the fact that the beam is rastered in polarized target experi-
758 ments. Next, any imperfections and mis-alignments of detectors and other
759 components of the experimental set-up are not accounted for. Furthermore,
760 the torus field map is not known precisely. In addition, the effects of multiple-
761 scattering and particle energy losses are not considered in RECSIS. There-
762 fore, to get more accurate results from the data analysis, the data quality
763 must be improved by applying various kinematic corrections. Following is
764 the list of the corrections that were applied for the analysis:

- 765 1. Incoming (beam) energy loss correction (due to ionization)
- 766 2. Tracking corrections
- 767 3. Drift chamber dependent momentum correction
- 768 4. Outgoing energy loss correction (due to ionization after scattering)

769 **3.5.1 Incoming Energy Loss Correction**

770 The first correction listed above considers the loss of beam energy due to
771 atomic collisions before the actual nuclear scattering takes place. A good
772 estimate for this loss is 2 MeV on average [29, 30], which is subtracted from

773 the nominal beam energy. This correction is applied during the analysis
774 whenever the beam energy is involved⁴, and therefore it is not included in
775 the correction package described below.

776 3.5.2 Tracking Corrections

777 This work is mostly based on the work documented in the EG1-DVCS-TN-
778 004 by P. Bosted [?], in which a routine or method is developed to swim the
779 particles through the field map of the target magnet to the drift chambers in
780 order to determine the particle angles and position at the target, provided
781 the direction cosines of the tracks at DC and the beam position from the
782 raster magnets are known. It is expected that the method improves both the
783 angular resolution and the reconstructed longitudinal vertex position. The
784 slightly modified version of the corresponding C/C++ routine is used with
785 some of the constants in the routine replaced by new parameters to be deter-
786 mined by the method of **χ^2 -square minimization** using ep-elastic events.
787 (Since this data set didn't have enough e^+e^- pairs, we didn't use them in
788 the minimization like in the EG1DVCS.)

789 Method

790 First of all, in order to convert raster magnet ADCs into corresponding beam
791 positions x_0 and y_0 , we need conversion parameters. These parameters are
792 determined by using a method outlined in EG1-DVCS-TN-002. The method
793 determines the values of the slopes and offsets that convert the X- and Y-
794 raster ADC readings to corresponding beam positions x_0 and y_0 in cm by
795 minimizing the sensitivity of target vertex position (v_z) for charged tracks
796 to beam motion.

797 Next, ep-elastic events are skimmed (from all of the NH_3 target data-
798 set) using electron ID cuts for the electrons (see section 3.3) in the sixth
799 sector and proton ID consisting mainly of the time-of-flight cuts are used to
800 select protons in the third sector (opposite to the sixth one). Then missing
801 momentum cuts (less than 0.1 GeV for each of the four components P_x ,
802 P_y , P_z and E) based on 4-momentum conservation requirements (within
803 measurement uncertainties) are used to help further clean up the accidental

799
800
801
802
803
804
805
806
807
808
809
810
811
812
813
814
815
816
817
818
819
820
821
822
823
824
825
826
827
828
829
830
831
832
833
834
835
836
837
838
839
840
841
842
843
844
845
846
847
848
849
850
851
852
853
854
855
856
857
858
859
860
861
862
863
864
865
866
867
868
869
870
871
872
873
874
875
876
877
878
879
880
881
882
883
884
885
886
887
888
889
890
891
892
893
894
895
896
897
898
899
900
901
902
903
904
905
906
907
908
909
910
911
912
913
914
915
916
917
918
919
920
921
922
923
924
925
926
927
928
929
930
931
932
933
934
935
936
937
938
939
940
941
942
943
944
945
946
947
948
949
950
951
952
953
954
955
956
957
958
959
960
961
962
963
964
965
966
967
968
969
970
971
972
973
974
975
976
977
978
979
980
981
982
983
984
985
986
987
988
989
990
991
992
993
994
995
996
997
998
999
1000
1001
1002
1003
1004
1005
1006
1007
1008
1009
10010
10011
10012
10013
10014
10015
10016
10017
10018
10019
10020
10021
10022
10023
10024
10025
10026
10027
10028
10029
10030
10031
10032
10033
10034
10035
10036
10037
10038
10039
10040
10041
10042
10043
10044
10045
10046
10047
10048
10049
10050
10051
10052
10053
10054
10055
10056
10057
10058
10059
10060
10061
10062
10063
10064
10065
10066
10067
10068
10069
10070
10071
10072
10073
10074
10075
10076
10077
10078
10079
10080
10081
10082
10083
10084
10085
10086
10087
10088
10089
10090
10091
10092
10093
10094
10095
10096
10097
10098
10099
100100
100101
100102
100103
100104
100105
100106
100107
100108
100109
100110
100111
100112
100113
100114
100115
100116
100117
100118
100119
100120
100121
100122
100123
100124
100125
100126
100127
100128
100129
100130
100131
100132
100133
100134
100135
100136
100137
100138
100139
100140
100141
100142
100143
100144
100145
100146
100147
100148
100149
100150
100151
100152
100153
100154
100155
100156
100157
100158
100159
100160
100161
100162
100163
100164
100165
100166
100167
100168
100169
100170
100171
100172
100173
100174
100175
100176
100177
100178
100179
100180
100181
100182
100183
100184
100185
100186
100187
100188
100189
100190
100191
100192
100193
100194
100195
100196
100197
100198
100199
100200
100201
100202
100203
100204
100205
100206
100207
100208
100209
100210
100211
100212
100213
100214
100215
100216
100217
100218
100219
100220
100221
100222
100223
100224
100225
100226
100227
100228
100229
100230
100231
100232
100233
100234
100235
100236
100237
100238
100239
100240
100241
100242
100243
100244
100245
100246
100247
100248
100249
100250
100251
100252
100253
100254
100255
100256
100257
100258
100259
100260
100261
100262
100263
100264
100265
100266
100267
100268
100269
100270
100271
100272
100273
100274
100275
100276
100277
100278
100279
100280
100281
100282
100283
100284
100285
100286
100287
100288
100289
100290
100291
100292
100293
100294
100295
100296
100297
100298
100299
100300
100301
100302
100303
100304
100305
100306
100307
100308
100309
100310
100311
100312
100313
100314
100315
100316
100317
100318
100319
100320
100321
100322
100323
100324
100325
100326
100327
100328
100329
100330
100331
100332
100333
100334
100335
100336
100337
100338
100339
100340
100341
100342
100343
100344
100345
100346
100347
100348
100349
100350
100351
100352
100353
100354
100355
100356
100357
100358
100359
100360
100361
100362
100363
100364
100365
100366
100367
100368
100369
100370
100371
100372
100373
100374
100375
100376
100377
100378
100379
100380
100381
100382
100383
100384
100385
100386
100387
100388
100389
100390
100391
100392
100393
100394
100395
100396
100397
100398
100399
100400
100401
100402
100403
100404
100405
100406
100407
100408
100409
100410
100411
100412
100413
100414
100415
100416
100417
100418
100419
100420
100421
100422
100423
100424
100425
100426
100427
100428
100429
100430
100431
100432
100433
100434
100435
100436
100437
100438
100439
100440
100441
100442
100443
100444
100445
100446
100447
100448
100449
100450
100451
100452
100453
100454
100455
100456
100457
100458
100459
100460
100461
100462
100463
100464
100465
100466
100467
100468
100469
100470
100471
100472
100473
100474
100475
100476
100477
100478
100479
100480
100481
100482
100483
100484
100485
100486
100487
100488
100489
100490
100491
100492
100493
100494
100495
100496
100497
100498
100499
100500
100501
100502
100503
100504
100505
100506
100507
100508
100509
100510
100511
100512
100513
100514
100515
100516
100517
100518
100519
100520
100521
100522
100523
100524
100525
100526
100527
100528
100529
100530
100531
100532
100533
100534
100535
100536
100537
100538
100539
100540
100541
100542
100543
100544
100545
100546
100547
100548
100549
100550
100551
100552
100553
100554
100555
100556
100557
100558
100559
100560
100561
100562
100563
100564
100565
100566
100567
100568
100569
100570
100571
100572
100573
100574
100575
100576
100577
100578
100579
100580
100581
100582
100583
100584
100585
100586
100587
100588
100589
100590
100591
100592
100593
100594
100595
100596
100597
100598
100599
100600
100601
100602
100603
100604
100605
100606
100607
100608
100609
100610
100611
100612
100613
100614
100615
100616
100617
100618
100619
100620
100621
100622
100623
100624
100625
100626
100627
100628
100629
100630
100631
100632
100633
100634
100635
100636
100637
100638
100639
100640
100641
100642
100643
100644
100645
100646
100647
100648
100649
100650
100651
100652
100653
100654
100655
100656
100657
100658
100659
100660
100661
100662
100663
100664
100665
100666
100667
100668
100669
100670
100671
100672
100673
100674
100675
100676
100677
100678
100679
100680
100681
100682
100683
100684
100685
100686
100687
100688
100689
100690
100691
100692
100693
100694
100695
100696
100697
100698
100699
100700
100701
100702
100703
100704
100705
100706
100707
100708
100709
100710
100711
100712
100713
100714
100715
100716
100717
100718
100719
100720
100721
100722
100723
100724
100725
100726
100727
100728
100729
100730
100731
100732
100733
100734
100735
100736
100737
100738
100739
100740
100741
100742
100743
100744
100745
100746
100747
100748
100749
100750
100751
100752
100753
100754
100755
100756
100757
100758
100759
100760
100761
100762
100763
100764
100765
100766
100767
100768
100769
100770
100771
100772
100773
100774
100775
100776
100777
100778
100779
100780
100781
100782
100783
100784
100785
100786
100787
100788
100789
100790
100791
100792
100793
100794
100795
100796
100797
100798
100799
100800
100801
100802
100803
100804
100805
100806
100807
100808
100809
100810
100811
100812
100813
100814
100815
100816
100817
100818
100819
100820
100821
100822
100823
100824
100825
100826
100827
100828
100829
100830
100831
100832
100833
100834
100835
100836
100837
100838
100839
100840
100841
100842
100843
100844
100845
100846
100847
100848
100849
100850
100851
100852
100853
100854
100855
100856
100857
100858
100859
100860
100861
100862
100863
100864
100865
100866
100867
100868
100869
100870
100871
100872
100873
100874
100875
100876
100877
100878
100879
100880
100881
100882
100883
100884
100885
100886
100887
100888
100889
100890
100891
100892
100893
100894
100895
100896
100897
100898
100899
100900
100901
100902
100903
100904
100905
100906
100907
100908
100909
100910
100911
100912
100913
100914
100915
100916
100917
100918
100919
100920
100921
100922
100923
100924
100925
100926
100927
100928
100929
100930
100931
100932
100933
100934
100935
100936
100937
100938
100939
100940
100941
100942
100943
100944
100945
100946
100947
100948
100949
100950
100951
100952
100953
100954
100955
100956
100957
100958
100959
100960
100961
100962
100963
100964
100965
100966
100967
100968
100969
100970
100971
100972
100973
100974
100975
100976
100977
100978
100979
100980
100981
100982
100983
100984
100985
100986
100987
100988
100989
100990
100991
100992
100993
100994
100995
100996
100997
100998
100999
1001000
1001001
1001002
1001003
1001004
1001005
1001006
1001007
1001008
1001009
1001010
1001011
1001012
1001013
1001014
1001015
1001016
1001017
1001018
1001019
1001020
1001021
1001022
1001023
1001024
1001025
1001026
1001027
1001028
1001029
1001030
1001031
1001032
1001033
1001034
1001035
1001036
1001037
1001038
1001039
1001040
1001041
1001042
1001043
1001044
1001045
1001046
1001047
1001048
1001049
1001050
1001051
1001052
1001053
1001054
1001055
1001056
1001057
1001058
1001059
1001060
1001061
1001062
1001063
1001064
1001065
1001066
1001067
1001068
1001069
1001070
1001071
1001072
1001073
1001074
1001075
1001076
1001077
1001078
1001079
1001080
1001081
1001082
1001083
1001084
1001085
1001086
1001087
1001088
1001089
1001090
1001091
1001092
1001093
1001094
1001095
1001096
1001097
1001098
1001099
1001100
1001101
1001102
1001103
1001104
1001105
1001106
1001107
1001108
1001109
1001110
1001111
1001112
1001113
1001114
1001115
1001116
1001117
1001118
1001119
1001120
1001121
1001122
1001123
1001124
1001125
1001126
1001127
1001128
1001129
1001130
1001131
1001132
1001133
1001134
1001135
1001136
1001137
1001138
1001139
1001140
1001141
1001142
1001143
1001144
1001145
1001146
1001147
1001148
1001149
1001150
1001151
1001152
1001153
1001154
1001155
1001156
1001157
1001158
1001159
1001160
1001161
1001162
1001163
1001164
1001165
1001166
1001167
1001168
1001169
1001170
1001171
1001172
1001173
1001174
1001175
1001176

804 coincidences. These skimmed events are saved in root files and later reused
805 for the minimization process described here.

806 The cuts used in the initial data skimming required that each of the four
807 missing components be less than 0.1 GeV.

808 After that a correction routine involving a set of correction equations
809 with several unknown parameters are established. Then with the help of
810 TMinuit (ROOT version of Minuit), several sets of trial values are given to
811 these unknown parameters and the corresponding correction is applied to
812 the particles in the skimmed events. For each set of these trial values, a
813 specifically defined χ^2 (see below) is evaluated looping over all the skimmed
814 events and the Minuit tries to find the optimum set of these parameter values
815 for which the χ^2 is minimum. Such an optimal set of values are chosen as
816 the correct values of these parameters and is used in the eventual correction
817 routine.

818 **The correction routine**

819 The routine uses 17 constants (free parameters determined by the above
820 mentioned process of χ^2 -minimization) and the following input and output
821 variables:

- 822 • **Input variables:** x_r , y_r , $\text{cxd}\mathbf{c}$, $\text{cyd}\mathbf{c}$, xdc , ydc , zdc , p , q .

823 – x_r , y_r are x & y beam positions as returned by the raster correction
824 routine (see appendix)
825 – **cxd \mathbf{c}** , **cyd \mathbf{c}** are direction cosines of the track as measured at DC1
826 – **xdc**, **ydc**, **zdc** are the coordinates of the track measured at DC1
827 – p , q are the momentum and charge of the track

- 828 • **Output variables:** cxc , cyc , czc , vzc (all three corrected direction
829 cosines and the corrected Z-coordinate at the vertex) .

830 The sequence of calculation steps taken (inside the routine) to arrive at the
831 output results are as follows (where, I am also using the notations of P.
832 Bosted i.e., subscripts '0' used to indicate variables at vertex, subscript 'f'
833 for those at the drift chambers (these are the tl1_ variables in the ntuples),
834 and the values of (x, y, z) are in cm):

- 835 • First of all, get ready the following constants and variables:

- $f_c = \frac{B}{50} = 0.995$ is the overall field correction
 - * (i.e., the $B.dl$ correction factor. Our $B = 4.97T$, with B in kG f_c is 0.995)
 - $targsign = 1$
 - $\theta_f = \arccos(cz_{dc})$
 - $\phi_f = \text{atan2}(cy_{dc}, cx_{dc})$
- Then, θ_f is corrected (for the misalignment of the DC) as follows:
 - If it's the electron in the event,
 - * $\theta_f = \theta_f + (\text{par}[0] + \text{par}[1] \times \phi_f) \frac{\cos\theta_f}{\cos\phi_f} + (\text{par}[2] + \text{par}[3] \times \phi_f) \sin\theta_f$
 - else if its the proton,
 - * $\theta_f = \theta_f + (\text{par}[4] + \text{par}[5] \times \phi_f)$
- Next, get ϕ_0 without raster corrections yet
 - $\phi_0 = \phi_f + targsign \times f_c (0.186 + \text{par}[10] + (0.045 + \text{par}[11]) \theta^2 + (0.008 + \text{par}[12]) \theta_f^3 + (0.0032 + \text{par}[13]) \theta_f^3/p^2) \frac{q}{p}$
- Correction to polar angle from focusing effect. First, get focusing term for beam (x,y)=0.
 - $\delta\theta = f_c (0.90 \theta_f + 1.2 \theta_f^3)/(100 p^2)$
- Displacement of beam along trajectory (x_p) and perpendicular to it (y_p)
 - $x_p = x_r \cos\phi_0 + y_r \sin\phi_0$
 - $y_p = -(x_r + \text{par}[6]) \sin\phi_0 + (y_r + \text{par}[7]) \cos\phi_0$
- Correction to $\delta\theta$ from radial target field, which only depends on raster x and y but not vertex z. Also, no effect on peak at zero!
 - $\delta\theta = \delta\theta (1. + targsign q p (0.5/\theta_f) (y_p/0.75))$

862 • Now can get cz

863 – $\theta_0 = \theta_f + \delta\theta$

864 – $cz_c = \cos\theta_0$

865 • Now ϕ_0 again, this time including raster correction

866 – $\phi_0 = \phi_f + \text{targsign } f_c (0.186 + \text{par}[10] + (0.045 + \text{par}[11]) \theta^2 +$
867 $(0.008 + \text{par}[12]) \theta_f^3 + (0.0032 + \text{par}[13]) \theta_f^3/p^2) \frac{q}{p} (1 - (0.09 +$
868 $\text{par}[14]) \frac{0.35 - \text{par}[15]}{\theta_f} x_p)$

869 • Get cx and cy using this cz

870 – $cx_c = \sin\theta_0 \cos\phi_0$

871 – $cy_c = \sin\theta_0 \sin\phi_0$

872 • Renormalize czc

873 – $cz_c = \sqrt{1.0 - cx_c^2 - cy_c^2}$

874 • Apply target field rotation correction

875 – $cx_c = cx_c - \text{targsign } q \text{par}[8] cz_c/p$

876 – $cy_c = cy_c + \text{targsign } q \text{par}[9] cz_c/p$

877 • Renormalize again:

878 – $czc = \sqrt{1.0 - cx_c^2 - cy_c^2}$

879 – $\theta_0 = \arccos(cz_c)$

880 • Get vertex z in cm

881 – $r_{dc} = \sqrt{(x_{dc} - x_r)^2 + (y_{dc} - y_r)^2}$

882 – $Z_c = Z_{dc} - \frac{r_{dc} - (22 + \text{par}[16]) \cos\theta_0 (\tan\theta_0 - \tan\theta_f)}{\tan\theta_f}$

883 • Finally, the routine outputs (returns) the four corrected quantities

884 – cx_c, cy_c, cz_c, Z_c .

885 **Calculation of χ^2 (to be minimized)**

886 The chi-square has different components as follows:

$$887 \quad \chi^2 = \chi_{\text{Zvar}}^2(\mathbf{e}) + \chi_{\text{Zvar}}^2(\mathbf{p}) + \chi_{\text{Evar}}^2 + \chi_{\text{miss}}^2 + \chi_{\text{Ppen}}^2 + \chi_{\text{Epen}}^2 + \chi_{\text{Zpen}}^2 + \chi_{\Delta E}^2$$

888 where,

- 889 • $\chi_{\text{Zvar}}^2(\mathbf{e})$ and $\chi_{\text{Zvar}}^2(\mathbf{p})$ are Z-variance contributions from electron and
890 proton candidates in the ep-elastic events and are calculated as $\chi_{\text{Zvar}}^2 =$
891 $\frac{1}{N_{ep}-1} \left(\sum Z_c^2 - \frac{(\sum Z_c)^2}{N_{ep}} \right) / (0.05)^2$ separately for the electrons and protons.
892 (Here, Z_c is the corrected Z of vertex and N_{ep} is the number ep-elastic
893 events used in the minimization)
- 894 • $\chi_{\text{Evar}}^2 = \frac{1}{N_{ep}-1} \left(\sum E_b^2 - \frac{(\sum E_b)^2}{N_{ep}} \right) / (0.005)^2$ is E_b -variance contribution.
895 (Here, $E_b = M_p \left(\frac{1}{\tan(\theta_p)\tan(\theta_e/2)} - 1 \right)$ is the beam energy calculated after
896 the angles are corrected by the correction routine.)
- 897 • $\chi_{\text{miss}}^2 = 100 \times \left(\frac{\sum p_x^2(\text{miss}) + \sum p_y^2(\text{miss})}{0.02^2} + \frac{\sum p_z^2(\text{miss}) + \sum E^2(\text{miss})}{0.05^2} \right)$ is missing
898 four-momentum contribution. (Here, 100 is an arbitrary number to
899 make the weight of this contribution comparable to others.)
- 900 • $\chi_{\text{Ppen}}^2 = \sum_{i=0}^{16} \frac{(par[i] - iPar[i])^2}{0.01^2}$ is the contribution due to runaway penalty
901 on free parameters of the minimization. (Here, par[i] & iPar[i] are the
902 current and initial values of the 'i'th parameter. In the first iteration,
903 initial values were set to either zeros or the corresponding values as
904 determined for EG1-DVCS by P. Bosted. In later iterations, they were
905 set to the values determined from the previous iteration of the mini-
906 mization.)
- 907 • $\chi_{\text{Zpen}}^2 = \sum_{e,p} \left(\sum_{N_{ep}} \frac{(Z_c - (-100.93))^2}{0.05^2} \right)$ is a penalty term when Z_c runs away
908 from the known/nominal target center (-100.93 cm)
- 909 • $\chi_{\text{Epen}}^2 = \sum_{i=2}^4 \left(\frac{\sum_{N_{ep}} E_b}{N_{ep}} - E_0 \right)^2 / (0.005)^2$ is a penalty term to constrain E_b
910 running away from the nominal values E_0 of beam energy.

- 911 • $\chi^2_{\Delta E} = \left(\sum_{i=2}^4 \frac{\sum N_{ep}}{N_{ep}} (E_b - E_0)^2 \right) / (0.005)^2$ is another penalty term to constrain
 912 E_b running away from the nominal values E_0 of beam energy.

913 **Minimization**

914 TMinuit is used to minimize the value of χ^2 as calculated above and, thereby,
 915 determine the values of the free parameters used in the correction routine.
 916 The minimization was done in such a way that the parameters were deter-
 917 mined step by step - first deciding the first six parameters (keeping others
 918 fixed to initial values), then next two, then next two, then next four, then
 919 next 2 and finally the last one respectively.

920 **Tracking Correction Results**

921 With the method of χ^2 -minimization described above, the following set of
 922 values were determined for the 17 parameters from par[0] through par[16]
 923 respectively:
 924 -0.00165789, -0.00131314, -0.00643021, -0.00721441, -0.00775272, 0.00483673,
 925 0.063387, -0.0615822, 0.00133127, 0.000839944, 0.0210091, -0.0363265, 0.00335536,
 926 0.00104193, 2.51519, -0.0313527, -1.29325

927 As a result of the corrections with these newly determined parameter
 928 values, various quantities before and after the corrections looked as shown in
 929 the following figure:

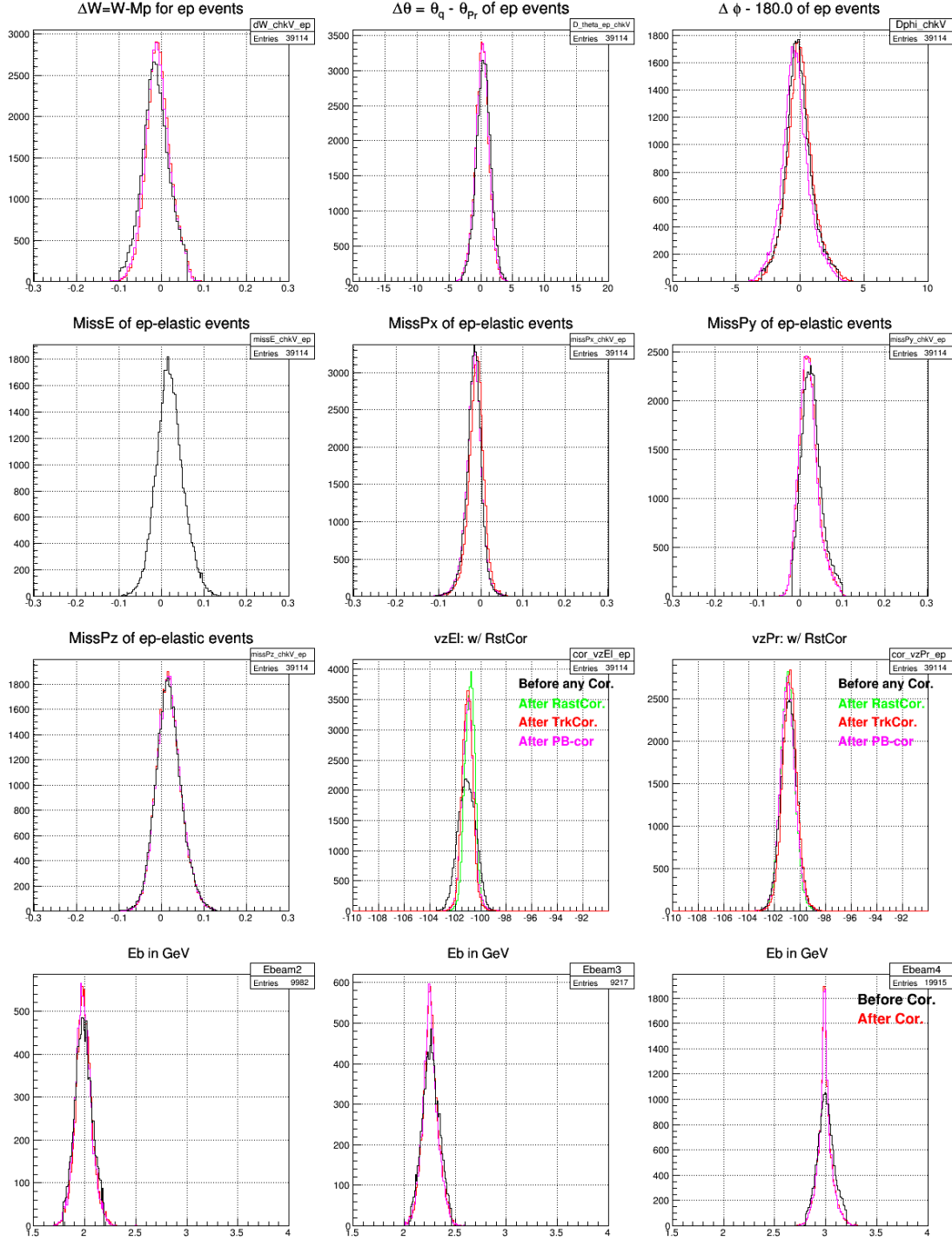


Figure 3.25: Comparing various quantities before and after the tracking corrections which affects only the angles (and ~~not~~ the magnitude 'p') of the momentum.

930 **3.5.3 Momentum Correction**

931 Different DC related factors contribute to the biggest part of the system-
 932 atic deviations of particle momenta as reconstructed by RECSIS. The drift
 933 chambers could be misaligned relative to their nominal positions or the sur-
 934vey results that is used by RECSIS could be inaccurate or out-of-date. The
 935 effects of physical deformations (due to thermal and stress distortions) of the
 936 chamber including wire-sag, incorrect wire positions may not have been incor-
 937 porated properly. The torus field map used by the reconstruction software
 938 may not have been accurate and complete enough [32]. Effects on angles
 939 θ and ϕ due to these contributions are already factored in the tracking cor-
 940 rection described earlier. However, a separate method is developed to correct
 941 for the effect on the magnitude p of the momentum. This p -correction meth-
 942 ods picks up and builds on some of the ideas outlined in the CLAS-NOTE
 943 2003-005 [32].

944 **Procedure to determine the first 11 parameters**

945 The procedure involved dividing the covered kinematic space into a number
 946 of bins, finding in them the magnitude of shifts of the inclusive elastic peaks
 947 w.r.t. the expected position and use that to fit to a function to get an
 948 analytical expression for the correction. The following angular bins were
 949 used:

- 950 • Six θ_{dc1} bins: (0,8),(8,10),(10,12),(12,15),(15,20),(20,30) degrees
- 951 • Five ϕ_{dc1} bins: (-10,-6),(-6,-2), (-2,2), (2,6), (6,10) degrees

952 where the angles used are the ones measured at the first drift chamber and
 953 ϕ_{dc1} is measured w.r.t the sector mid-plane (thus the maximum range allowed
 954 is (-30.0,30.0)).

$$E'_{elastic} = \frac{E_{beam}}{1 + \frac{2E_{beam}}{M_p} \sin^2(\theta_e/2)} \quad (3.4)$$

955 In each of these kinematic bins, the quantity $\Delta E = E'_{elastic} - p$ (see Eq.
 956 3.4) is histogrammed for both NH₃ and ¹²C data separately. Next, the carbon
 957 histogram is cross-normalized with the ammonia histogram (by comparing
 958 the two in the region left to the quasi-elastic peak) and subtracted from the

959 latter one to remove the nuclear background. The difference gives histograms
 960 for the elastic events (as shown by the dashed green histogram in Fig. 3.26).
 961 A Gaussian fit to the extracted elastic histogram gives the position and width
 962 of the distribution. The offset or shift of average position of the peak with
 963 respect to the expected $\Delta E = 0$ gives us the needed correction on energy
 964 $E \approx p$ for the electron. This process is repeated for all of the bins listed
 965 above and the corresponding ΔE offsets or the corrections are determined
 966 for each of them. Additionally, ΔE distributions using ^{15}N nuclear mass
 967 in calculating $E'_{elastic}$ are also made and off-sets in the corresponding elastic
 968 peaks are also recorded whenever possible (particularly from the lower θ bins
 969 from low beam energy data where the nuclear-elastic and quasi-elastic peaks
 970 are well separated). Finally, these values of corrections for different average
 971 values of θ_{dc1} and ϕ_{dc1} are fit to Eq. 3.5 (which is based on similar work done
 972 for EG1b analysis[22]) and using the method of χ^2 -minimization in order to
 973 determine the values of the 11 fit parameters.

$$\frac{\Delta p}{p} = Pcorr1 + Pcorr2 + PatchCorr \quad (3.5)$$

974 where, $\frac{\Delta p}{p}$ is the ratio of the correction (Δp) to the magnitude (p) of the
 975 momentum and

$$Pcorr1 = \left((E + F\phi) \frac{\cos\theta}{\sin\phi} + (G + H\phi) \sin\theta \right) \frac{p}{qB_{torus}} \quad (3.6)$$

$$Pcorr2 = (J\cos\theta + K\sin\theta) + (M\cos\theta + N\sin\theta)\phi \quad (3.7)$$

$$PatchCorr = 0.02 \left(P + (Q + R \frac{\phi_{deg}}{30^\circ}) (\frac{10^\circ}{\theta_{deg}})^3 \right) \quad (3.8)$$

976 The quantity B_{tor} stands for $\int B_\perp dl$ along the track length multiplied by
 977 the speed of light in the units of m/ns ($c = 0.29979$ m/ns) and is given by

$$B_{tor} = 0.76 \frac{I_{tor} \sin^2(4\theta)}{3375\theta/rad} \quad \text{for } \theta < \frac{\pi}{8} \quad (3.9)$$

$$B_{tor} = 0.76 \frac{I_{tor}}{3375\theta/rad} \quad \text{for } \theta > \frac{\pi}{8} \quad (3.10)$$

978 In all these equations, sector number, θ , ϕ , θ_{deg} , and ϕ_{deg} come from the
 979 angle information measured at DC1. The direction cosine variables tl1_cx,
 980 tl1_cy, tl1_cz (from pass1 ntuple) are used to derive these quantities. C++
 981 standard functions `acos()` and `atan2()` are used to evaluate θ , ϕ (w.r.t the
 982 sector mid plane).

983 These total of eleven unknown parameters were determined by fitting
 984 above mentioned momentum offsets (in combination with ionization energy
 985 loss correction for electrons (see Sec.3.5.4 below)) to the correction function
 986 given by the Eq. 3.5.

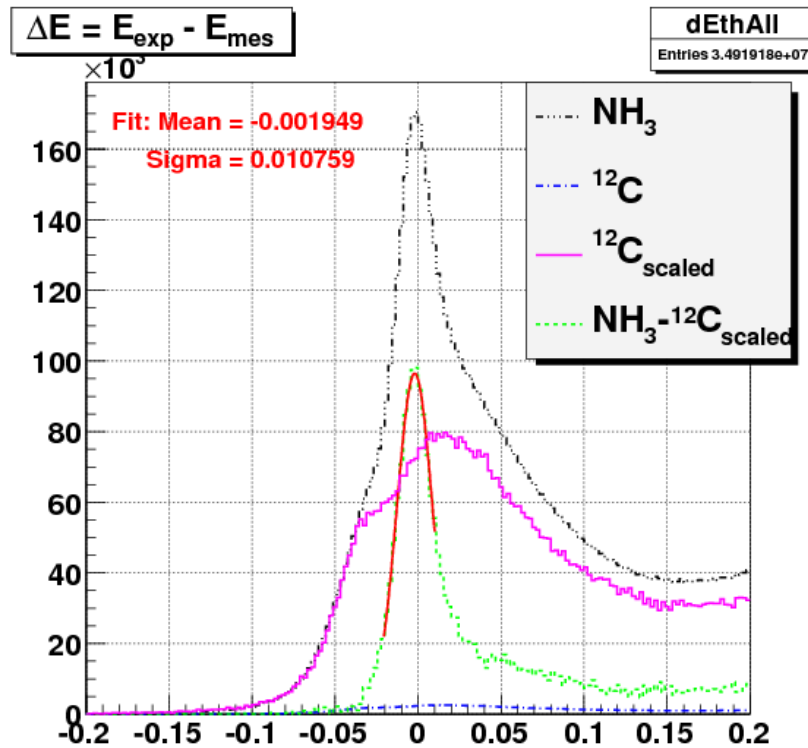


Figure 3.26: Plots showing background removal from the ΔE counts from NH_3 (shown by “ NH_3 ” line) data (by subtracting cross-normalized counts from ${}^{12}\text{C}$ data (shown by “ ${}^{12}\text{C}_{\text{scaled}}$ ” line)) to separate the elastic peak (shown by “ $\text{NH}_3 - {}^{12}\text{C}_{\text{scaled}}$ ” line) in one of the kinematic bins, thereby getting the momentum offset for that bin.

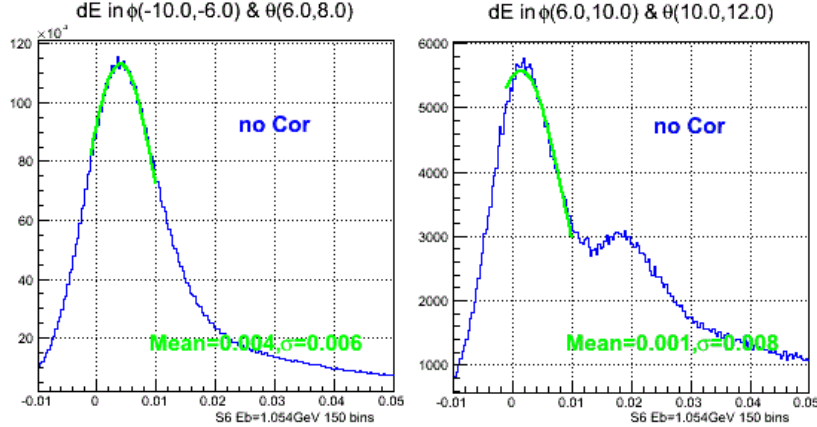


Figure 3.27: Nuclear elastic peaks from ^{15}N target and the Gaussian fits in two of many kinematic bins as seen in $\Delta E = E'_{\text{elastic}} - p$ distributions from NH₃ data before the momentum corrections. In this case E'_{elastic} is evaluated using known mass of ^{15}N in Eq. 3.4. In the second plot, the proton elastic peak is also visible. Ideally, after all the corrections, the nuclear elastic peak is expected to be centered at zero. But, as is obvious from these figures, these peaks show offsets. These offsets (given by the mean values of the Gaussian fits) are collected from those bins in which the nuclear elastic peaks are very well separated (particularly the first few angular bins) and used in the χ^2 -minimization along with all the offsets of elastic peaks (see Fig. 3.26)

3.5.4 Outgoing Ionization Loss Correction

In addition to the corrections described above, the energy (E) of each of the particles is corrected for the outgoing ionization loss by adding an estimation of ionization loss as follows: $E_{\text{cor}} = E + \Delta E$ with $\Delta E = \frac{dE}{dX}\tau$ where the factor τ is the total effective mass thickness traversed by the particle and

$$\frac{dE}{dX} \approx 2.8 \text{ MeV}/(\text{g cm}^{-2}) \quad \text{for electrons} \quad (3.11a)$$

and, for hadrons [33]

$$\frac{dE}{dX} \approx 0.307 \times \frac{0.5}{\beta^2} \left(\ln \left(2.0 \times 511.0 \frac{\beta^2 \gamma^2}{0.090} \right) - \beta^2 \right) \text{ MeV} \quad (3.11b)$$

which is an approximation of the Bethe-Block formula [33]:

$$-\frac{1}{\rho} \frac{dE}{dx} = 4\pi N_a r_e^2 m_e c^2 \frac{Z}{A} \frac{1}{\beta^2} \left(\ln \left(\frac{2m_e c^2 \gamma^2 \beta^2}{I} \right) - \beta^2 \right) \quad (3.12)$$

994 This quantity is calculated as follows:

995 • $\tau = \tau_{||}/\cos\theta$ if $\theta \leq \pi/4$

996 • $\tau = \tau_{||}/\cos(\pi/4)$ if $\theta > \pi/4$

997 where $\tau_{||}$ is calculated as:

998 • $\tau_{||} = \Delta z \times 0.6 + 0.4$ if $\Delta z > 0.0$ and $\Delta z < 1.0$

999 • $\tau_{||} = 0.6 + 0.4$ if $\Delta z \geq 1.0$

1000 • $\tau_{||} = 0.4$ if $\Delta z \leq 0.0$

1001 with $\Delta z = z_{target_center} - z_{ave} + L_{target}/2 = (-101.0 \text{ cm} - z_{ave} + 0.5) \text{ cm}$ being
1002 the physical distance (along the target length) traveled by the particle
1003 through the polarized target material (e.g. the EG4 ND₃ target has length
1004 1.0 cm and is positioned at $z = -101.0 \text{ cm}$). The factor 0.6 is the effective
1005 mass thickness of ND₃ (density of ND₃ ($\sim 1 \text{ g/cm}^3$) multiplied by the pack-
1006 ing fraction which is roughly 0.6 [34], whereas 0.4 is the sum of the mass
1007 thicknesses of He (~ 0.3) and that of window foils (~ 0.1) [22].

1008 Using the ionization loss corrected energy and the rest mass of the parti-
1009 cle, momentum is recalculated as $p_{cor} = \sqrt{E_{cor}^2 - m^2}$ (where m is the mass
1010 of the particle). Finally, this new p is used along with the previously cor-
1011 rected angles to evaluate the three cartesian components p_x , p_y and p_z of the
1012 momentum.

1013

1014 **3.6 Cerenkov Counter (CC) Efficiency**

1015 In the EG4 experiment, the Cherenkov Counter (CC) signal plays a major
1016 part in forming the event trigger for the data-acquisition system (DAQ). As
1017 stated earlier (see 2), for the purpose of achieving low Q^2 measurements with
1018 high detector efficiency⁵, a new dedicated CC was designed and placed in the
1019 sixth sector. Even though the new CC was designed to have a very high and
1020 uniform detection efficiency, some variation occurs over the covered kinematic
1021 range and therefore the knowledge of the detector efficiency as a function of
1022 the kinematics is required by our “method of absolute cross-section differ-
1023 ence”. Therefore, a study was done to determine the CC efficiency as follows.

5High detection efficiency is crucial for achieving smaller systematic uncertainties in the extracted physics quantities.

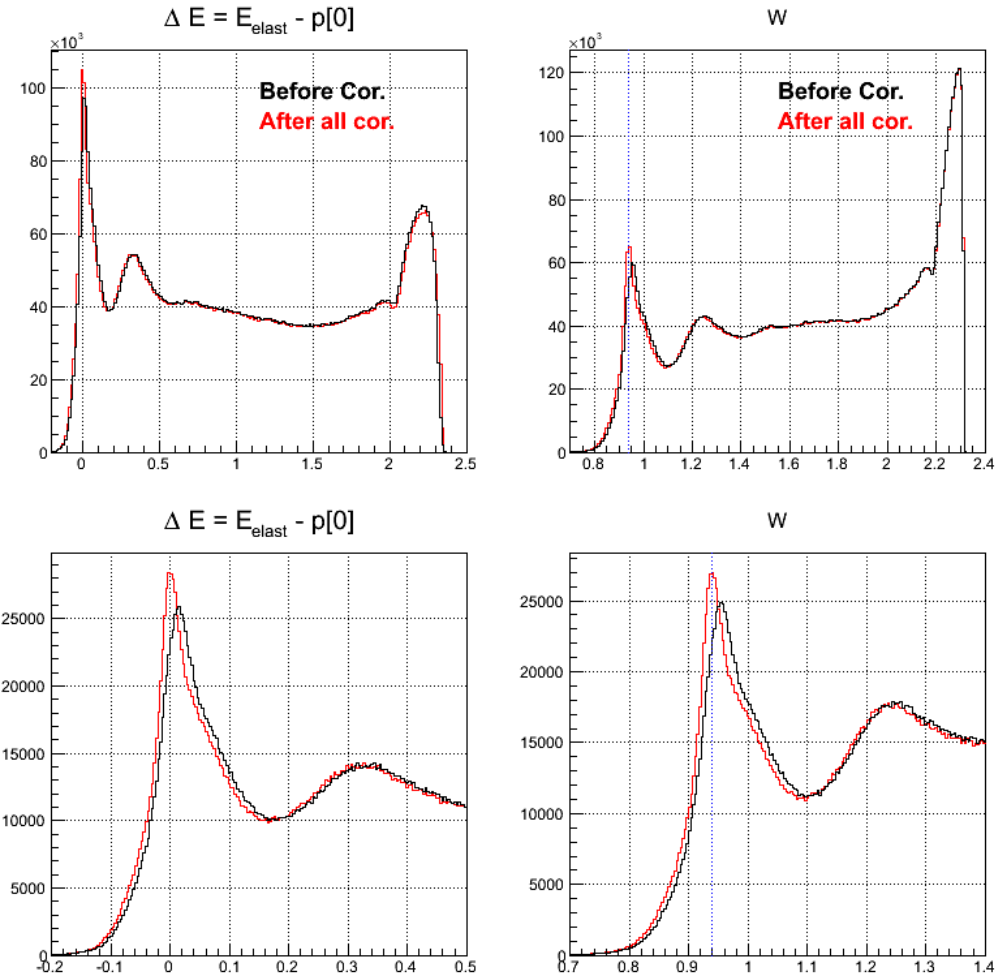


Figure 3.28: Effects of kinematic corrections on inclusive events from 3 GeV NH₃ data. Here, distributions of ΔE and W are shown in two different ranges. The upper ones show the full range distributions, whereas the lower two show the distributions near the quasi-elastic peak. The distributions before the corrections are shown by **black continuous** lines and the ones after the corrections are shown by the **redlines**. Here, E_{elast} is the calculated or expected energy of the scattered electron assuming it was scattered off elastically, whereas, $p[0]$ is the momentum as measured by CLAS.

1024 **3.6.1 Procedure**

1025 It is assumed that the efficiency for some specific kinematic bin depends
 1026 on the average number of photoelectrons produced by electrons in that bin
 1027 which, in turn, is determined by the hit location on the Cerenkov PMT-
 1028 projected plane as well as the angle with which the electron hits (or intersects)
 1029 the plane. In the following, we describe how we determined the efficiency as
 1030 a function of kinematic variables.

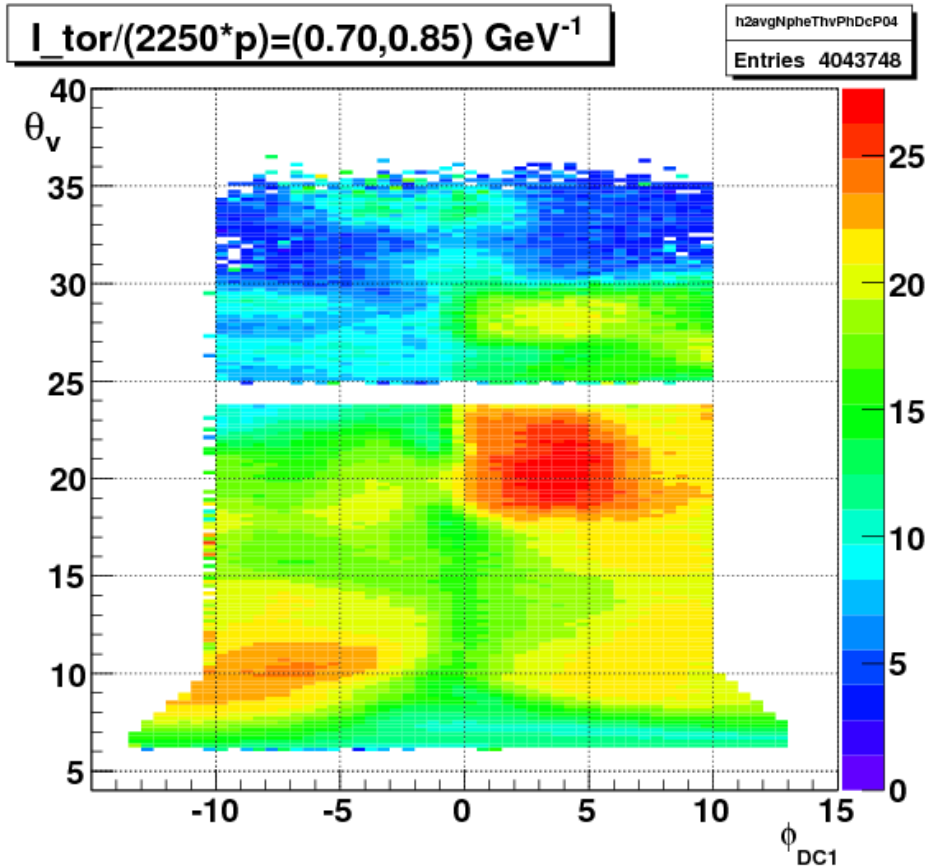


Figure 3.29: Average photoelectron number (color-coded) produced in the 6th sector CC as a function of θ_{vtx} and ϕ_{DC1} in the second bin of the variable $ip = (I_{tor}/2250)/p$ (from the 2.3 GeV NH₃ data).

- 1031 1. First, we define a torus-current normalized inverse-momentum variable
 1032 $ip = (I_{tor}/2250)/p$ (see above), and divide the whole kinematic space

1033 into 12 bins in “ip” as follows: (0.3, 0.4, 0.5, 0.6, 0.7, 0.85, 1.0, 1.25,
1034 1.5, 1.75, 2.0, 2.25, 2.53). (For example, a 0.5 GeV electron during a
1035 2 GeV run, which used 2250 A for torus current, would have $ip = 2.0$
1036 GeV^{-1})

- 1037 2. Next, for each bin in “ip”, a 2D map of the average number of photoelec-
1038 trons is produced in a kinematic space defined by θ_{vtx} (scattering angle
1039 measured at the event vertex) and ϕ_{DC1} (azimuthal angle as measured
1040 at DC1). For this step, some data from NH₃ production runs⁶ are used
1041 with the standard electron selection cuts. One of these average-nphe
1042 maps is shown in the Fig. 3.29.
- 1043 3. Next, using the “EC-only-trigger” data runs, good electron candidates
1044 are selected using the same cuts as before but without any CC-related
1045 cuts. For each of the selected electrons, the expected number of photo-
1046 electrons in the CC is determined in a look-up from the above average
1047 N_{ph} -maps based on its momentum and angles. This expected N_{ph} is
1048 then histogrammed in two ways - one histogram for those electrons
1049 which either didn’t trigger CC or didn’t pass all of the CC related
1050 cuts and another histogram for all electrons. The ratio of these two
1051 histograms (shown in the top-right and top-left panels of Fig. 3.30 re-
1052 spectively) gives us the inefficiency of the CC-detector as a function of
1053 N_{ph} (as shown by the bottom two panels of the same figure). (Errors
1054 in the inefficiencies have not been drawn (for the purpose of cleaning)
1055 in the figures but they were calculated using the fact that the error in
1056 a ratio N2/N1 is $\sqrt{N2(1 - N2/N1)/N1}$).
- 1057 4. The ideally expected CC intrinsic inefficiency is given by the Poisson
1058 distribution, since we require more than 2 photoelectrons, the theoreti-
1059 cal prediction for the inefficiency is actually $(1 + N_{ph} + 1/2 N_{ph}^2) * \exp(-N_{ph})$. However,
1060 we found empirically that if we calculate N_{ph} only with
1061 electrons that exceed the threshold of 2.5, then we find that the func-
1062 tional form is pretty close to the form $y = p_0 + p_1 \cdot \exp(-p_2 x)$, where
1063 x represents $\langle N_{ph} \rangle$, and y represents the inefficiency. This form was

⁶This method relies on the use of two different sets of data. One is the regular NH₃ target data and another is the “EC-only” data runs which were collected without using CC in the trigger. Since the latter type of data were collected with NH₃ as target, to be consistent, NH₃ production data was chosen rather than the ND₃ ones to make the N_{ph} -maps.

1064 used to fit with the above measured inefficiency and the result of the
1065 fit is shown in Fig. 3.30. We find that the inefficiency agrees very well
1066 with the expectation at low nphe, but remains at a very small constant
1067 value of around 0.01 (we call it the “constant background”) at higher
1068 nphe.

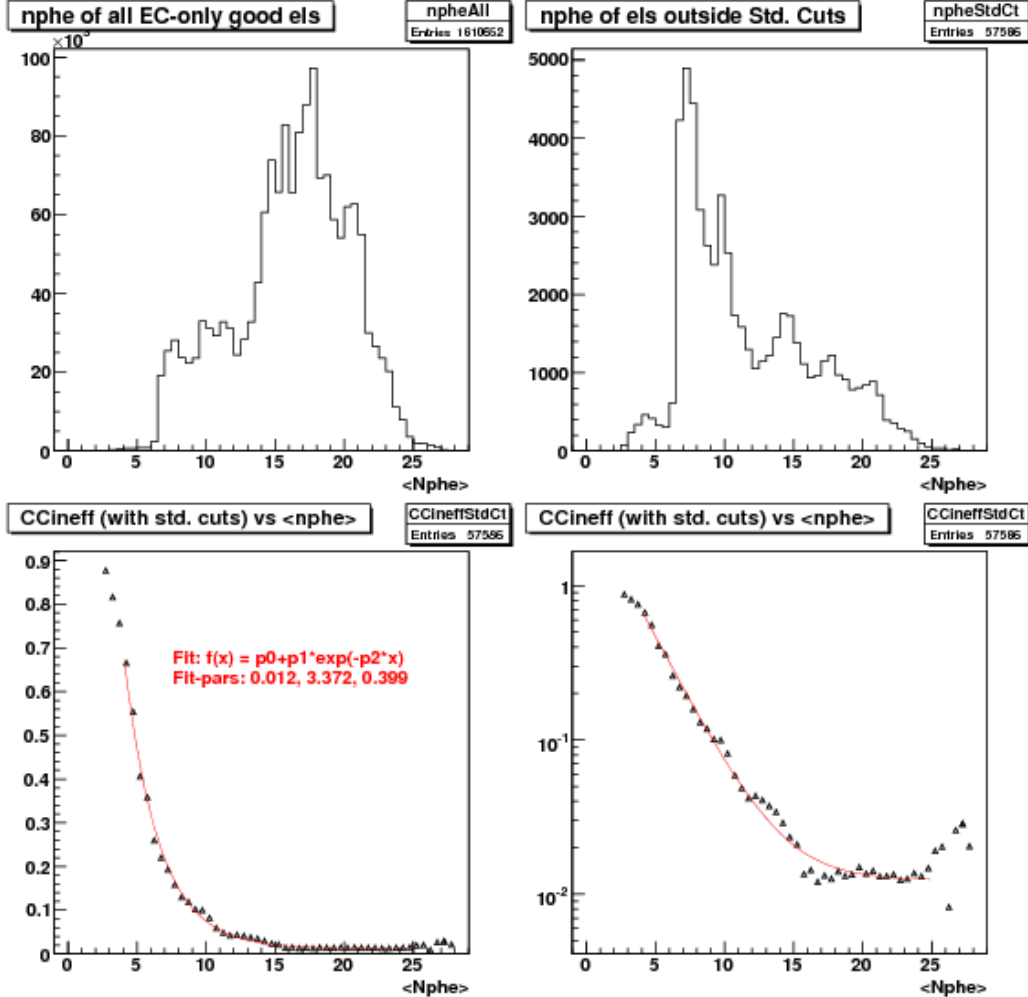


Figure 3.30: EC detected good electrons (for all momenta) as a function of $\langle N_{ph} \rangle$ (top left). Similar distribution (top right) for those good electrons that were detected by the EC but were rejected by the standard set of event selection cuts which includes CC-dependent cuts. By dividing the latter with the former, one gets the calculated CC inefficiency. The bottom two plots show the inefficiency distribution and a fit (red continuous line) in both linear (in third panel) and logarithmic (fourth panel) scales. Looking at the first plot, it can be seen that most electrons are above $N_{ph} = 15$ where the inefficiency is at most 1-2 %.

- 1069 5. Finally we use the inefficiency fit just developed to evaluate the corre-
 1070 sponding efficiencies and transform the 2D map of N_{ph} into the corre-

1071 sponding efficiency maps (see Fig. 3.31 for such a map in one momen-
 1072 tum bin.). These maps are later used to apply the efficiency correction
 1073 on an event by event basis in the simulation.

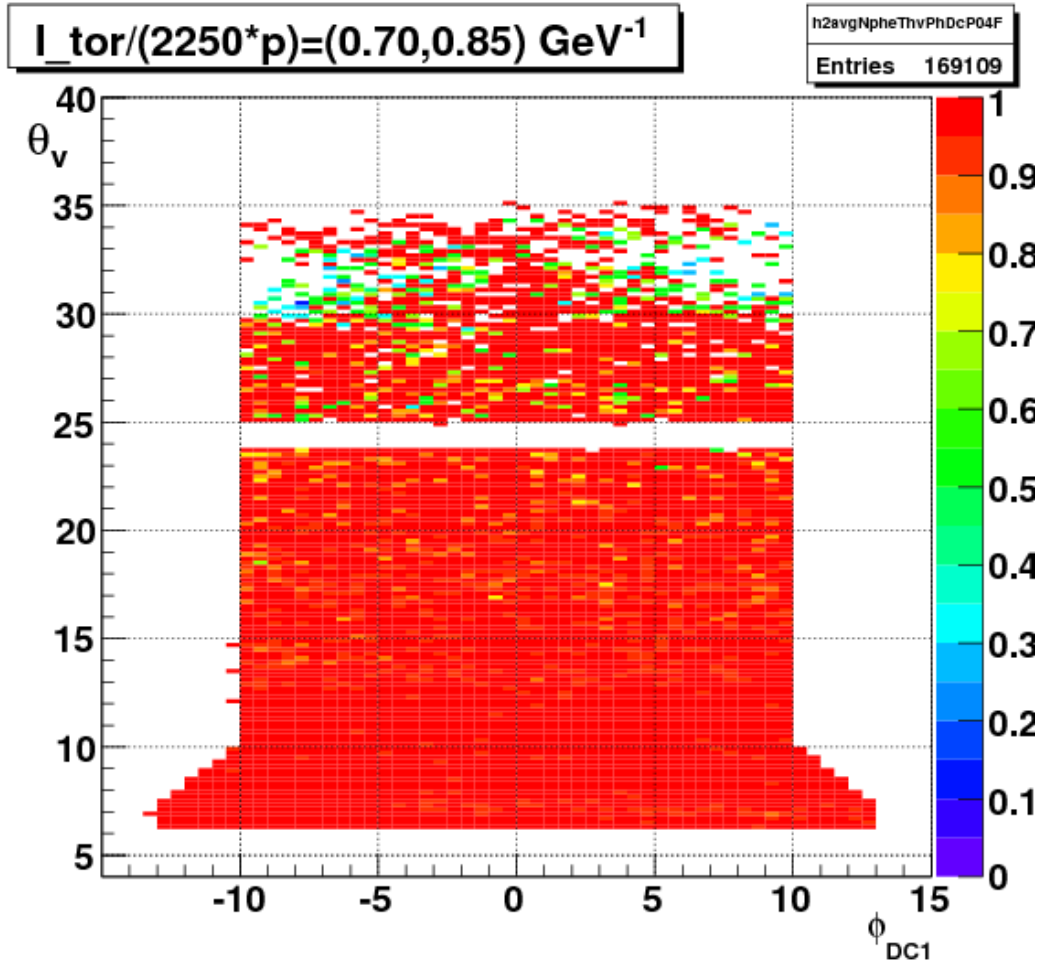


Figure 3.31: CC-efficiency in a momentum bin .

1074 From this study, we see that the CC is very efficient in most of the
 1075 kinematic region (see Fig. 3.31). Once, the CC-(in)efficiency was estimated,
 1076 we use the calculated CC efficiency to multiply our simulation (i.e., for each
 1077 simulated event, we look up the CC efficiency and weigh the event with it).

1078 3.7 Pion Contamination Corrections

1079 One of the two major sources of backgrounds in the measured EG4 electron
1080 rates comes from misidentified negatively charged pions (π^-) that produce
1081 similar set of signals as electrons in various detector components and thus
1082 pass the electron ID cuts. In the EG4 experiment, signals from the elec-
1083 tromagnetic calorimeter (EC) and Cherenkov counter (CC) are used to dis-
1084 criminate electrons from pions, but even with stringent conditions on these
1085 signals, some of the pions get misidentified as electrons. To avoid limiting
1086 statistics too much in order to minimize the final statistical error in a given
1087 kinematic bin, a trade-off in purity versus efficiency (statistics) is made by
1088 quantifying the amount of this kind of contamination.

1089 3.7.1 Method

1090 First, the whole kinematic space covered by EG4 is divided into 90 two-
1091 dimensional bins - 9 in p and 10 in θ ⁷.

1092 For each kinematic bin, a histogram of the number of photo-electrons
1093 (variable ' N_{phe} ' in the data ntuple) produced by the electron candidates (se-
1094 lected using the standard particle selection conditions (cuts) except that no
1095 cut on ' N_{phe} ' is included is made (see Fig. ??). Likewise, using a very strin-
1096 gent set of cuts, a similar histogram is made for the cleanest possible sample
1097 of pion candidates in the same kinematic bin.

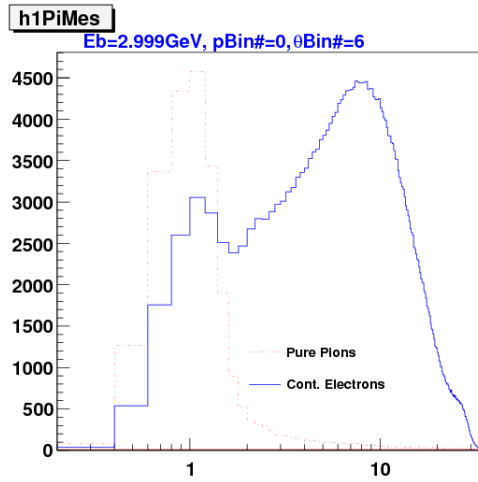
- 1098 • **Estimating the contamination in each bin:** A 7th order polyno-
1099 mial is fit to the N_{phe} histogram for electrons in the N_{phe} range extend-
1100 ing from $N_{phe} = 1.8$ to $N_{phe}=10$. The fit is then extrapolated down
1101 to $N_{phe} = 0$ (see Fig. ??). Subtracting the extrapolated fit from the
1102 impure electron distribution results in the extraction of the contami-
1103 nating pion peak⁸. Rescaling the pure pion sample to the extracted

⁷For 2 GeV or higher beam energy data sets, the p -bin boundaries are chosen as (0.30, 0.60, 0.90, 1.20, 1.50, 1.80, 2.20, 2.60, 3.00) and (0.30, 0.45, 0.60, 0.75, 0.9, 1.1, 1.4) for others. And, for θ , the boundaries are (5.0, 6.0, 7.0, 8.0, 9.0, 10.0, 12.0, 15.0, 19.0, 25, 49). The choice of the binning was rather arbitrary. Nevertheless higher statistics region was divided into relatively finer bins (event population peaks around $\theta= 10$ degrees).

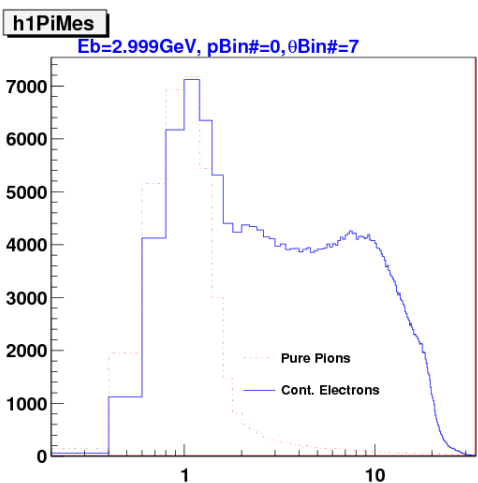
⁸Beyond $N_{phe} = 1.8$, the electron sample is nearly pure except for a tiny fraction due to the pion tail, so any function that fits that section of the N_{phe} -distribution is supposed to represent the pure electron distribution. In order to simplify the situation, we chose to fit only from 1.8 to 7.0 rather than covering the full range beyond 7.0.

peak gives us the distribution of the actual pion contamination over the complete range of N_{phe} . Finally, the counts corresponding to this rescaled pure sample in the region above the standard cut $N_{phe} > 2.5$ is calculated. Then the ratio of this count to the impure electron count in the same standard N_{phe} range gives the measured contamination for the bin.

- The contaminations thus evaluated for different momentum bins belonging to a particular θ -bin are then plotted against the corresponding momenta. Then, this is fit to an exponential function.
- The parameters par1 and par2 of the exponential fit performed in different theta bins are next graphed together to see the presumed linear dependence.
- Finally, a global fit is performed on all the contaminations in different θ - and p- bins (not on the fit parameters). The fit parameters from the earlier two fits only give us a hint to the type of the dependence, thus allowing us decide the form of the fit function.



(a) For the first in momentum and seventh in θ bin.



(b) For the first in momentum and eighth in θ bin.

Figure 3.32: Number of photo-electrons produced in CC by clean pion and contaminated electron samples (3.0 GeV data)

₁₁₂₀ From the study, it is found that the typically pion contamination is less
₁₁₂₁ than 1 %.

3.8 e^+e^- -Pair Symmetric Contamination Corrections

The next major source of background is the secondary electrons from various e^+e^- pair production processes. When an electron originating from such a pair passes through the detector, the detector has no way to distinguish it from the electrons that actually scattered off the target. Therefore, the detector simply accepts it as a true scattered electron candidate, thus producing a contamination that has to be estimated and corrected for. The first such source is the wide-angle e^+e^- pair production from bremsstrahlung photons generated in the target. The other major source is hadron decay such as the Dalitz decay ($\pi^0 \rightarrow e^+e^-\gamma$), $\pi^0 \rightarrow \gamma\gamma$ and then conversion of these photons into e^+e^- pairs. Likewise, the pseudoscalar particle η , and the vector mesons ρ , ω , ϕ also decay to e^+e^- , but they are not major contributors because of their very small decay probabilities as well as the small population compared to the π^0 and photons. Of all these sources, the biggest contributor to the secondary electrons is the $\pi^0 \rightarrow \gamma\gamma$ with γ conversion to e^+e^- [35].

The amount of contamination from this type of process can be estimated by monitoring the amount of positrons that were recorded under the same experimental and kinematic conditions. Because of the symmetry in the amount of electrons and positrons produced from these sources, the positron to electron ratio gives us the amount of the pair-symmetric contamination. However, due to the presence of the strong magnetic field inside the detector and the fact that the positrons have opposite charges, their detector acceptance would be different in a given setting. By reversing the magnetic field while keeping everything else the same, it is possible to estimate the contamination. For some of the beam energies used for the NH₃ data of the EG4 experiment, some data were collected with identical experimental setting but with the torus field reversed. The data from those runs were used to estimate the amount of positrons in somewhat the same fashion as pion contamination. For example, Fig. 3.34 shows one estimate (both data points and the fit) of the contamination in EG4 compared with those determined for the EG1b experiment [22].

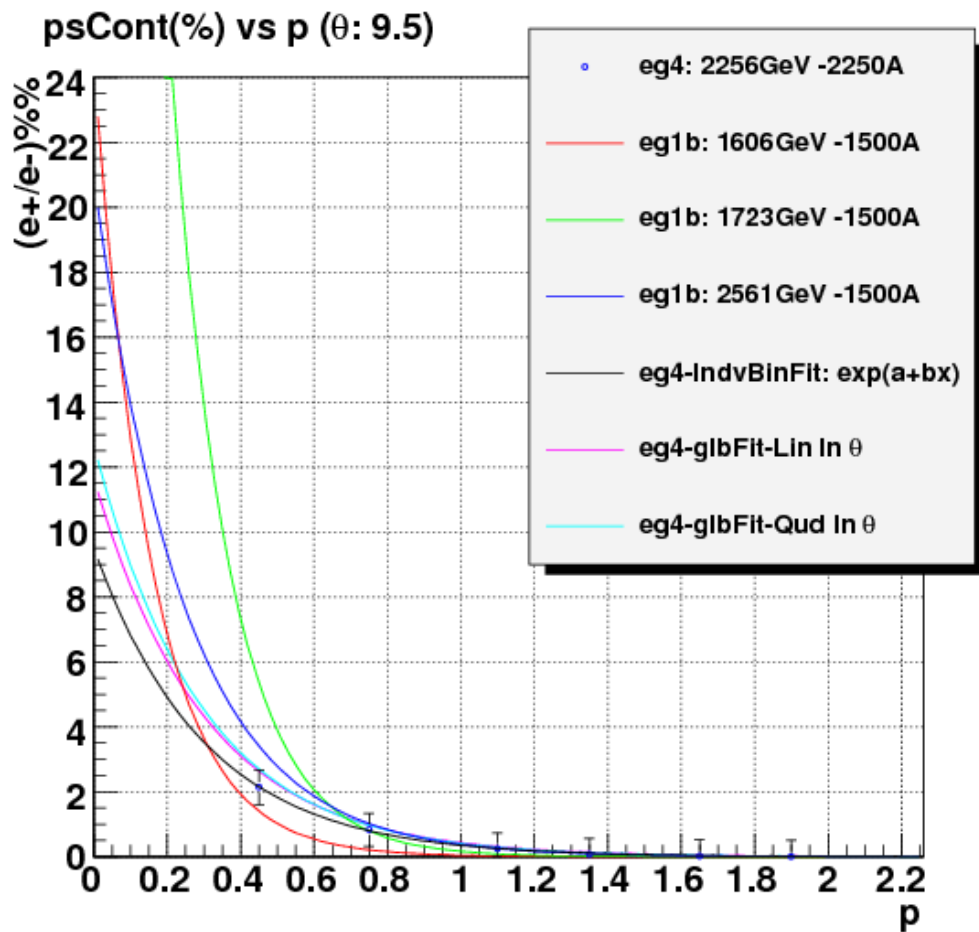


Figure 3.34: Pair-symmetric contamination Fits (%) as a function of electron momentum.

1154 For this analysis, both the pion and e^+e^- pair symmetric contaminations
 1155 are small enough to be ignored. This leads to only a slight increase in the
 1156 systematic error in the final physics results.

1157 **3.9 Study of NH₃ Contamination of EG4 ND₃**
1158 **Target**

1159 In equation (3.1), it is assumed that the ammonia target is 100% pure i.e.
1160 composed of only ¹⁵ND₃ molecules and that the contribution from the
1161 slightly polarized nitrogen is negligible. But, in practice, the standard ND₃
1162 sample is not a 100% pure material. Rather, it contains one or two percent
1163 of ¹⁴ND₃, ¹⁵NH₃ [36], and some traces of other isotopic species of ammonia.
1164 It was reported by the EG1-DVCS experiment at Jlab [37][38] that a higher
1165 than usual amount of NH₃ (about 10%) was observed in the ND₃ target,
1166 indicating that an inadvertent mix-up of NH₃ and ND₃ materials could have
1167 happened during the experimental run. Wondering if the EG4 experiment
1168 had a similar incident, we decided to investigate and estimate the amount of
1169 NH₃ contamination of our ND₃ target by looking at the data from the ND₃
1170 run period of the experiment as described below.

1171 **3.9.1 Procedure**

1172 The method involves using ep elastic (or quasi-elastic in the case of non-
1173 proton target) events and comparing the width in some quantity that reflects
1174 the correlation between the scattered electron (e) and the recoiling proton (p)
1175 due to the kinematic constraints of such events. The most suitable correlation
1176 is the one between the polar angles of the electron and the proton. That is
1177 because of the better angular resolution in CLAS than that for momentum,
1178 and also due to the fact that polar angle (θ) resolution is much better than
1179 that of the azimuthal angle (ϕ) because of the rotational effect (on ϕ) of the
1180 polarized target field as well as the drift chamber resolutions [37].

The θ -correlation can be studied mainly in two ways. The first way is to reconstruct and histogram the beam energy using the measured polar angles and the known target mass and then compare the histogram from the ND₃ target run with that from a pure NH₃ target run. The other equivalent way is to predict the proton polar angles (using the measured electron angles, known target mass and the beam energy) and then histogram the deviation of the measured proton angles from the expected values. We chose to use a slightly modified version of the latter approach in which we histogram the

following quantity⁹:

$$\Delta = p_p \cdot (\sin\theta_q - \sin\theta_p) \quad (3.13)$$

where p_p is the measured proton momentum, θ_p is the measured polar angle of the proton, and θ_q is the expected polar angle of the recoiling proton (which is also the angle of the exchanged virtual photon (q)) given by:

$$\theta_q = \tan^{-1} \left(\frac{M_p}{\tan(\theta/2) \cdot (E_{beam} + M_p)} \right) \quad (3.14)$$

The method exploits the fact that the width of the quantity Δ from data with deuteron target decreases because the Fermi motion of the protons in the deuteron nuclei gives a spread of the order of 50 MeV in transverse momentum, and for longitudinal particle momenta of order of a few GeV, we obtain a polar angle spread about 20 mr, which is much larger than the intrinsic CLAS resolution of about 2 mr.

3.9.2 Event Selection

First, for each data set (corresponding either to NH₃, ND₃ or ¹²C runs), using standard electron and proton identification cuts events each with a well reconstructed scattered electron and a similarly well reconstructed candidate for proton are selected. We accept only events each of which have one electron, one proton and at most one neutral particle candidate (expected to be a neutron coming off from the deuteron target break-up). If the event is one of the above two types, following additional cuts are applied to make sure it is elastic or quasi-elastic event:

- $E_X < 0.15$ GeV with $E_X = M_p + E_e - E_{e'} - E_p = M_p + \nu - E_p$
- $P_X < 0.5$ GeV/c with $\vec{P}_X = \vec{0}_p + \vec{P}_e - \vec{P}_{e'} - \vec{P}_{p'} = \vec{P}_e - \vec{P}_{e'} - \vec{P}_{p'}$
- $0.88GeV < M_X < 1.04GeV$
- $\theta_q < 49.0^\circ$
- $||\phi_e - \phi_p| - 180.0^\circ| < 2.0^\circ$

⁹We chose this quantity Δ rather than the simple angle difference ($\theta_q - \theta_p$) because the former is more directly interpretable in terms of transverse missing momentum for the case of quasi-elastic scattering.

1201 where X indicates the missing entity in the $d(e,e'p)X$ channel, which is ex-
1202 pected to be neutron in the case of the quasi-elastic channel, thus E_X is the
1203 missing energy and so on.

1204 If it passes these cuts, the quantity Δ is calculated for the event and then
1205 histogrammed as shown by the red curves in the top-left (from ^{12}C runs),
1206 top-right (from NH_3 runs), and bottom-right (from ND_3 runs) panels of Fig.
1207 3.35.

1208 After getting the histograms for the quantity Δ for the ep-elastic or
1209 quasi-elastic events from the NH_3 , ND_3 and ^{12}C target data sets, we first
1210 remove the contribution from the non-hydrogen component of NH_3 and ND_3
1211 targets by subtracting the corresponding carbon histogram (properly scaled
1212 to match with the shoulders from the background in each of the ammonia
1213 data). Since the carbon data is too low in counts (hence the raggedness in the
1214 histogram), a fit (a 'gaussian' times a 'linear' function) to the carbon data is
1215 obtained, and that fit (shown as the blue line in the first panel in Fig. 3.35
1216 is used instead of the histogram itself to remove the background. The blue
1217 line in the second (top-right) panel and the cyan line in the last (bottom-
1218 right) panel show the properly scaled carbon fits which are subtracted from
1219 the NH_3 and ND_3 histograms (shown by red lines) respectively. After the
1220 subtraction, we get new histograms that represent 'pure' elastic or quasi-
1221 elastic data from protons and deuterons (shown by the magenta lines in the
1222 third and last panels respectively).

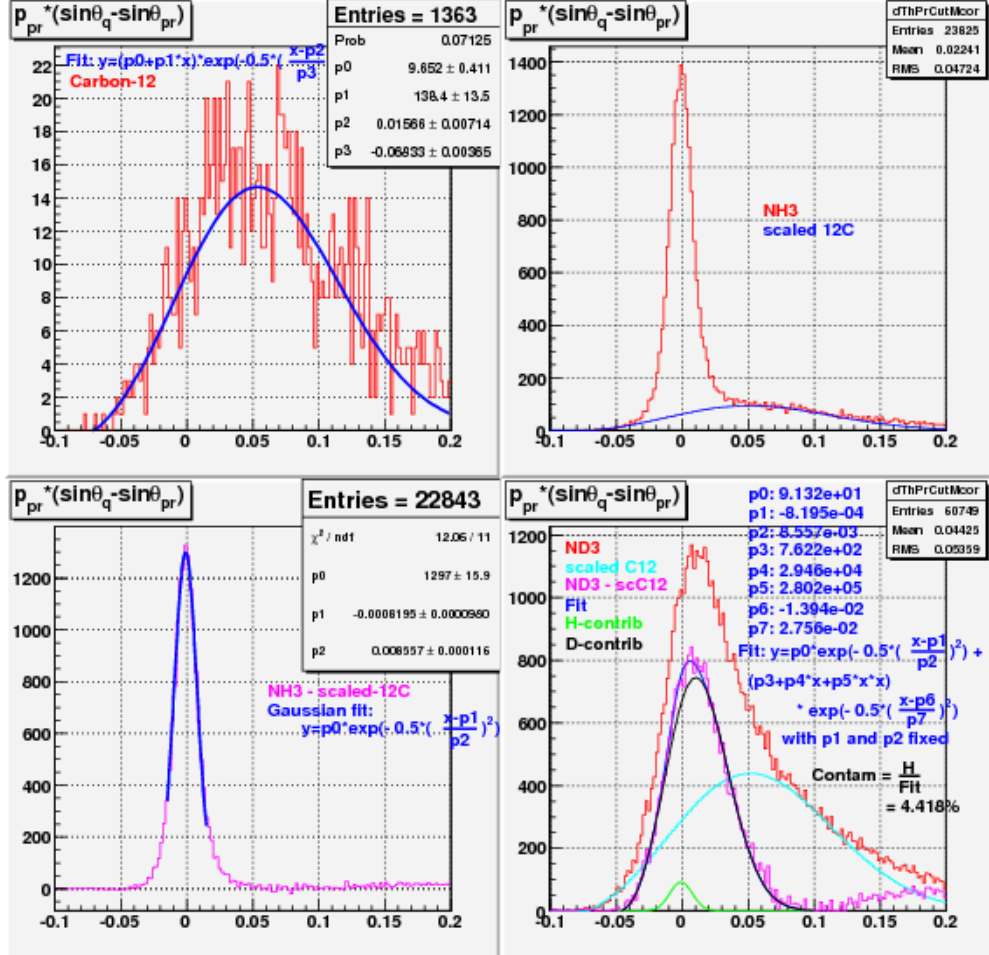


Figure 3.35: Histograms showing the quantity $\Delta = p_p \cdot (\sin\theta_q - \sin\theta_p)$ for elastic or quasi-elastic events from carbon-12 (top-left), NH₃ (top-right) and ND₃ (bottom-right) target runs respectively. The third (bottom-left) panel shows the background removed elastic events from the NH₃ data. In the fourth panel, various Δ are shown - red is the raw ND₃, light green is the scaled-¹²C for the nuclear background, brown is for the difference between the two.

3.9.3 Extracting the Contamination

After we have the 'pure' elastic or quasi-elastic data from NH₃ and ND₃ runs, we get the mean and the spread (standard deviation σ) of the proton elastic peak by fitting the NH₃ data to a Gaussian function $f_p(x)$ (the blue line in

1227 the third panel with parameters p0=height, p1=mean and p2= σ). After
 1228 we have the fit for the proton elastic peak, we fit the background subtracted
 1229 deuteron data to a function $f(x)$ that is a linear combination of the pure
 1230 proton fit and a pure deuteron fit (the latter with the form of **a quadratic**
 1231 **function \times a Gaussian**¹⁰) as follows:

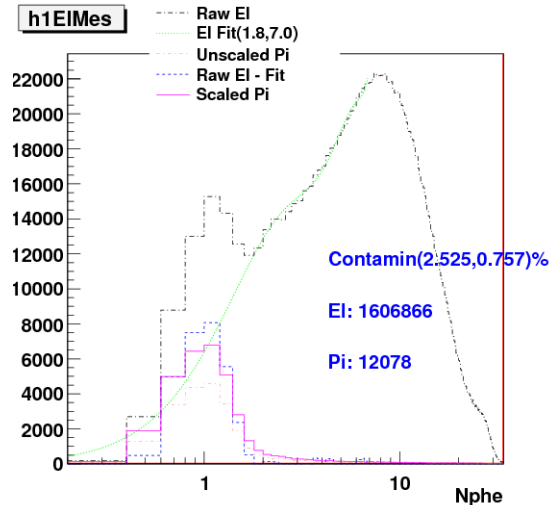
$$f(x) = p_0 \cdot f_p(x) + (p_1 + p_2 \cdot x + p_3 \cdot x^2) \cdot e^{-0.5 \cdot \left(\frac{x-p_4}{p_5}\right)^2} \quad (3.15)$$

1232 where p_i ($i = 0, 2, \dots, 5$) are the free parameters which are determined by
 1233 fitting of $f(x)$ to the deuteron data. The first term $p_0 \cdot f_p(x)$ in $f(x)$ represents
 1234 the contribution from the contaminant (i.e., protons in ND_3) and the rest
 1235 of the term in $f(x)$ represents the contribution from the deuterons in ND_3 .
 1236 The total fit function $f(x)$, the proton contribution and the deuteron part are
 1237 shown by the blue, green and black lines in the fourth panel. The ratio of
 1238 the area under the green line to that under the blue line gives us the relative
 1239 amount of the NH_3 contamination in the ND_3 target.

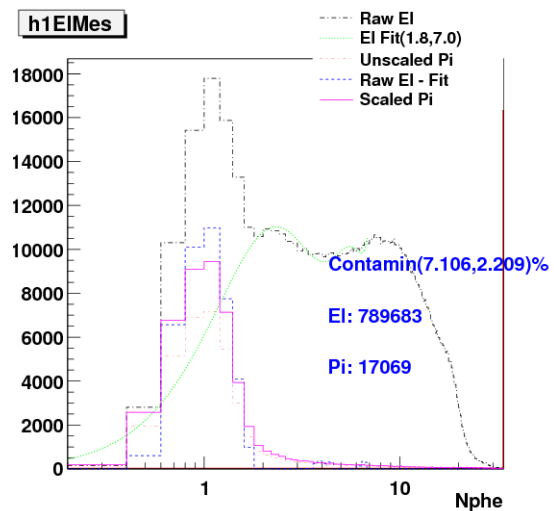
1240 3.9.4 Results and Conclusion

1241 From the calculation as described above, the estimate for the ND_3 contam-
 1242 ination came out to be 4.4% It was not possible to do a similar analysis on
 1243 the 1.3 GeV ND_3 data, because the CLAS acceptance constraints did not al-
 1244 low for the coincident detection of e and p from the exclusive (quasi-)elastic
 1245 events. The basic conclusion is that at 2 GeV, we cannot get a 'pure' Gaus-
 1246 sian spectrum for deuteron, and therefore, there is no way to unambiguously
 1247 separate deuteron from proton in ND_3 . The fact that the fit looks reason-
 1248 ably well (with contamination coming out to be only a few percent) and that
 1249 we clearly do not see a narrow peak on top of a wider one (unlike in EG1-
 1250 DVCS) should be sufficient to ascertain that EG4 did NOT have the same
 1251 contamination problem as EG1-DVCS (which still has not been explained
 1252 yet) [29]. To accommodate the fact that the contamination measurement is
 1253 not reliably unambiguous, we will assume a rather generous systematic error
 1254 due to the contamination.

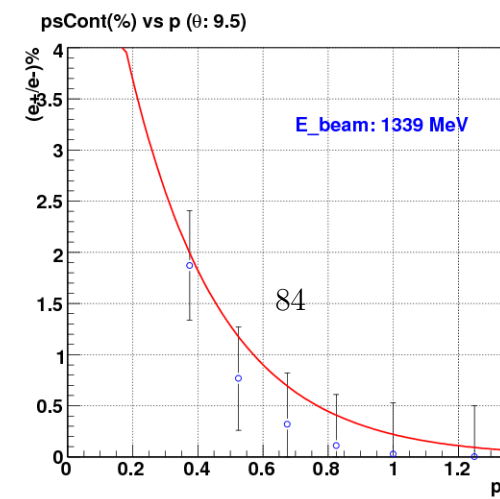
¹⁰A pure Gaussian and other forms for the deuteron spectrum were tried but the overall fit was not as good.



(a) For the first bin in momentum and seventh bin in θ .



(b) For the first bin in momentum and eighth bin in θ .



(c) Fits in the $\theta(9.0, 10.0)$ bin for 1.339 GeV

₁₂₅₅ **Chapter 4**

₁₂₅₆ **Monte Carlo Simulations and**
₁₂₅₇ **Extraction of g_1 and $A_1 F_1$**

₁₂₅₈ **4.1 Simulation and Approach to Analysis**

The EG4 data consist of a table numbers of electrons reconstructed within various (W, Q^2) bins that are scattered off polarized hydrogen (NH_3) or deuteron (ND_3), divided by the (life-time gated) integrated charge, for two different combinations of target polarization and beam helicity:

$$n^\pm = N^\pm / FC^\pm, \quad (4.1)$$

where “+” refers to beam helicity and target polarization anti-parallel, while “−” refers to the parallel case. The difference between these two normalized counts is given by

$$\Delta n(W, Q^2) = n^+(W, Q^2) - n^-(W, Q^2) = \mathcal{L}_r \cdot P_b P_t \cdot \Delta\sigma(W, Q^2) \cdot AccEff(W, Q^2) + Bg \quad (4.2)$$

₁₂₅₉ where the “relative luminosity” \mathcal{L}_r is a constant factor containing the density of polarized target nuclei per unit area and the conversion factor from
₁₂₆₀ Faraday cup counts to integrated number of electrons incident on the target;
₁₂₆₁ P_b and P_t are the beam and target polarization, Acc and Eff are the
₁₂₆₂ geometric acceptance and detection efficiency of CLAS for electrons within
₁₂₆₃ the kinematic bin in question (including cuts and trigger efficiency), and
₁₂₆₄ the background Bg comes from several sources, including pions misidentified
₁₂₆₅ as electrons, electrons from $e^+ e^-$ pair production, and electrons scattered off
₁₂₆₆ (partially) polarized target nucleons and nuclei that are not the
₁₂₆₇

intended species (e.g., bound protons in ^{15}N , free proton contamination in nominal ND_3 targets, and bound proton-neutron pairs in any ^{14}N contamination present)¹.

Our main goal is to extract the spin structure function g_1 and calculate its moments. The cross section difference $\Delta\sigma(W, Q^2)$ on the right side of the above equation is what contains the information on $g_1(W, Q^2)$ along with various other contributions.² This means we can, in principle, calculate the cross section (and then use that to extract g_1), from the background corrected measured quantity $\Delta n(W, Q^2)$ by putting in the values for all the rest of the quantities involved in Eq. 4.2. But, in reality, having an accurate knowledge of Acc and Eff is challenging and the available measurements of polarizations and luminosities are not reliable enough. So, experimenters usually resort to Monte-Carlo simulation to determine some or all of those factors that are involved in the relation between the counts and cross-section differences.

A standard way to extract the sought-after Physics quantities from these kinds of measurements proceeds along the following steps [39]:

1. Use a full simulation of CLAS with a “realistic” event generator, detector simulation and event reconstruction including cuts to obtain the product $AccEff$ as the ratio of events reconstructed in a particular bin, divided by events thrown in that same bin.
2. Extract the product $\mathcal{L}_r \cdot P_b P_t$ from the ratio of the acceptance and efficiency corrected Δn in the (quasi-)elastic region ($0.9 < W < 1.0$) to the well-known theoretical cross section difference for elastic (or quasi-elastic) scattering off the proton (deuteron).
3. Estimate and correct for Bg .
4. Apply radiative corrections, which use a model of the unradiated Born cross section and a calculation of the radiated cross section based on programs like RCSLACPOL (see below).

¹While this background is a small correction for hydrogen targets, in the case of deuteron targets, it must be corrected for (see Sec. 5).

² $\Delta\sigma(W, Q^2)$ also has contributions from the unmeasured g_2 or, equivalently, from the product $A_2 F_1$. Moreover, the cross section receives modifications and tails from radiative effects (both internal and external radiation) and kinematic resolution smearing.

- 1297 5. Express the extracted Born cross section difference in terms of the de-
 1298 sired quantity (here: g_1) and additional input (e.g., $A_2 F_1$). Use a model
 1299 for the latter to extract g_1 only. Vary the model (concurrently with the
 1300 model input to the previous step) to assess systematic uncertainties.

1301 One conceivable problem with this approach lies in the first step, and
 1302 in particular with the choice of the “realistic event generator”. This choice
 1303 would not matter at all if two conditions are fulfilled [39]:

- 1304 1. The kinematic bins are chosen so small that the variation of the cross
 1305 section over the bin (and/or the corresponding variation of the accep-
 1306 tance times efficiency) do not lead to any significant deviations for the
 1307 *average AccEff* between the simulation and the real detector.
- 1308 2. The counts reconstructed within any one bin are directly proportional
 1309 to the number of initial electrons generated within that *same* bin (the
 1310 proportionality constant being *AccEff*), without any “bin migration”
 1311 from other kinematic bins. (Otherwise, the ratio reconstructed/generated
 1312 depends on those “migration tails”, and the simulation will give differ-
 1313 ent results from the “true value” if the overall cross section model of
 1314 the generator is not accurate enough.)

1315 Unfortunately, assumption 1 tends to directly contradict assumption 2
 1316 because 1 favors small bins and 2 favors large bins! For most precision
 1317 experiments , bin migration effects are significant. This is aggravated by
 1318 the difficulty of making a clean separation between bin migration due to
 1319 detector resolution alone and the contribution from radiative effects. For
 1320 instance, GEANT and therefore GSIM includes (at least by default) photon
 1321 radiation as part of the simulation of outgoing electron tracks throughout
 1322 the gas and building materials of all detectors. It is very important not to
 1323 “double count” when simulating an experiment; the radiative calculations in
 1324 step 4 above should not include any “after” radiation beyond the limit of
 1325 the target itself (which, in turn, should then **NOT** be included in the GSIM
 1326 simulation as material to be traversed).

1327 This is a problem for all CLAS experiments attempting to extract abso-
 1328 lute cross sections (or, here, cross section differences); however, the problem
 1329 is magnified for our case: Since the cross section difference itself is not re-
 1330 quired to be positive, one can have both positive and negative tails migrating
 1331 into adjacent bins. In any case, it is clear that using the average, **unpolarized**

1332 cross section as a model for the generator is not really appropriate (unless
1333 one is confident that the asymmetry is fairly constant or slowly-varying – not
1334 a good assumption in the resonance region where the $\Delta(1232)$ with negative
1335 asymmetry is adjacent to the S11 with positive asymmetry). Using a (hope-
1336 fully realistic) model of the cross section difference instead would be much
1337 better, but this causes two new problems [39]:

- 1338 1. Prima facie it is unclear how to simulate a negative cross section (dif-
1339 ference). This problem can be circumvented fairly easily (see below),
1340 albeit at extra cost in terms of simulation effort.
- 1341 2. It obviously becomes impossible to extract $AccEff$ from a simple ratio
1342 of reconstructed divided by generated events; both of these quantities
1343 could be positive, negative (even different sign under extreme circum-
1344 stances), or simply zero (which is particularly bad for the denominator).
1345 From this discussion, it is also clear that such a ratio would depend very
1346 sensitively on the cross section model and bin migration tails and be a
1347 very poor indicator of the actual product $AccEff$.

1348 For this reason, we decided to try a different approach outlined in the
1349 following. The basic idea is to study the dependence of the reconstructed
1350 count difference on the model input (in particular g_1) directly through the
1351 whole chain of simulation and reconstruction, and then use tables of Born
1352 and radiated cross section differences for various model inputs as estimates
1353 of systematic uncertainties³.

1354 4.1.1 Outline of the method

1355 The basic idea is the following: If we already had a perfect model of g_1 and all
1356 other ingredients that go into Δn (including a perfect simulation of CLAS), a
1357 simulation of Δn would agree 100% with the data (within statistical errors).
1358 Any (larger than statistical) deviation between such a simulation of Δn and
1359 the data can only be due to the following possible sources:

- 1360 1. The model for g_1 is not perfect and, therefore, must be adjusted to
1361 reflect the “true” g_1 . This is the default assumption which we will use

³We developed this method for the case of an ND₃ target; however, it could, of course, easily be adopted to NH₃, as well

1362 to extract g_1 from the data. This will be done by finding the proportionality factor between *small* changes in g_1 and the reconstructed Δn
1363 and then adjusting g_1 to fully account for the observed Δn .
1364

- 1365 2. There could be a systematic error on this proportionality factor (which,
1366 after all, will come from simulation); for instance, there could be sys-
1367 tematic deviations from the simulated results for acceptance and effi-
1368 ciency (in particular efficiencies of the CC, EC, or tracking, that are
1369 not perfectly simulated by GSIM). This is a multiplicative uncertainty
1370 that must be carefully estimated and applied to the final data.
- 1371 3. Any imperfect simulation of the “background” due to all events not
1372 originating in the bin in question (migration, radiation), or due to
1373 undesired target components (hydrogen, bound polarized nucleons in
1374 nitrogen), or from misidentified pions or e^+e^- pairs, or due to contribu-
1375 tions to $\Delta\sigma$ from A_2 can lead to an additive systematic deviation
1376 that would then be misinterpreted as a change in g_1 . This systematic
1377 uncertainty must be studied by varying model inputs, parameters etc.
1378 in the simulation.

4.2 Radiative Corrections

The physics quantities that we seek to extract from measurements are theoretically defined or interpreted and calculated in terms of the cross-section of the so called “Born” scattering process, which is represented by the simplest possible Feynman diagram i.e., by the lowest order approximation of a single photon exchange process. However, the measured cross-sections also contain contributions from higher order electromagnetic processes, which must be accounted for before extracting the quantities of our interest. These additional contributions are grouped into two categories - **internal and external radiative corrections**.

The **internal corrections** are the contributions from the higher order QED processes (higher order Feynmann diagrams) which occur during the interaction. These include the correction for the internal Bremsstrahlung (i.e., the emission of a real photon while a virtual photon is being exchanged with the target) by the incoming or the scattered electron), the vertex correction (in which a photon is exchanged between the incoming and the scattered electron), and the correction for the vacuum polarization of the exchanged virtual photon (e^+e^- loops).

External corrections include those that account for the energy loss (mainly by the Bremsstrahlung process) of electrons well before or after the interaction while passing through the target material and the detector.

If the beam electron radiates a photon before the scattering, the kinematics of the actual process will be different from the the one calculated with the nominal beam energy. Likewise, if the radiation occurs after the scattering, the actual energy and momentum of the scattered electron will be different from what is calculated normally (i.e., without any radiation). The effect can be quite large for elastic scattering.

1406

4.3 “Standard” simulation

The simulation process consists of mainly three parts - generating inclusive events similar to the ones produced in the double polarization scattering process, simulating the CLAS detector response, and finally the event reconstruction from the simulated detector signals.

The first part is accomplished by using a program that is made by combin-

1413 ing the essential elements of an updated version of the “RCSLACPOL” pro-
1414 gram (for cross section generation) and some parts of the “STEG” event gen-
1415 erator (see sections 4.3.1 and 4.3.2). The second part is done by two standard
1416 CLAS software packages running in succession - “GSIM” and “GPP”(see sec-
1417 tions 4.3.3 and 4.3.4). And, finally, the standard CLAS package “RECSIS”
1418 is used to reconstruct the events in the same way as for the real CLAS data.

1419 4.3.1 RCSLACPOL

1420 The simulation for the standard model cross sections proceeds as follows.
1421 We use the code “RCSLACPOL” [40] that can generate polarized and un-
1422 polarized cross sections (both Born and radiated) based on the approach by
1423 Shumeiko and Kuchto [41] as well as Mo and Tsai [42], including external
1424 radiation in the target. This code has been extensively tested and used for
1425 the analysis of SLAC experiments E142, E143, E154, E155 and E155x as
1426 well as Jefferson Lab experiments like EG1a and EG1b. It has been updated
1427 with the most recent models on polarized and unpolarized structure func-
1428 tions (F_1, F_2, A_1 and A_2) [40, 43–45] and an implementation of the folding
1429 algorithm developed by W. Melnitchouk and Y. Kahn [46] for structure func-
1430 tions of the deuteron. The models have been fitted to and tested with data
1431 from EG1b as well as world data on both A_1 and A_2 over a wide range of Q^2
1432 and W , including the resonance region and the DIS region.

1433 For EG4, we have combined the “RCSLACPOL” code with that of the
1434 “STEG” event generator. This generator uses a grid of (radiated) cross sec-
1435 tions generated by our modified version of RCSLACPOL to generate events
1436 that are distributed according to these cross sections (i.e., the number of
1437 events generated in a given bin is proportional to the cross section integrated
1438 over this bin).

1439 4.3.2 Event Generator

1440 The concept and some part of the generator skeleton was inherited from the
1441 STEG (SimplesT Event Generator) program obtained from INFN, in Genova,
1442 Italy. The old event sampling part (which made the program run extremely
1443 slow) of the code was replaced by a new one developed by myself which
1444 made the event generation process much faster. The cross section calculating
1445 part was replaced by codes from an updated version of RCSLACPOL (see
1446 Sec. 4.3.1).

1447 The generator works in two steps. First, it generates two two-dimensional
1448 maps or tables of radiated inclusive polarized cross differences (for the scat-
1449 tering of polarized electrons from a longitudinally polarized deuteron tar-
1450 get, by using RCSLACPOL) in various kinematic bins encompassing the
1451 kinematic region covered by EG4 data. These cross section maps (and the
1452 corresponding events later on) were generated in the following angular and
1453 momentum ranges: 5.0-45.0 degrees for θ , 250.0-325.0 degrees for ϕ (to en-
1454 sure the CLAS 6th sector is completely covered) and $(0.2, E_{beam})$ GeV for the
1455 momenta, where the beam energy E_{beam} took values of 1.337 and 1.993 GeV,
1456 corresponding to the two ND_3 data sets of EG4. In our case, the map was
1457 created by dividing the kinematic phase space into a grid of small rectangles
1458 and then calculating the differential cross-section at the geometric center of
1459 each of those squares (such as ABCD in Fig. 4.1). For our application, we
1460 need to generate two such maps (because of the impossibility of generating
1461 events according to negative cross-sections) and run the program twice - once
1462 corresponding to positive $\Delta\sigma$ and the next for the negative one. For all bins
1463 in which the integrated cross section $\Delta\sigma \geq 0$, we fill the first table (“positive
1464 map”) which is therefore positive-definite. For all bins in which this cross
1465 section is below 0, we fill a second table (“negative map”), but with the
1466 absolute (i.e. negative) value of this cross section.

1467 In the second stage, events are thrown according to the cross section maps
1468 produced in the first stage. The events are given vertex coordinates that are
1469 uniformly distributed over the volume of a 1 cm long cylinder with radius
1470 0.01 cm around the beam line - with the center of this volume being at the
1471 EG4 target position of $(0,0,-100.93$ cm). Nearly equal numbers of events are
1472 generated for each sign of $\Delta\sigma$ they are finally normalized according to their
1473 total cross sections (integrals of the corresponding maps).

1474 The kinematic and other information (positions, momenta, charge) of
1475 these generated events are recorded and saved in the BOS format⁴ output
1476 files which organizes data into banks. In our case, HEAD, MCEV, MCTK,
1477 and MCVX banks are used for the generator output. The generator is also
1478 capable of producing output in the hbook format which makes it possible
1479 to study the Monte Carlo data using PAW (or ROOT because the h2root
1480 program easily converts “hbook” files into “root” files).

⁴Existing versions of GSIM, GPP and RECSIS accept only BOS format for input files.

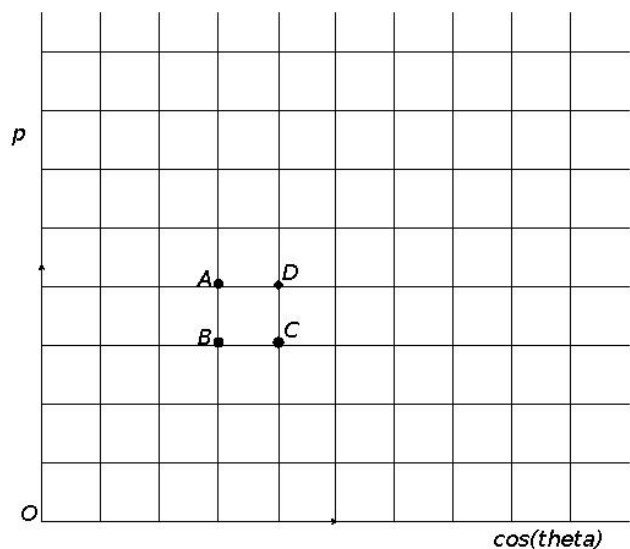


Figure 4.1: Corners of a typical bin highlighted in the kinematic space covered by the event generator.

4.3.3 GSIM - CLAS Detector Simulation

The Monte Carlo events thus generated are next fed into GSIM - the CLAS Monte Carlo simulation program using GEANT 3.21 libraries from CERN [47]. It simulates the CLAS detector response by implementing a complete model of the detector as well as the propagation of particles through different materials including all physics processes, such as multiple scattering, energy loss, pair production, and nuclear interactions. The program takes the input event particles and then, based on their types, momenta and positions, “swims” (traces) them through all volumes of different materials that are defined using various library routines and the detector parameters. Charged particles are also subjected to the effects of the torus and target magnetic fields of the same strength as in the actual experiment (for this the same field maps are used as in the track reconstruction process using RECSIS). All the ingredients of the program (field maps, active detection volumes, passive volumes of detector support structures etc) are modeled as accurately as possible with the help of engineering designs and actual detector measurements. Special subroutines corresponding to various active parts of the detector produce outputs resembling the real detector signals which can then be reconstructed and analyzed just as the real experimental data [48][49]. GSIM is configured to match with the conditions of a given experiment by giving it proper values of input parameters via a command line input file which contains various “ffread cards” some of which are listed in table-A.1 along with their values that were used in our simulation.

4.3.4 GSIM POST PROCESSOR (GPP)

The GSIM output is next passed onto GPP - another standard CLAS software package - to process the simulated data further so that the detector response is accounted for more accurately. This package improves the response by smearing the detector signals and removing them if there are dead regions (determined by querying a data base which in turn is made by looking at the raw data of the experiment).

A lot of known, unknown, quantified, and unquantified factors such as temperature, alignment, dead channels, electronic malfunction etc affect the performance of the CLAS detector. But, GSIM does not include all these effects and, hence, the efficiency of the detector is always less than what the

1516 simulation provides us. To make the simulation more realistic by taking into
1517 account some of those effects, another CLAS software called GSIM Post Pro-
1518 cessor (GPP) is used to process the GSIM output. The GPP can change the
1519 DC, SC, CC and EC signals produced in the simulation. The DC signals can
1520 be changed by (a) accounting for the dead wires according to the calibration
1521 database, (b) shifting the DOCA mean value, and (3) smearing the hit sig-
1522 nals according to the resolution determined by the calibration database or
1523 according to the command line input. Likewise, SC signals can be changed
1524 with a parameter input for smearing the time resolution. And, for the CC
1525 and EC signals, the GPP can use the hardware thresholds[50].

1526 As the experimental conditions and detector configurations can change
1527 from one experiment to another, in order to run the GPP, we must have
1528 our own experiment specific calibration constants and parameters such as
1529 the run number (R), the DC smearing scale values for regions 1, 2 and 3
1530 (a, b, c) and the SC smearing scale value (f). Even for a given experiment,
1531 these constants and parameters are determined to be different for different
1532 data sets (corresponding to a given beam energy, for example). The value
1533 for R can be any run number belonging to a specific data set. This number
1534 is used to identify the entry of the calibration constants in the database that
1535 corresponds to the given data set. In order to simplify the job, we decided to
1536 use the timing resolutions determined by the calibration database assuming
1537 that they are good enough and need only to determine new values for the
1538 DC smearing. To further simplify the job, we assumed that the three DC
1539 Regions had identical resolutions, so the DC smear parameters a, b, and c
1540 would have the same values, and the common DC-smear value is what is
1541 determined from the procedure described below.

1542 In order to determine the DC-smear, we generated a statistically signif-
1543 icant number (about half million) of elastic-electron events distributed ac-
1544 cording to the elastic cross section and then ran them through GSIM, GPP
1545 and RECSIS. The pure proton target events, turning off the radiative effects
1546 are generated using the existing STEG event generator.

1547 The simulated elastic events are then fed into GSIM, GPP and RECSIS,
1548 with GSIM and RECSIS used in the same configuration as when processing
1549 the CLAS data during the “pass-1” phase, and GPP run with different values
1550 of DC-smear scales as inputs. The reconstructed data coming out of RECSIS
1551 corresponding to a given value of DC-smear is then histogrammed in ΔE
1552 again and fitted to a Gaussian to get its σ (characterizing width) of and
1553 mean (characterizing position). As we can see in figures 4.2(a) and 4.2(b),

the width of the elastic peak increases with the DC-smear but the position stays more or less the same as expected. In fact, when the two are plotted against DC-smear (as in figures 4.3(a) and 4.3(b)) the width shows a linear dependance.

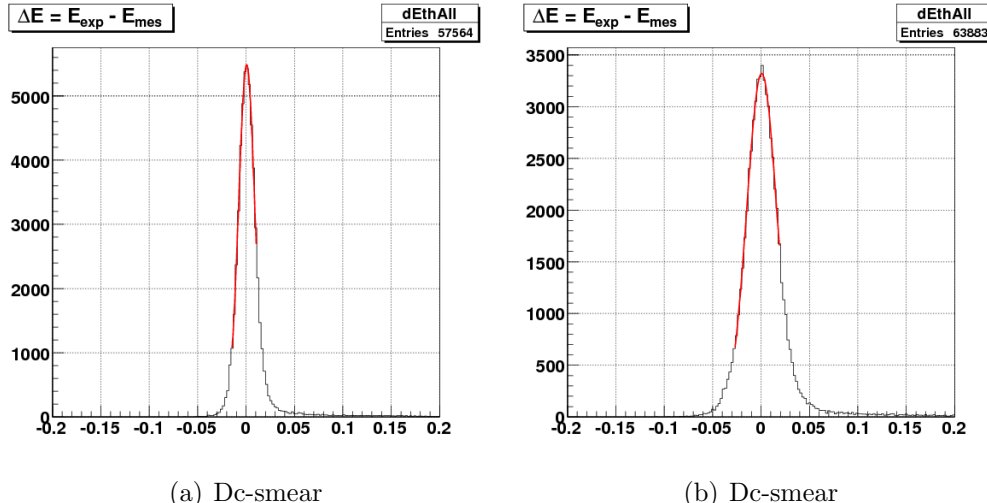
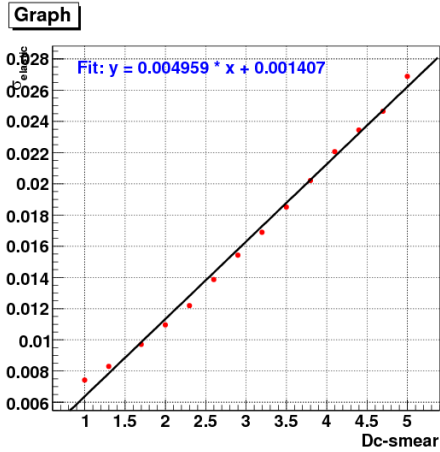
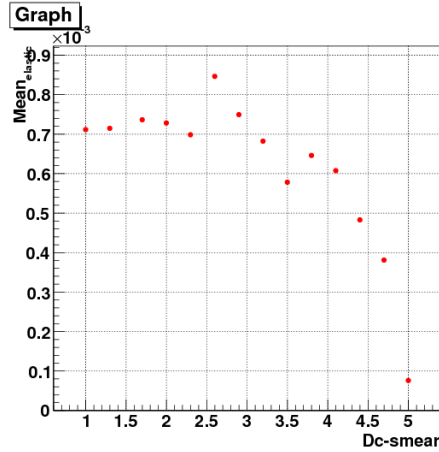


Figure 4.2: ΔE of 2.3 GeV simulated elastic-only proton-target events passing through GSIM, GPP (with two different Dc-smear scales), and RECSIS.

(a) σ vs DC-smear

(b) Mean vs DC-smear

Figure 4.3: Graphs showing the dependence of width and position (obtained from the Gaussian fits as shown in the fig (??) of the elastic peaks on the DC-smear applied to GPP.

1558 4.3.5 Finding the width of the real CLAS data elastic 1559 peak.

1560 With the knowledge of the DC-smear dependence of energy resolution (Fig.
1561 4.3(a)), if we also know the resolution in the real data, we can determine
1562 the right value of DC-smear which would make the resolution in the
1563 simulation comparable with that in the real data. So, the next step is to find
1564 the resolution in the real CLAS data, which is done again by measuring the
1565 width of the elastic peak in the real data. But, because the real data is a very
1566 complex mixture of events coming from various reaction channels, we must
1567 first have a way to separate the elastic data from the rest. One method entails
1568 histogramming ΔE from both the NH_3 and ^{12}C target data (for a given beam
1569 energy) and subtracting the latter (after the cross-normalization) from the
1570 former (as in fig (4.4)) to effectively remove the contribution from nitrogen
1571 component of the NH_3 target leaving the contribution coming only (mostly)
1572 from the proton component. Another method consists of using only the NH_3
1573 data but this time calculating the helicity dependent cross-section difference
1574 in the elastic region Fig. (4.5). In the latter method, the difference removes
1575 the contribution from the unpolarized nuclear background because they have

1576 the same contribution to the opposite helicity state cross-sections. After the
 1577 elastic data is separated, its ΔE distribution is fitted to a Gaussian as with
 1578 the simulation data and we arrive at the experimental energy resolution.

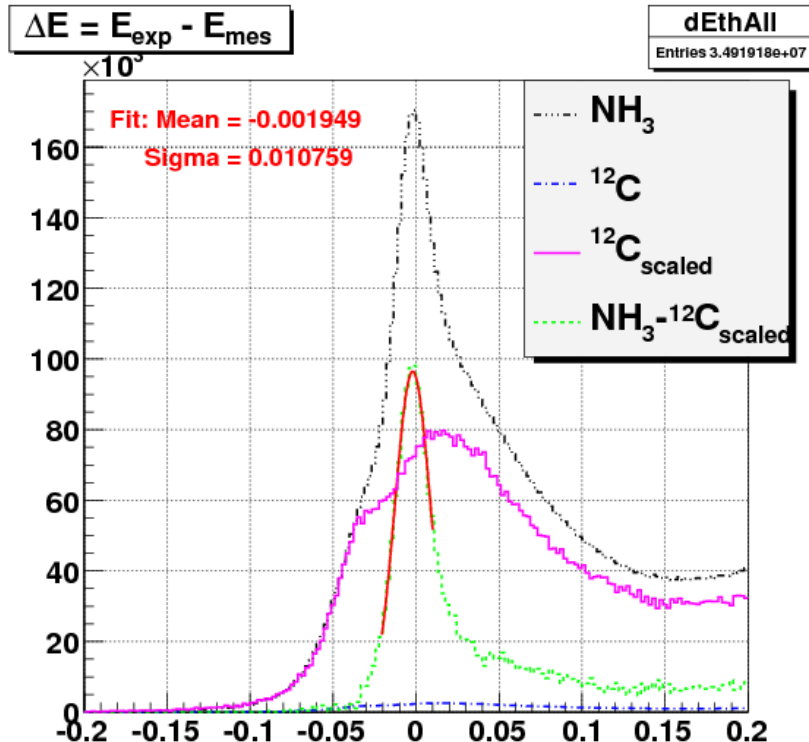


Figure 4.4: Histograms illustrating the extraction of elastic peak for 2.3 GeV by using carbon-12 data for background removal from the total-cross section (all good electrons with $\theta > 7$ used).

1579 Using the first of the two methods mentioned above, the real data reso-
 1580 lutions were evaluated for three different polar angle (θ) cuts - all θ (in fact
 1581 $\theta \geq 7^\circ$), $\theta > 15^\circ$, and $\theta > 20^\circ$. The dependence of these experimental reso-
 1582 lutions on the beam energy for these cases are shown together in the Fig.
 1583 4.6, along with the resolution for the case “all θ ”, but determined from the
 1584 cross-section difference method. Likewise, as described above, the DC-smear
 1585 dependence of the simulated resolution were determined separately for all
 1586 these three cases of angle cuts, so that we could compare the experimental
 1587 resolutions with the simulations correspondingly. One such comparison is

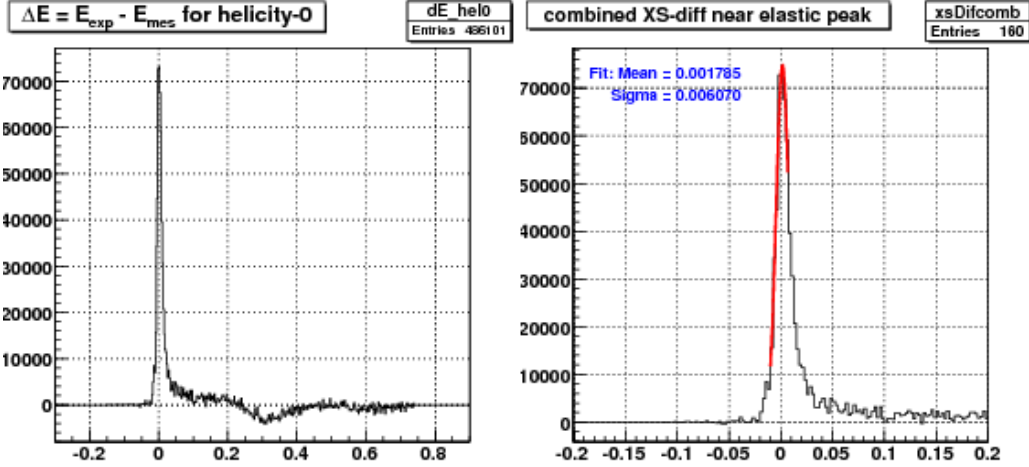


Figure 4.5: Plots showing the cross-section difference for 2.3 GeV NH₃ target data with the right one zoomed in around the elastic region (all good electrons with $\theta > 7$ used).

1588 illustrated in the figure 4.7, where we show resolutions evaluated for the case
 1589 of “all θ ” - first two for the experimental data and the rest for the simulated
 1590 data.

1591 Looking at Fig. 4.6, it is obvious that the resolution is θ -dependent as ex-
 1592 pected. When the experimental and simulated resolutions are compared for
 1593 the three different cases of θ cuts, we realize that the GPP asks for the θ de-
 1594 pending DC-smearing, which makes the simulation work very complicated
 1595 with the current version of GPP. To simplify the situation, we decide to have
 1596 a global (θ independent) value of DC-smearing (for a given beam energy)
 1597 by comparing the experimental and simulated resolutions corresponding to
 1598 the case of “all θ ” cut. That should be good enough for practical purposes.
 1599 By taking into account the fact that there seems to be an inherent uncer-
 1600 tainty in the measurement of the resolutions (evident from the discrepancy
 1601 of the experimental resolutions determined from the two different methods)
 1602 and comparing the experimental and simulated results, the values as listed
 1603 in Table. 4.1 are chosen for the DC-smearing scales for the GPP.

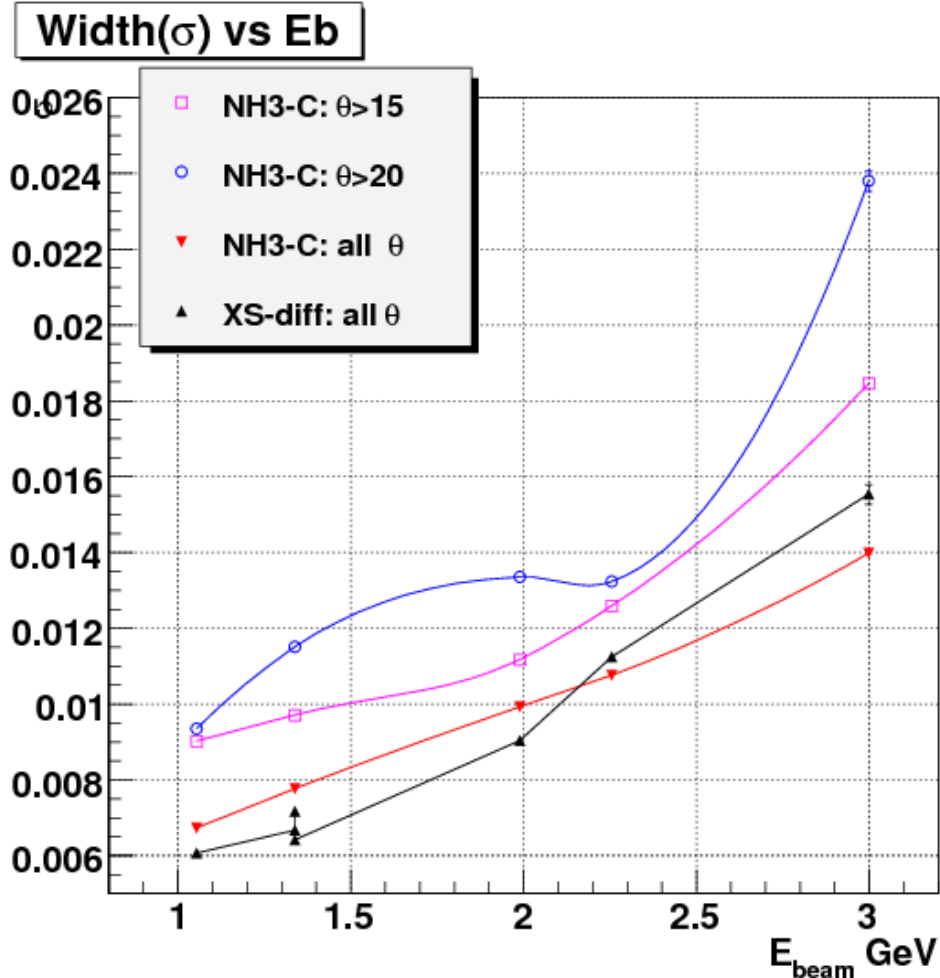


Figure 4.6: Graphs showing the dependence of width (σ) of the elastic peaks (from experimental data) on the beam energy (GeV).

Table 4.1: DC-smearing scales determined for different beam energies.

E_{beam} (GeV)	1.054	1.339	1.989	2.256	2.999
DC-smear	2.6	2.0	2.0	2.0	1.7

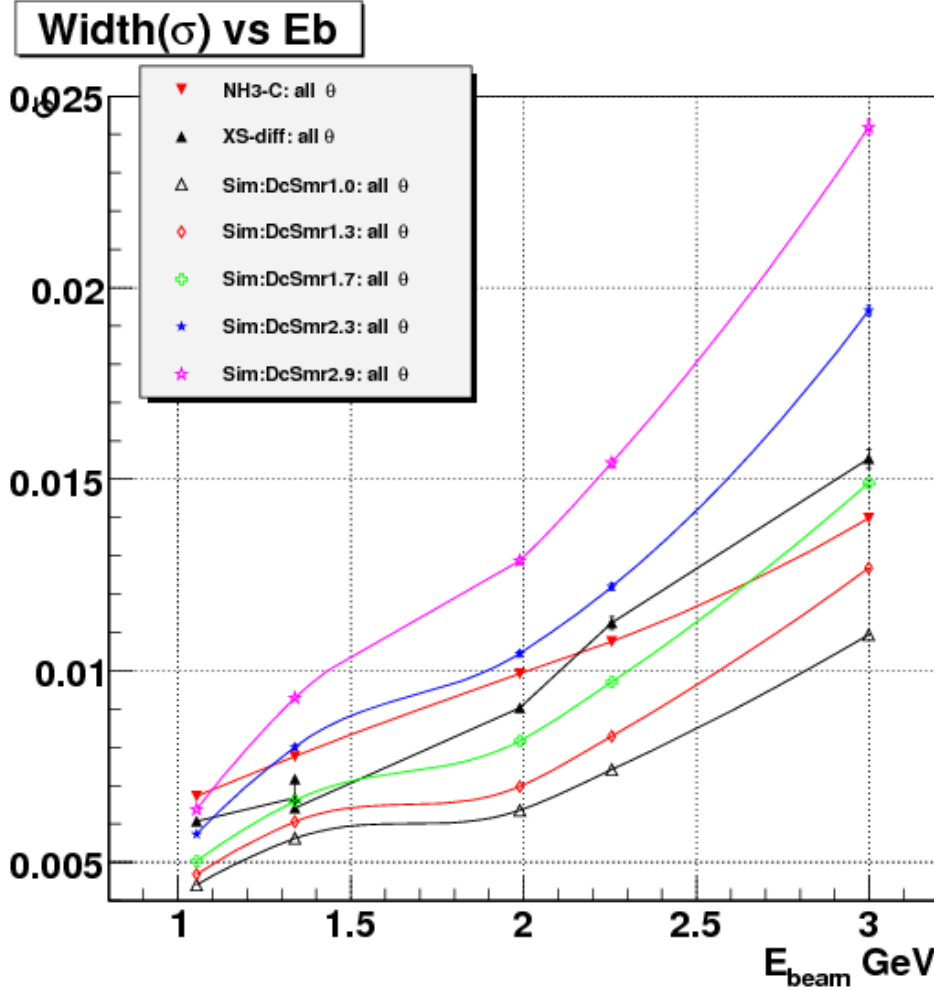


Figure 4.7: Graphs showing the dependence of width (σ) of the elastic peaks (from both experimental and simulated data) on the beam energy (GeV).

1605 4.4 Comparison of Data and Simulation

1606 Using our final values for the smear parameters, the simulated data were
 1607 passed through GPP and then reconstructed with RECSIS. Finally, all ap-
 1608 plicable cuts and corrections were applied to both sets of polarized simu-
 1609 lation data. Because the CC was turned off in GSIM for the simulation, all
 1610 experimental data cuts except those depending on CC were applied to the
 1611 simulated data. However, the cuts were modified (see Sec. 3.3) to account

₁₆₁₂ for differences between simulation and data.

In the end, we had two sets of simulated events (for the two cases of $\Delta\sigma \geq 0$ and $\Delta\sigma < 0$) in each kinematic bin. The number of these two type of events in each bin were then cross-normalized with respect to each other by their respective cross-section map integrals and the number of generated Monte-Carlo events and then combined to make the simulated polarized count difference Δn . To do that, the number of simulated event counts in a kinematic bin corresponding to the positive $\Delta\sigma$ was kept unchanged but the one corresponding to the negative $\Delta\sigma$ was multiplied with the following normalization factor:

$$norm^- = \frac{\sigma_{tot}^-}{\sigma_{tot}^+} \times \frac{N^+}{N^-} \quad (4.3)$$

₁₆₁₃ where $\sigma_{tot}^{+/-}$ and $N^{+/-}$ are the total integral of the cross section map and
₁₆₁₄ the corresponding number of Monte-Carlo events generated for each of the
₁₆₁₅ polarization cases (+/-).

The next step was to properly cross-normalize the simulated events to the data, as outlined in the introduction. For this, we found the scale factor SF necessary to have the same Δn in the quasi-elastic region (e.g., $0.9 \leq W \leq 1.0$). This factor represents the ratio

$$SF = \frac{n^+ - n^-}{\Delta n(simul)} \quad (4.4)$$

₁₆₁₆ since we assume that the simulation for the cross section difference in this
₁₆₁₇ region is reliable and all other factors are common to the simulation and the data.
₁₆₁₈ In fact, we chose one Q^2 bin (the 20th one - for which the agreement
₁₆₁₉ between the data and simulation was among the best) and calculated above
₁₆₂₀ ratio to get the global preliminary value of the scaling factor SF_{20} . The sim-
₁₆₂₁ ulated Δn was then multiplied with this factor to get our best “prediction”
₁₆₂₂ of the real data in all the kinematic bins, in order to directly compare it with
₁₆₂₃ the real data (see Figs. 4.8 and 4.9).

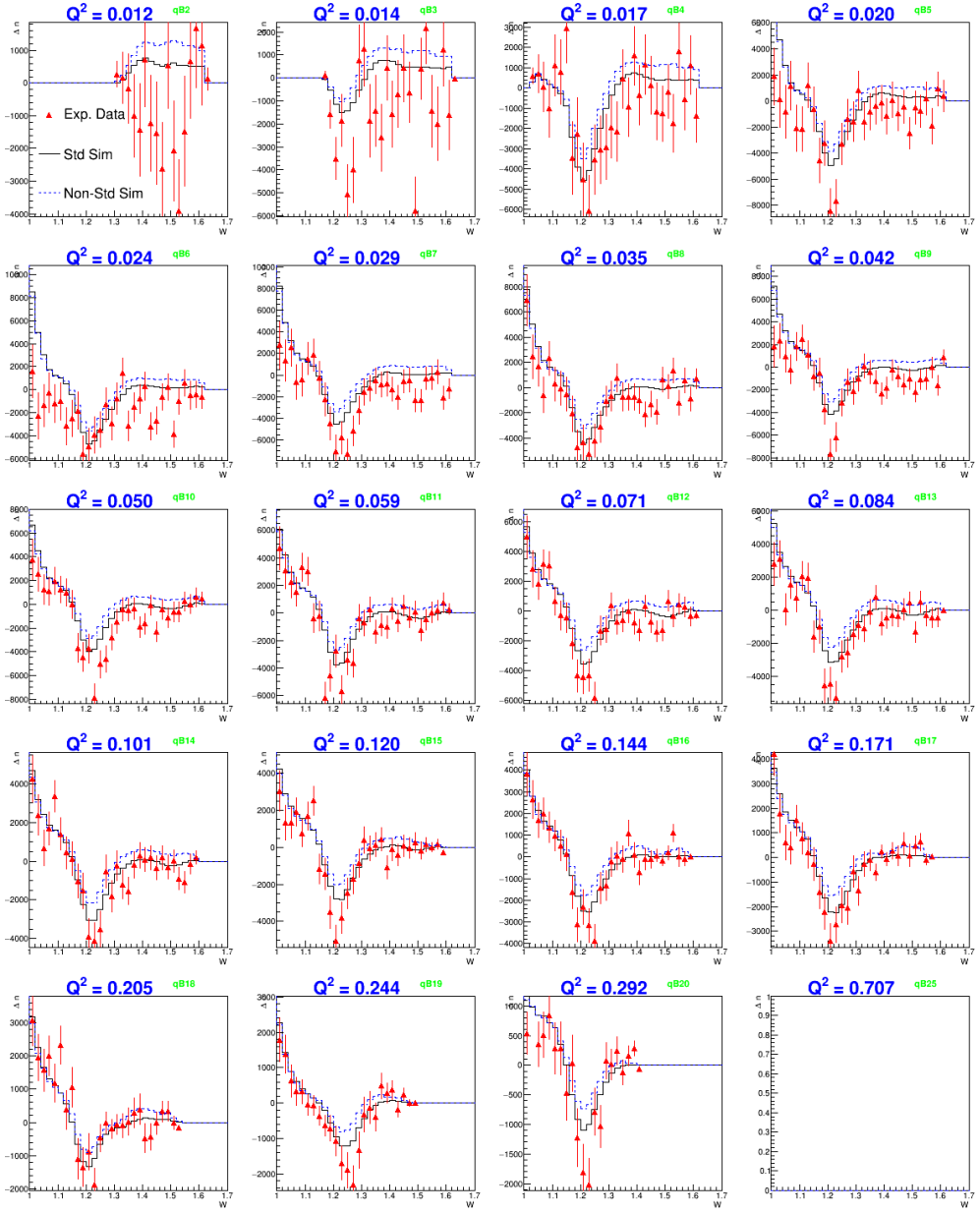


Figure 4.8: Comparison (in different Q^2 bins) of polarized count differences from 1.3 GeV experimental (red points with error bars) and two versions of normalized simulation data. The black continuous histograms are for “standard” simulation with values of A_1 set as given by the used model. The blue dotted histograms are for “non-standard” simulated data with A_1 changed to $A_1 + 0.1$.).

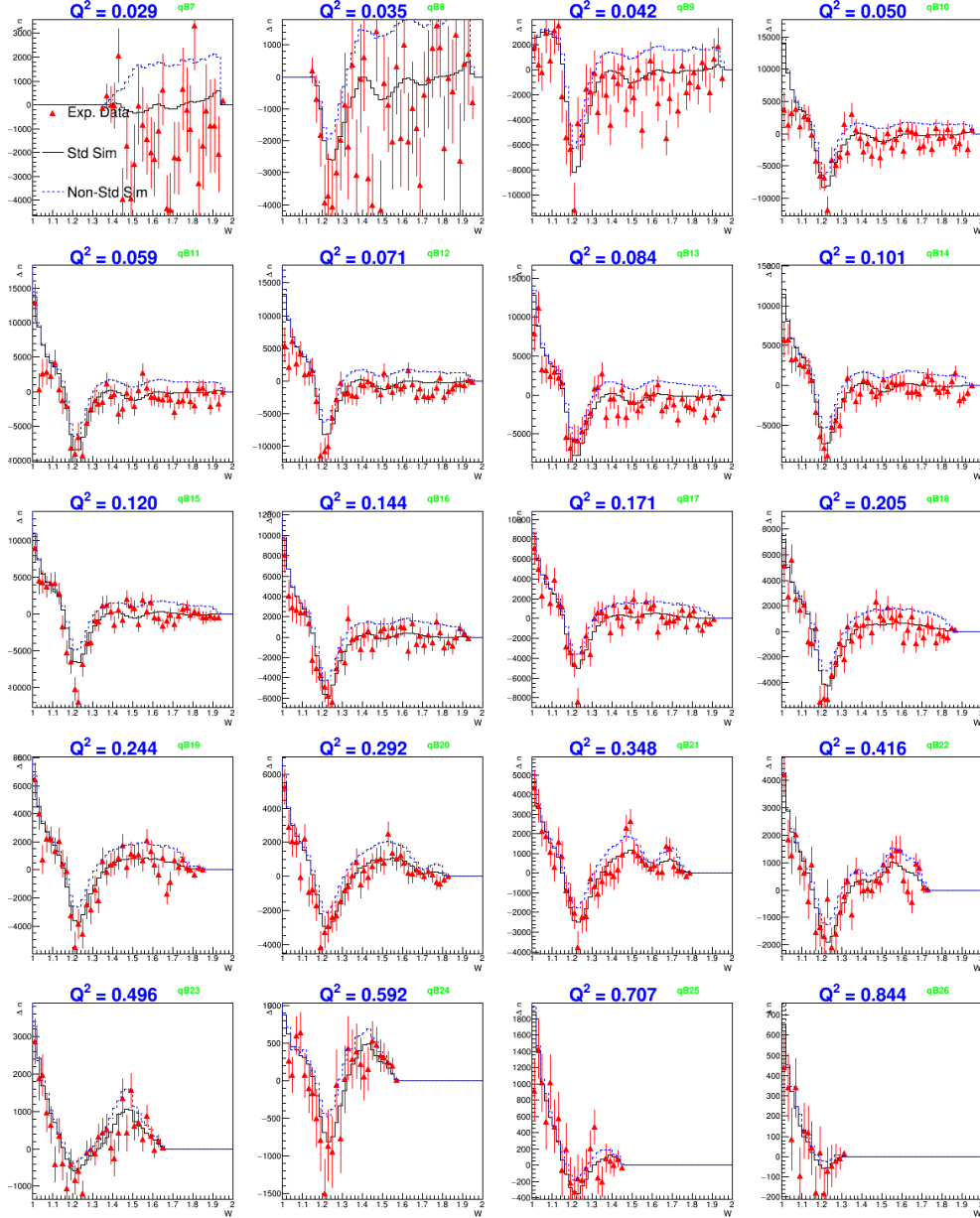


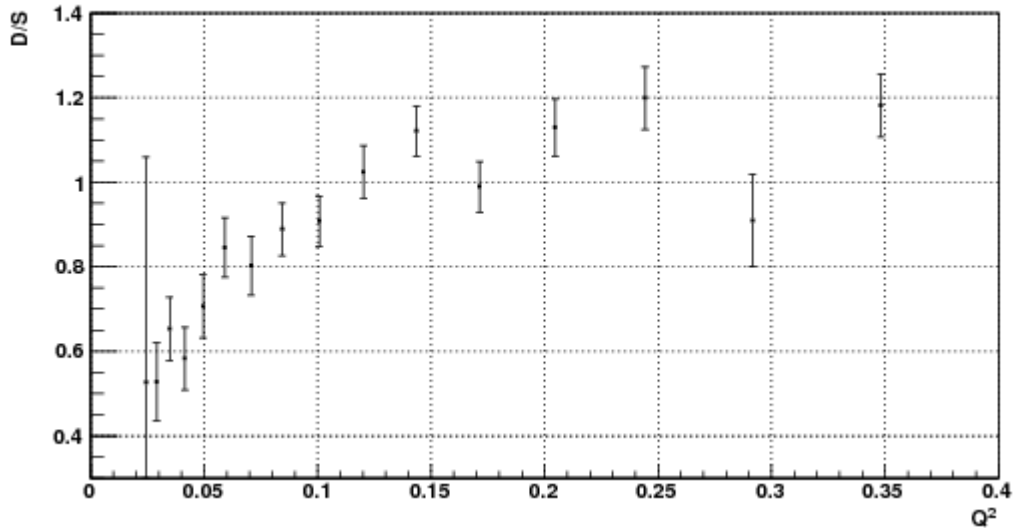
Figure 4.9: Comparison (in different Q^2 bins) of polarized count differences from 2.0 GeV experimental (red points with error bars) and two versions of normalized simulation data. The black continuous histograms are for “standard” simulation with values of A_1 set as given by the used model. The blue dotted histograms are for “non-standard” simulated data with A_1 changed to $A_1 + 0.1$.

1624 After this normalization, the ratios $(n^+ - n^-)/\Delta n(simul)$ in the quasi-
1625 elastic region for all Q^2 bins were calculated and plotted versus Q^2 as well as
1626 θ (see Figs. 4.10(a) - 4.13(a)) along with the corresponding statistical errors
1627 as given by $\sqrt{(n^+ + n^-)/\Delta n(simul)}$. As the figures show, the ratio in the
1628 quasi-elastic region drops off rapidly at small Q^2 . The fall-off is likely due
1629 to CC inefficiencies for very high momenta and very forward angles. Also,
1630 our simple cross section model for the deuteron is less accurate at low Q^2 .
1631 Figs. 4.10(b) - 4.13(b) show that the Δ -resonance region does not suffer from
1632 similar problems.

1633 The final normalization was obtained by calculating the error weighted
1634 average $SF_{average}$ of above ratios in the quasi-elastic region. The average was
1635 calculated using only those Q^2 bins which had ratios reasonably stable and
1636 closer to each other. Because, the ratios are reasonably stable only above
1637 $Q^2 \approx 0.045$ GeV 2 and $Q^2 \approx 0.09$ GeV 2 in the 1.337 and 2.0 GeV data sets
1638 respectively (as can be seen from Figs. 4.10(a) and 4.12(a)), only those Q^2
1639 bins above these two limits were used in calculating the weighted average of
1640 these ratios. In addition, even above those two limits, some of those which
1641 had too large ratios - greater than 2.0 (or 2.5) for 1.337 (or 2.0) GeV data
1642 set- were not used in the weighted average. However, it should be noted that
1643 the bins not used in the average ratio calculations were not entirely discarded
1644 from the final analysis. Only those below $Q^2 = 0.02$ GeV 2 were completely
1645 thrown out from the final analysis because they did not cover the resonance
1646 (particularly the Δ) region very well. The resulting simulated data in the
1647 form of count differences Δn in various Q^2 bins are shown in Figs. 4.8 and
1648 4.9 along with the corresponding experimental data.

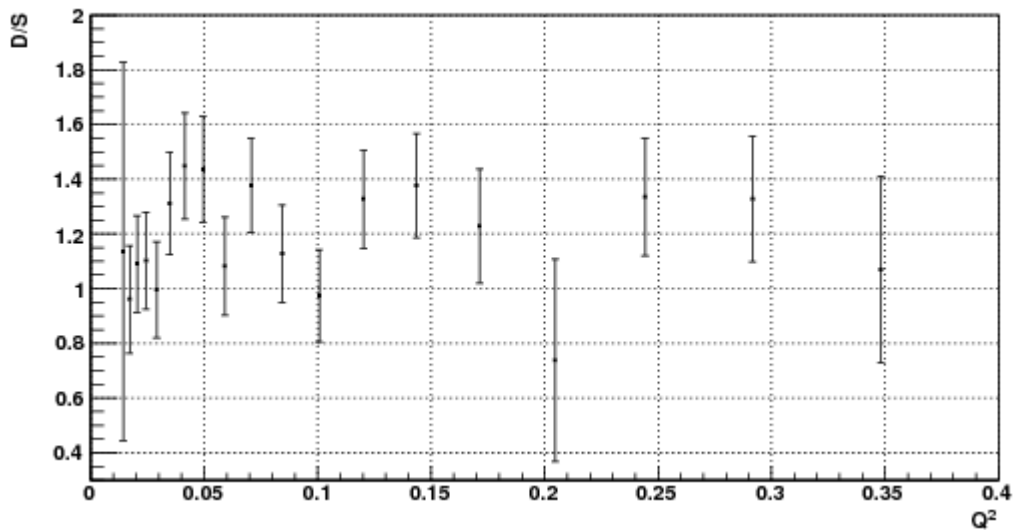
1649 A complete systematic error analysis was done to study the effect of the
1650 overall scaling factor SF on the extracted g_1 (see below) and to estimate
1651 its statistical (due to the number of counts) and systematic (due to model
1652 uncertainties and backgrounds) error.

Data/Sim for W(0.9,1.05)



(a) Data/Sim ratio vs Q^2 in 1.3 GeV quasi-elastic data.

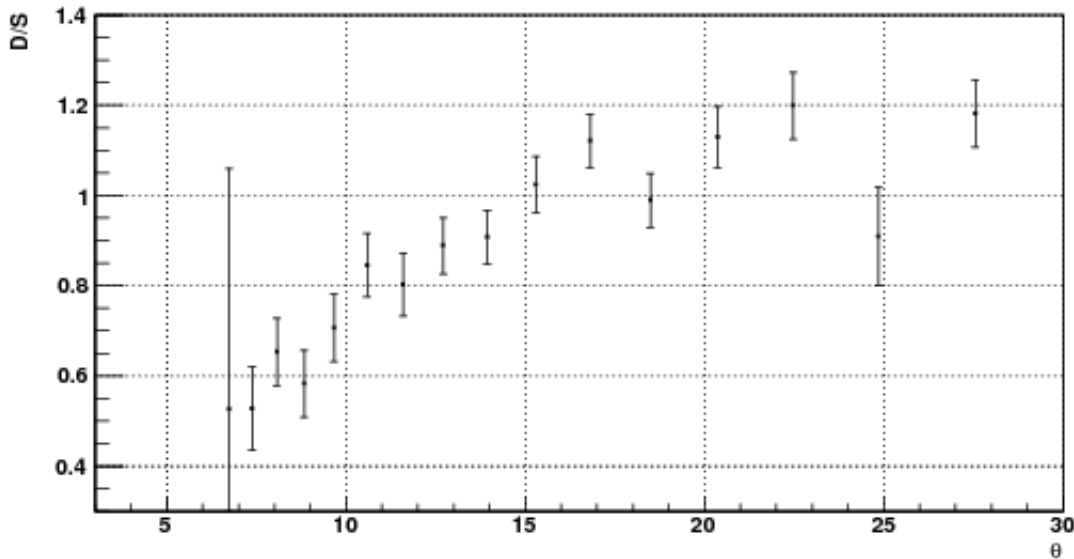
Data/Sim for W(1.15,1.3)



(b) Data/Sim ratio vs Q^2 in Δ -resonance region of 1.3 GeV data.

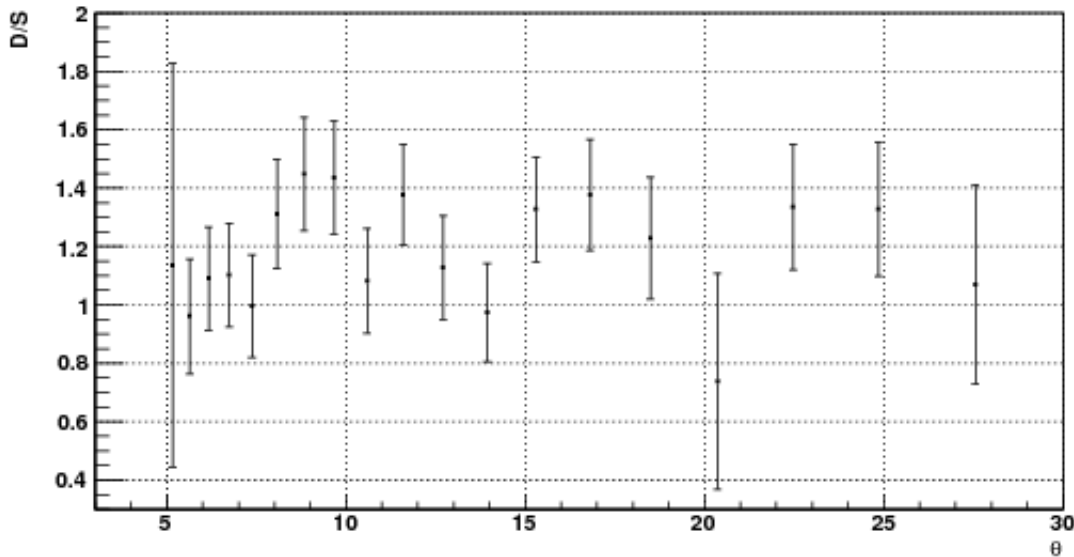
Figure 4.10: Q^2 dependence of ratios of 1.3 GeV data and simulation in the quasi-elastic and Δ -resonance regions.

Data/Sim for W(0.9,1.05)



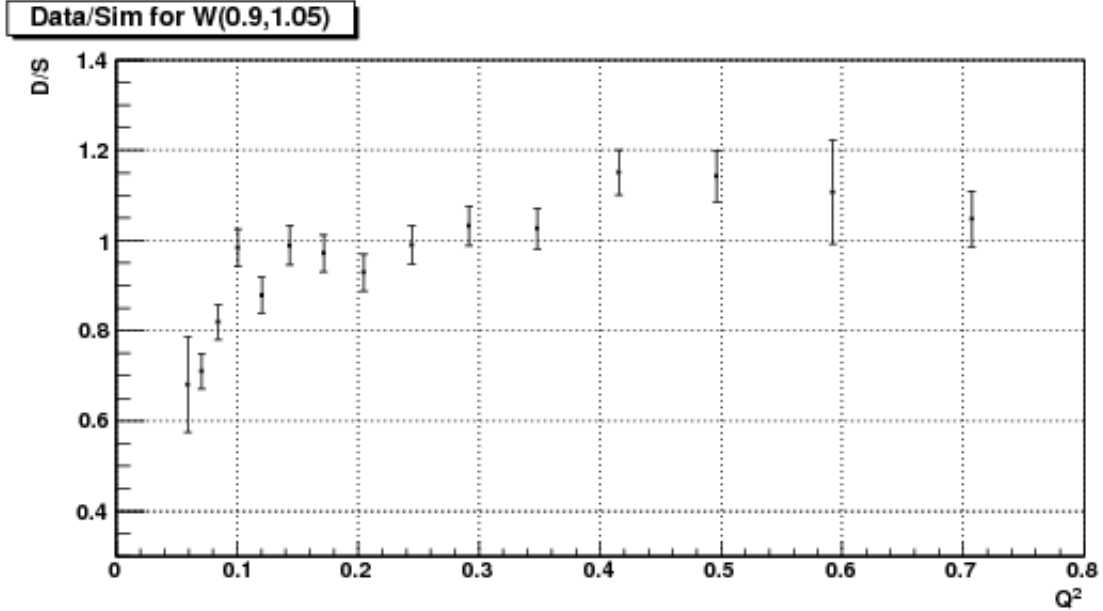
(a) Data/Sim ratio vs θ in 1.3 GeV quasi-elastic data.

Data/Sim for W(1.15,1.3)

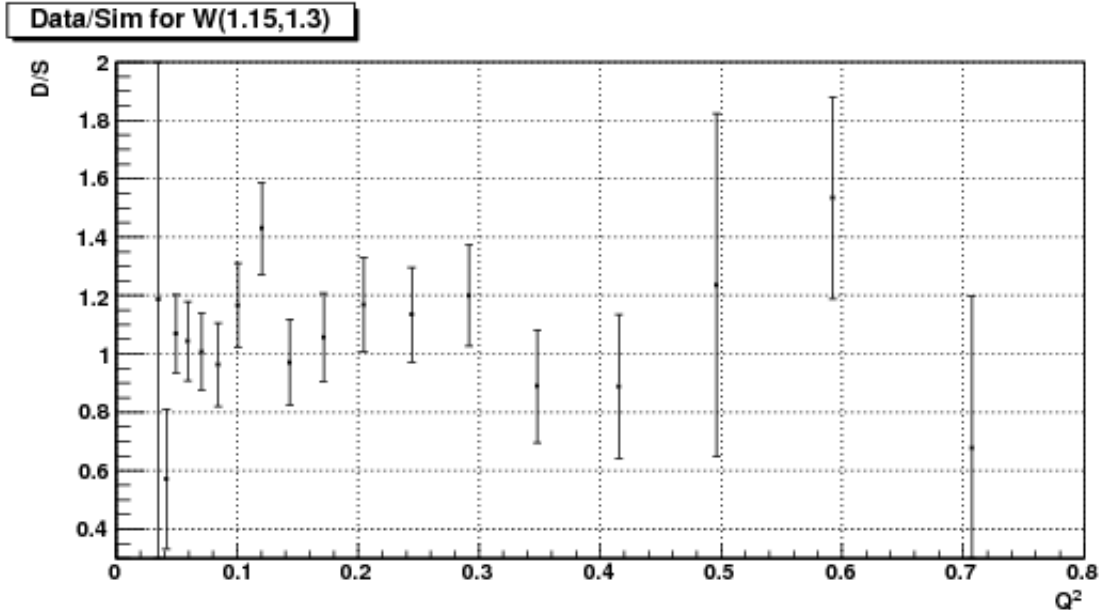


(b) Data/Sim ratio vs θ in Δ -resonance region of 1.3 GeV data.

Figure 4.11: The same data as in Fig. 4.10, but plotted versus average scattering angle (θ).

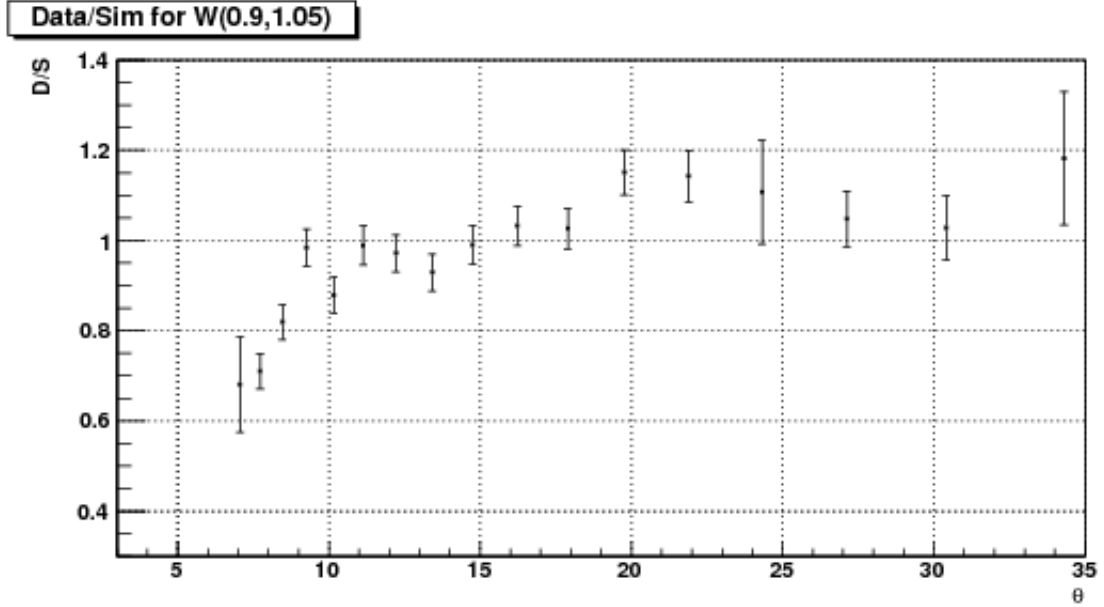


(a) Data/Sim ratio vs Q^2 in 2.0 GeV quasi-elastic data.

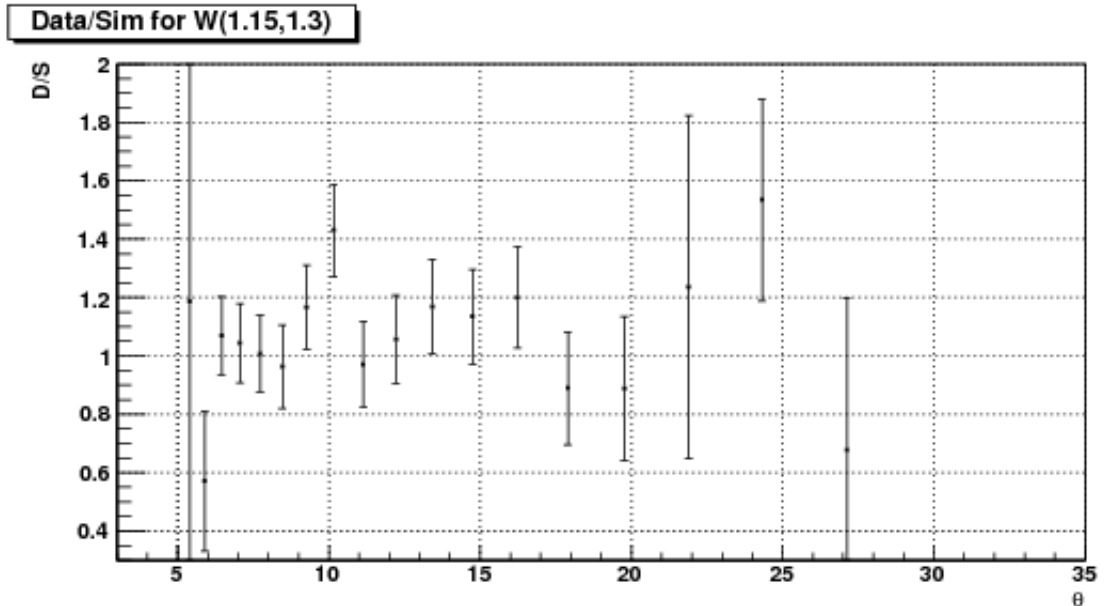


(b) Data/Sim ratio vs Q^2 in Δ -resonance region of 2.0 GeV data.

Figure 4.12: Q^2 dependence of ratios of 2.0 GeV data and simulation in the quasi-elastic and Δ -resonance regions.



(a) Data/Sim ratio vs θ in 2.0 GeV quasi-elastic data.



(b) Data/Sim ratio vs θ in Δ -resonance region of 2.0 GeV data.

Figure 4.13: The same data as in Fig. 4.12, but plotted versus average scattering angle (θ).

1654 4.5 Method to Extract g_1 and $A_1 F_1$

1655 4.5.1 ‘Variation’ of the standard simulation

The whole chain of steps outlined in the previous sections for the standard simulation is repeated with just one major difference: the model input for the asymmetries A_1 for both the proton and the neutron are increased by a constant value⁵ of 0.1. With all other model ingredients being kept constant, this change leads to a change of the spin structure function g_1 that can be straightforwardly calculated for each kinematic bin within the model:

$$\delta g_1(W, Q^2) = \delta A_1 \times F_1 \frac{\nu^2}{\nu^2 + Q^2} \quad (4.5)$$

1656 Correspondingly, the simulated count difference $\Delta n(W, Q^2)$ will change to
 1657 a new value $\Delta n'$. This ‘non-standard’ simulation with $A_1 = A_1(\text{standard}) +$
 1658 0.1 is performed generating an about equal number of Monte-Carlo events.
 1659 The final reconstructed data is then multiplied with the same overall scaling
 1660 factor SF as for the standard simulation and then further (cross-)normalized
 1661 by one additional factor $SF_{ext} = (\sigma_1^p / \sigma_2^p) / (N_1 / N_2)$ to account for the change
 1662 in cross section map and the (slight) difference in the number of the generated
 1663 events between the standard and non-standard simulations. Here, σ_1^p and σ_2^p
 1664 are the total cross sections for the positive $\Delta\sigma$ maps used for the standard and
 1665 non-standard simulations and, N_1 and N_2 are the corresponding numbers of
 1666 generated events. See Fig. (4.14) to see how the polarized count differences
 1667 look (in one particular Q^2 bin) in experimental and simulated data after such
 1668 normalizations (for all other Q^2 bins, see Figs. 4.8 and 4.9).

This change of the simulated $\Delta n(W, Q^2)$ to a new value $\Delta n'$ can be correlated to the increase in g_1 by solving for the two parameters A and B of the linear equation,

$$\Delta n(\text{simul}) = A + B \cdot \delta g_1, \quad (4.6)$$

where $A(W, Q^2)$ is the result for the simulated Δn for the standard set of model inputs i.e., $A(W, Q^2) = \Delta n^{\text{standard}}(W, Q^2)$, and $B(W, Q^2)$ is the proportionality factor representing the change in $\Delta n(\text{sim})$ per unit change in

⁵We arbitrarily chose 0.1 in the inelastic region, but could also have used any other value (not too big, however).

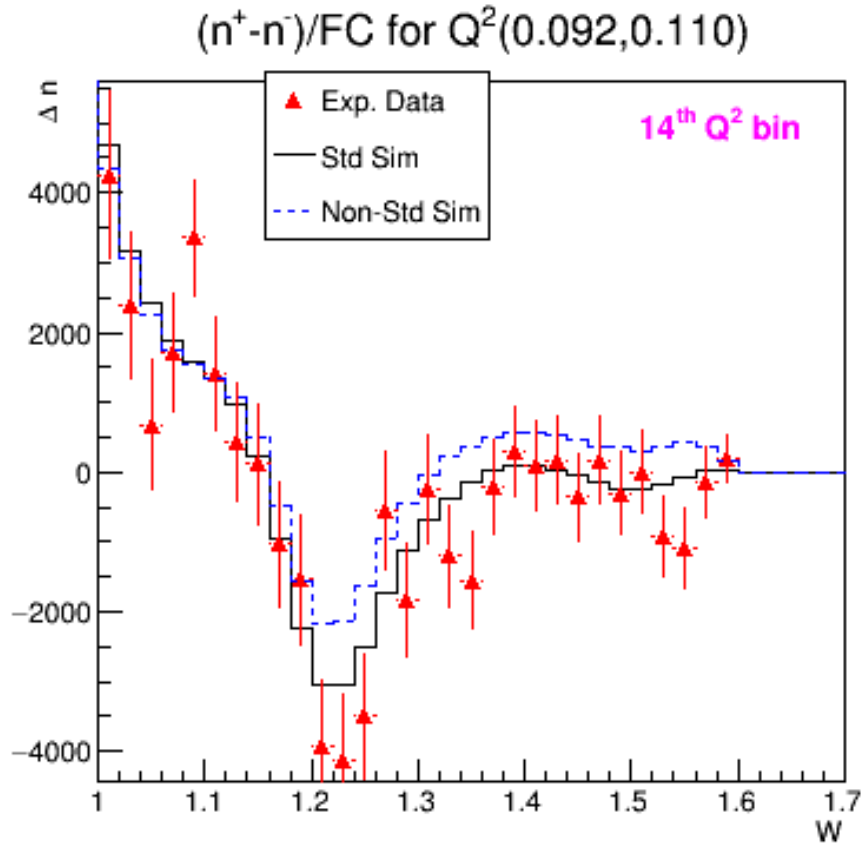
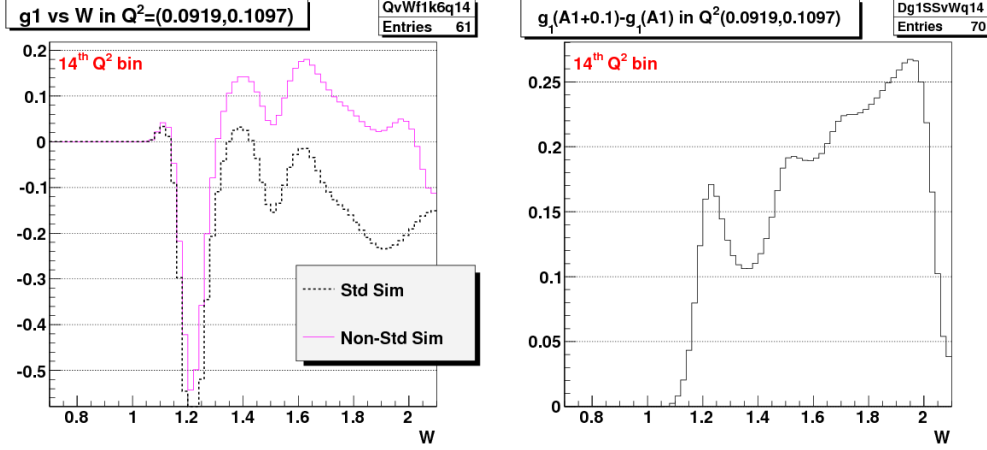


Figure 4.14: Δn of experimental data and two versions of simulations in one particular Q^2 bin for 1.3 GeV case (for data on more Q^2 bins, see Fig. 4.8).

g_1 , as given by:

$$B(W, Q^2) = \frac{\Delta n' - \Delta n}{\delta g_1}. \quad (4.7)$$

The proportionality factor $B(W, Q^2)$ is then determined for each of the kinematic bins (in (W, Q^2)) in which the experimental data has been histogrammed. For this purpose, using the RCSLACPOL program, we produce two values of structure function g_1 in each kinematic bin - one is $g_1^{Standard}$ corresponding to the standard simulation and the other is $g_1^{non-standard}$ corresponding to the non-standard simulation. By dividing the above change in the count difference with the difference Δg_1 of these two structure functions, we get the factor $B(W, Q^2)$ for the bin.



(a) g_1 for standard and non-standard simulation

(b) Difference of the two g_1

Figure 4.15: Plots showing the change in model g_1 due to the change of A_1 to $A_1 + 0.1$.

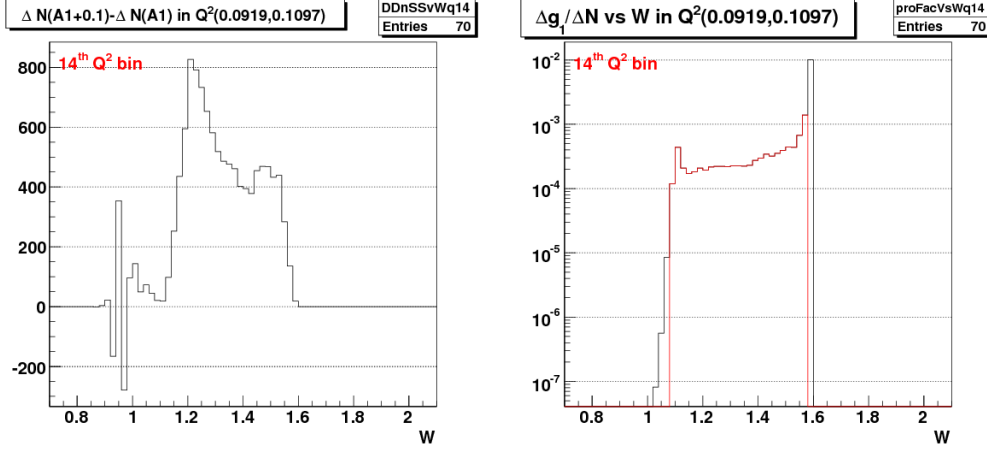
In principle (and ignoring the other enumerated possible sources of disagreement between data and simulation), we can then easily find the “amount of change” δg_1 to be added to the standard model g_1 to get perfect agreement:

$$\delta g_1 = g_1^{extr}(W, Q^2) - g_1^{Standard} = \frac{\Delta n^{data}(W, Q^2) - \Delta n^{standard}(W, Q^2)}{B(W, Q^2)} \quad (4.8)$$

where the values of Δn^{data} and $\Delta n^{standard}$ come from the polarized count differences Δn in the experimental data and the standard simulation respectively (as shown, for example, by the red points and black histograms in Fig. 4.14 for one particular Q^2 bin).

It is also straightforward to propagate the statistical error to the extracted g_1 . The statistical error in this extracted quantity totally comes from the error in the experimental counts Δn^{data} (assuming there is no error in the model quantities involved and also in the simulation counts because we did our simulation with large enough statistics to warrant ignoring the errors) as follows:

$$\sigma(g_1^{extr}(W, Q^2)) = \frac{\sigma(\Delta n^{data}(W, Q^2))}{B(W, Q^2)}. \quad (4.9)$$



(a) Change in $\Delta n(sim)$ simulated count difference i.e. $\Delta N = \Delta n'(A_1 + 0.1) - \Delta n(A_1)$ due to the change of A_1 to $A_1 + 0.1$ (for 1.3 GeV case).

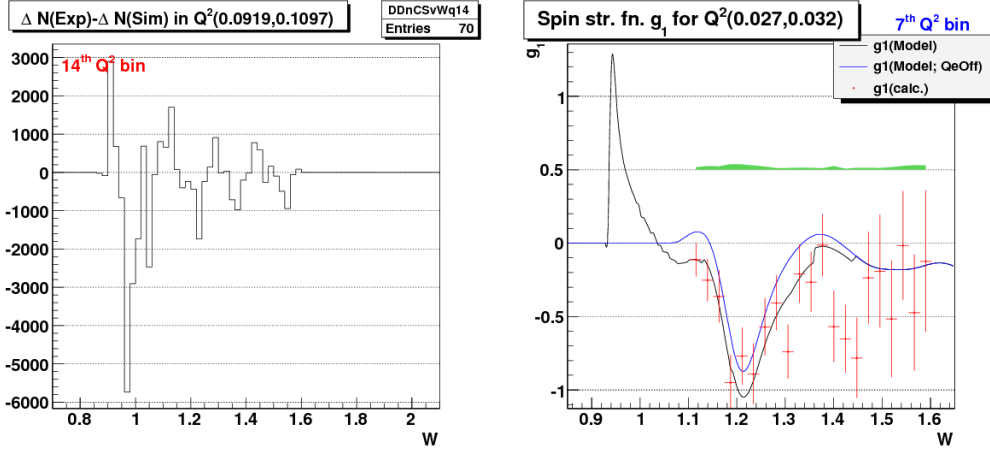
(b) Proportionality factor ($1/B(W, Q^2)$) for 1.3 GeV case. Black is the original values. Red is the ones kept after discarding the first or last few (low statistics bins) that had unreasonably high (suddenly changing) ratios. This ensures we only show final data with “good” proportionality factor.

Figure 4.16: Plots for $\Delta n(sim)$ and the corresponding proportionality factors.

1681 The values of g_1 and its errors thus extracted from 1.3 GeV data for one
 1682 Q^2 bin is shown in Fig. (4.17(b)). Similar results for all the bins from two
 1683 beam energy data sets in different kinematic bins can be seen in Fig. 6.1.

1684 Because we are also interested in measuring the forward spin polarizability
 1685 and the extended GDH integral, we also extract the product $A_1 F_1$ which
 1686 enters these integrals. We followed the exact same procedure for g_1 as out-
 1687 lined above. We determined new proportionality factors in each kinematic
 1688 bin, again using Eq. 4.11 as before but with the denominator replaced, this
 1689 time, with the corresponding change in $A_1 F_1$ (instead of the change in g_1).
 1690 Then we can use the following expression (similar to equation 4.8) to extract
 1691 $A_1 F_1(W, Q^2)$:

$$\delta A_1 F_1 = A_1 F_1^{extr}(W, Q^2) - A_1 F_1^{Standard} = \frac{\Delta n^{data}(W, Q^2) - \Delta n^{standard}(W, Q^2)}{B_{A_1 F_1}(W, Q^2)} \quad (4.10)$$



(a) Difference $\Delta n(\text{data}) - \Delta n(\text{sim})$ (for 1.3 GeV case).

(b) Calculated g_1 from 1.3 GeV data.

Figure 4.17: Plots for $\Delta(\Delta n)$ and the corresponding extracted g_1 . On the left, Δn are the normalized count differences from the experimental and simulated (using 'standard' model) data. On the right, the blue line is that of g_1 when the quasi-elastic part was turned off in the model that was used in simulation. We used $g_1^{\text{extracted}} = g_1^{\text{q.e.Off}} + \delta g_1$ to get the measured g_1 , where δg_1 was derived from the data shown on the left using Eq. 4.8.

where

$$B_{A_1 F_1}(W, Q^2) = \frac{\Delta n' - \Delta n}{\delta A_1 F_1}. \quad (4.11)$$

1692 And, the errors on $A_1 F_1$ can also be dealt in the same way as on g_1 .

₁₆₉₃ **Chapter 5**

₁₆₉₄ **Systematic Uncertainties**

₁₆₉₅ There is always a possibility that the final result(s) produced from any data
₁₆₉₆ analysis will be shifted from the true or ideally expected value(s) because the
₁₆₉₇ final result(s) are derived using the measured, modeled or estimated values
₁₆₉₈ of one or more other input parameters, whose values themselves usually have
₁₆₉₉ some systematic measurement or estimation uncertainties.

₁₇₀₀ The systematic effects due to a particular variable are studied by making a
₁₇₀₁ small change in the variable while holding the others constant, and measuring
₁₇₀₂ by how much the end result(s) changed.

₁₇₀₃ In this analysis, ten sources of systematic uncertainties are studied as
₁₇₀₄ listed below:

- ₁₇₀₅ 1. Possible Uncertainty in the overall scaling factor
- ₁₇₀₆ 2. Effect due to the contaminations from polarized H in the target and
₁₇₀₇ from misidentified π^- in the scattered electrons sample.
- ₁₇₀₈ 3. Potential deviations in the reconstructed kinematics
- ₁₇₀₉ 4. Possible uncertainty in the CC-inefficiency estimation
- ₁₇₁₀ 5. Effect due to the e^+e^- pair symmetric contamination
- ₁₇₁₁ 6. Possible uncertainty in the estimation of radiation lengths
- ₁₇₁₂ 7. Model variation using preliminary version (v1) of A_1 model by Guler/Kuhn
₁₇₁₃ (2008-9)
- ₁₇₁₄ 8. Model variation using old version of A_2 resonance model

1715 9. Model variation of F_2 (and proportionally of F_1) while keeping R con-
1716 stant

1717 10. Model variation of R or F_1 (with F_2 unchanged)

1718 For the ease of description later on, these ten components will be referred to
1719 by the index "k" with its value indicating the position in the list. So, the
1720 uncertainty due to scaling factor will be identified with k=1 and so on.

Possible Uncertainty due to the overall scaling factor This uncer-
tainty is due to the uncertainties in the overall scaling factor (SF), which is a
convolution of various unmeasured constants such as P_bP_t , packing fraction
etc (see Sec. 4.1.1). This contribution is estimated by assuming that the
uncertainties in SF is not more than 10%. Thus considering the worst case
scenario of 10% uncertainty in SF, we estimate the corresponding uncertainty
in g_1 as follows:

$$\Delta g_1^{SF}(W, Q^2) = g_1^{std}(W, Q^2) + \frac{\Delta n^{data}(W, Q^2) - 1.1 \cdot \Delta n^{std}(W, Q^2)}{1.1 \cdot B(W, Q^2)} - g_1^{data}(W, Q^2) \quad (5.1)$$

1721 with "std" shorthand used for "standard" model or the corresponding sim-
1722 ulation i.e. the ones provided by RCSLACPOL when the asymmetry A_1
1723 was not artificially increased to $A_1 + 0.1$. Here, Δn^{data} and Δn^{std} represent
1724 the polarized count differences for the experimental and simulated (without
1725 artificially changing A_1) data respectively.

Uncertainty from Polarized H in target and π^- contaminations This
contribution from polarized H in target and π^- contamination is evaluated as
follows,

$$\Delta g_1^{cont}(W, Q^2) = g_1^{std}(W, Q^2) + \frac{\Delta n^{data}(W, Q^2) \cdot 1.025 - \Delta n^{std}(W, Q^2)}{B(W, Q^2)} - g_1^{data}(W, Q^2) \quad (5.2)$$

1726 where we assume that the contamination is not more than 2.5%, which is
1727 consistent with what was found from our own study of the contamination.

Possible uncertainty in the beam energy measurement This contrib-
ution is evaluated assuming the uncertainty in beam energy measurement

is not more than 10 MeV, so either the experimental data or the standard-simulation data can be analyzed assuming the beam energy was different by 10 MeV. In this analysis, the simulated data was analyzed assuming that the beam energy was 10 MeV more than that used during the event generation or simulation which was the same as that used for analyzing the experimental data. For example, for the lower beam energy data set, 1339 MeV was used to analyze the experimental data as well as to simulate the corresponding data, but during the analysis of the simulated data, the energy value used was 1349 MeV. Here, the change in energy results in changes in both Q^2 and W .

$$\Delta g_1^{Eb}(W, Q^2) = g_1^{std}(W, Q^2) + \frac{\Delta n_{E\bar{b}}^{data}(W, Q^2) - \Delta n_{E\bar{b}+}^{std}(W, Q^2)}{B(W, Q^2)} - g_1^{data}(W, Q^2) \quad (5.3)$$

where $\Delta n_{E\bar{b}+}^{std}$ is now the simulated Δn^{std} obtained by analyzing the data from the standard simulation as usual but with a beam energy that was 10 MeV more than the standard value.

Possible uncertainty in the CC-inefficiency estimation This contribution is estimated by assuming a maximum of 50% uncertainty in the estimated inefficiency as follows: The the 50% error is justified because the uncertainty in inefficiency is no more than 50% for nphe<2.5 (see Fig. 3.30).

$$\Delta g_1^{Eb}(W, Q^2) = g_1^{std}(W, Q^2) + \frac{\Delta n_{0.5CCi}^{data}(W, Q^2) - \Delta n_{0.5CCi}^{std}(W, Q^2)}{B(W, Q^2)} - g_1^{data}(W, Q^2) \quad (5.4)$$

where $\Delta n_{0.5CCi}^{std}$ is now the simulated Δn^{std} obtained after applying 50% more inefficiency instead of the actually estimated value.

Possible uncertainty due to e^+e^- pair symmetric contamination The contribution due to e^+e^- pair symmetric contamination is calculated as follows:

$$\Delta g_1^{Eb}(W, Q^2) = g_1^{std} + \frac{\Delta n^{data} \cdot \frac{1}{1+f(e^+e^-)} - \Delta n^{std}}{B(W, Q^2)} - g_1^{data}(W, Q^2) \quad (5.5)$$

where $f(e^+e^-)$ is the fraction of electrons in a given bin that come from pair-symmetric e^+e^- produced as estimated with EG1b fit by N. Guler [22] (used the closest available energies).

Radiative correction uncertainty Here, we need to change the parameter that most influences radiative corrections, the number of radiation lengths before (RADB) and after (RADA) the scattering. By increasing both numbers by 10%, we should have a safe upper limit on practically all uncertainties coming from the radiative procedure itself. But, to simplify the situation, we increased the RADA parameter in RCSLACPOL by 20% and repeated the full-statistic simulation. As a result the simulated count difference in each kinematic bin changed from Δn^{std} to a new value Δn^{rad} . This change can be converted to the corresponding inferred change in g_1 by using the same proportionality factors $B(W, Q^2)$ as used earlier in the g_1 (or $A_1 F_1$) extraction/calculation. In other words, for a given kinematic bin this particular contribution to the systematic uncertainty is calculated as:

$$\Delta g_1^{rad}(W, Q^2) = g_1^{std} + \frac{\Delta n^{data}(W, Q^2) - \Delta n^{rad}(W, Q^2)}{B(W, Q^2)} - g_1^{data}(W, Q^2) \quad (5.6)$$

1736 where the proportionality factor $B(W, Q^2)$ for the bin is exactly the same as
1737 that used to calculate g_1 earlier.

1738 5.1 Model uncertainties

1739 The remaining four components in the total systematic uncertainty (the last
1740 four in the list ??) account for the model uncertainty contributions. For
1741 this purpose, we changed the values of two of the model parameters “Asym-
1742 Choice” and “SFchoice” (each takes value of 11, in the standard case)

1743 We repeated the full statistics simulation four more times by changing
1744 the values of two RCSLACPOL parameters “AsymChoice” and “SFchoice”
1745 (which controls the values of model asymmetries and the structure functions,
1746 with each taking a value of 11 in the standard case) one by one corresponding
1747 to the following four model variations:

- 1748 1. Variation-1: AsymChoice=12, SFchoic=11
- 1749 2. Variation-2: AsymChoice=15, SFchoic=11
- 1750 3. Variation-3: AsymChoice=11, SFchoic=12
- 1751 4. Variation-4: AsymChoice=11, SFchoic=13

1752 where, the different values of the two RCSLACPOL parameters correspond
1753 to the following model choices:

1754 1. **AsymChoice** values are used to determine specific A_1/A_2 models used
1755 in the RCSLACPOL program

- 1756 (a) 11: Standard Resonance Model 2008-9 Guler/Kuhn (**Used for**
1757 **standard simulation**)
1758 (b) 12: Variation of A_1 model (earlier fit)
1759 (c) 15: Variation of A_2 resonance model: Vary the virtual photon
1760 asymmetry A_2 in the resonance region within its fit uncertainties.

1761 2. **SFchoice** values are used to determine specific F_1/F_2 models.

- 1762 (a) 11: 2009 version of $F_1^n/F_1^p/F_1^d$ by Peter Bosted/Eric Christie 2009,
1763 HERMES (**Used for standard simulation**) (with d in F_1^d de-
1764 noting a deuteron).
1765 (b) 12: Same version as 11, but with fit uncertainties added to F_2
1766 (and proportionally F_1)
1767 (c) 13: Same version as 11, but with fit uncertainties subtracted from
1768 R (F_2 unchanged)

After the simulation data for the above four cases were available, four more data tables (TM1,TM2,TM3 and TM4) were produced for the corresponding model values of g_1 , A_1 , F_1 etc. Then, the contributions to the systematic uncertainty from each of these four cases of model variation were given as follows:

$$\Delta g_1^i(W, Q^2) = g_1^{std}(W, Q^2) - g_1^i(W, Q^2) + \frac{\Delta n^i(W, Q^2) - \Delta n^{std}(W, Q^2)}{B(W, Q^2)} \quad (5.7)$$

1769 with “i” indicating any of the four cases of model variation, g_1^i being the
1770 model prediction for the i^{th} case as obtained from the corresponding data
1771 table “TMi” and the proportionality factor $B(W, Q^2)$ again being exactly
1772 the same as used to calculate g_1 as earlier.

5.2 Combining uncertainties

Contributions from the 10 individual components are estimated and then a total contribution is estimated by first combining the corresponding individual components for each of the two beam energies and finally combining them all by calculating the RMS of the ten combined contributions.

5.2.1 Combining uncertainties from the two beam energies

In principle, each of the individual contributions to the systematic uncertainty can also be combined using the same equations as for combining g_1 and $A_1 F_1$ (see above). However, we must be careful to distinguish between correlated and uncorrelated uncertainties. If for a given (W, Q^2) bin, data is available only from one beam energy, then combined uncertainty for the k^{th} component is simply the uncertainty from that beam energy. If there are measurements from both beam energies, we combine them with statistical weights as follows:

1. The variations due to scale factor ($k=1$), beam energy ($k=3$) and CC-efficiency ($k=4$) are all un-correlated and, therefore, added in quadrature as follows:

$$\delta g_1(k=8,10,11, \text{ combined}) = \sqrt{\left(\sum_i \frac{(\delta g_1)^2(i)}{(\Delta g_1)^2(i)} \right) / \text{Sum2}} \quad (5.8)$$

where, δ represents the k^{th} component of the systematic uncertainty, whereas, 'Sum2', 'i' and Δ have the same meanings as before.

2. while all other variations are correlated between the two beam energies and should be averaged linearly (WITH sign):

$$\delta g_1(\text{other } k, \text{ combined}) = \left(\sum_i \frac{(\delta g_1)(i)}{(\Delta g_1)^2(i)} \right) / \text{Sum2} \quad (5.9)$$

with

$$\text{Sum2} = \sum_i \frac{1}{(\Delta g_1)^2(i)} \quad (5.10)$$

1796 providing the statistical weight, where the index 'i' represents two beam en-
 1797 ergy (1.3 and 2.0 GeV) data sets, and Δg_1 indicates the statistical uncertainty
 1798 in g_1 in the corresponding kinematic bin.

1799 **5.2.2 Combining uncertainties from the ten sources**

1800 Once each of the k^{th} component of the systematic uncertainties are combined
 1801 between the two beam energies, we then proceed to combine them all to get
 1802 a grand total. This is done by simply adding the ten E_b -combined systematic
 1803 uncertainties in quadrature and taking the square-root of the sum as follows:

$$TotalSystematicUncertainty = \sqrt{\sum_{k=1}^{10} (\Delta g_1)_k^2} \quad (5.11)$$

1804 Figs. (5.2 and 5.3) show, for example, the different components of the
 1805 systematic uncertainties (along with the grand total) on g_1 (from 1.3 GeV
 1806 data) evaluated in the manner just outlined. Likewise, Figs. (5.4 and 5.5)
 1807 show similar plots for the 2.0 GeV data.

1808 These ten different components of systematic uncertainties on g_1 (and
 1809 similarly on $A_1 F_1$) thus calculated separately for both beam energies are
 1810 later combined as follows:

1811 **5.2.3 Combining data from the two beam energies**

1812 Once the data g_1 and $A_1 F_1$ and their corresponding uncertainties are eval-
 1813 uated from each beam energy data set, they are combined as follows [29] (to
 1814 make the description simple, the procedure is described only for g_1 , but, in
 1815 the end, the exact same procedure is followed for $A_1 F_1$ as well):

- 1816 1. First a table is made, separately for each beam energy, of all (Q^2, W)
 1817 bins with with calculated values of g_1 , their statistical uncertainties and
 1818 each of the ten components of the systematic uncertainties (making sure
 1819 to keep the correct signs of the systematic changes) in separate columns
 1820 (one row is for one bin in (Q^2, W)).
- 1821 2. Then another table is made for the combined values of g_1 , which are
 1822 evaluated as follows:

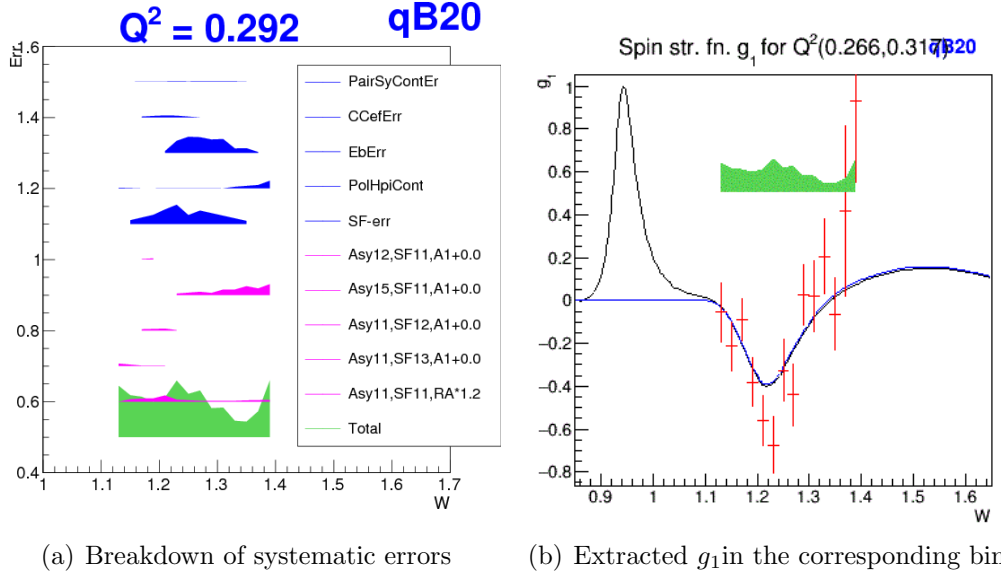


Figure 5.1: Various components of systematic uncertainty (see Secs. 5 and 5) on g_1 plotted against W in a Q^2 bin (1.3 GeV data). The band width represents the size of the uncertainties. The vertical position of each band has no physical meaning (arbitrarily chosen for the convenience of display). The first five (blue) bands are the contributions due to e^+e^- -contamination (see Sec. 5), CC-inefficiency (see Sec. 5), uncertainties in beam energy measurement (see Sec. 5), polarized background (H, π^- etc - see Sec. 5) and scaling factor uncertainties (see Sec. 4.1.1) respectively. The first (top) magenta band is the contribution due to the uncertainties in the radiative corrections (see Sec. 5), next four (magenta) are due to model uncertainties (see Sec. 5.1) and the last (green) one is the total uncertainty after properly combining all components. For similar plots in other Q^2 bins see Figs. 5.2 and 5.3.

- 1823 (a) If for a given (W, Q^2) bin, g_1 comes only from one beam energy,
1824 then all the entries from that energy go into the "combined" table
1825 (b) If g_1 has measurements from both beam energies, we combine

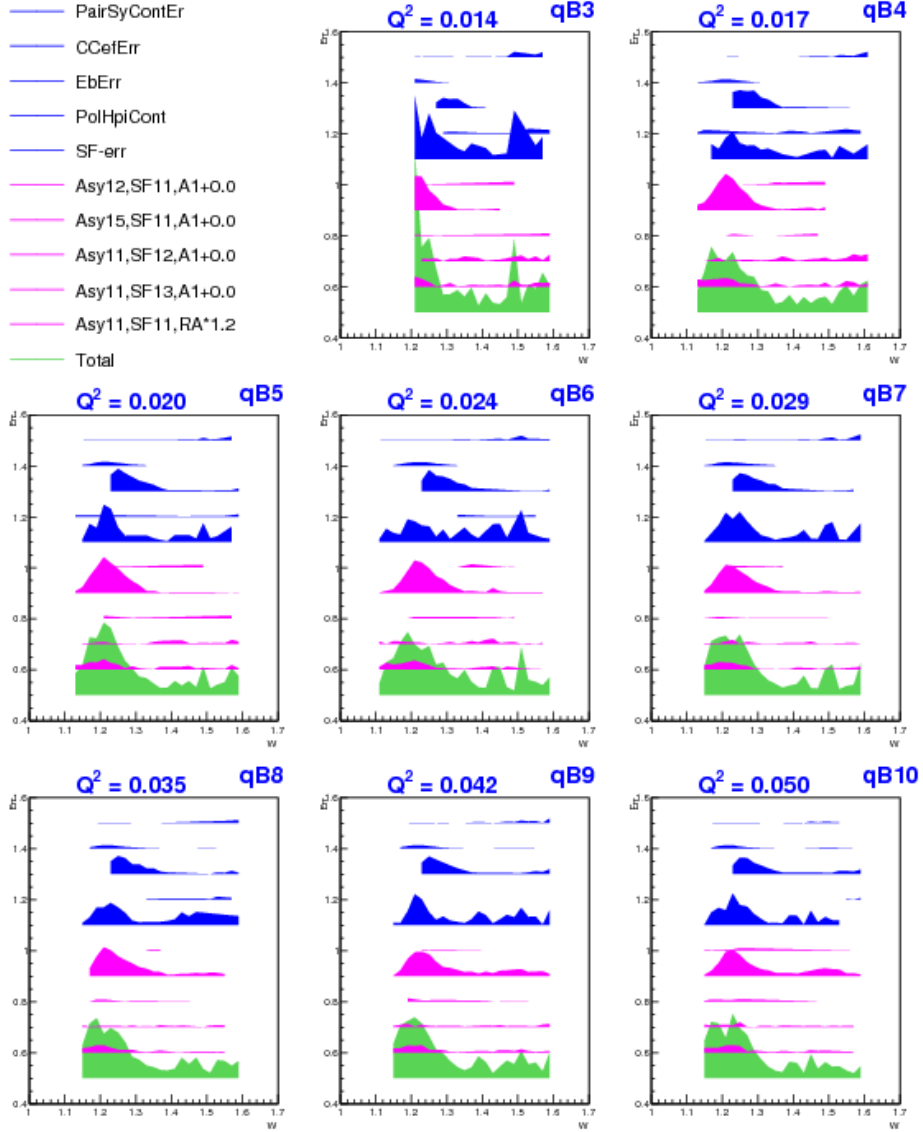


Figure 5.2: Plots like that shown in Fig. 5.1 showing various components of systematic uncertainty on g_1 plotted against W in different Q^2 bins for 1.3 GeV data.

them with statistical weights as follows:

$$Sum1 = \sum_i \frac{g_1(i)}{(\Delta g_1)^2(i)} \quad (5.12)$$

$$Sum2 = \sum_i \frac{1}{(\Delta g_1)^2(i)} \quad (5.13)$$

$$g_1(\text{combined}) = Sum1 / Sum2 \quad (5.14)$$

$$\sigma g_1(\text{combined}) = \sqrt{1/Sum2} \quad (5.15)$$

1827 where the index 'i' represents two beam energy (1.3 and 2.0 GeV)
 1828 data sets. and Δg_1 indicates the statistical uncertainty in g_1 .

1829 3. In principle, each of the individual contributions to the systematic un-
 1830 certainty can also be combined using the same equations. However,
 1831 we must be careful to distinguish between correlated and uncorrelated
 1832 uncertainties.

1833 (a) The variations due to scale factor ($k=1$), beam energy ($k=3$) and
 1834 CC-efficiency ($k=4$) are all un-correlated and, therefore, added in
 1835 quadrature as follows:

$$\delta g_1(k=8,10,11, \text{combined}) = \sqrt{\left(\sum_i \frac{(\delta g_1)^2(i)}{(\Delta g_1)^2(i)} \right) / \text{Sum2}} \quad (5.16)$$

1836 where, δ represents the k^{th} component of the systematic uncer-
 1837 tainty, whereas, 'Sum2', 'i' and Δ have the same meanings as
 1838 before.

1839 (b) while all other variations are correlated between the two beam
 1840 energies and should be averaged linearly (WITH sign):

$$\delta g_1(\text{other } k, \text{combined}) = \left(\sum_i \frac{(\delta g_1)(i)}{(\Delta g_1)^2(i)} \right) / \text{Sum2} \quad (5.17)$$

1841 4. Once each of the k^{th} component of the systematic uncertainties are
 1842 combined between the two beam energies, we then proceed to combine
 1843 them all to get a grand total. This is done by simply adding the
 1844 ten combined systematic uncertainties in quadrature and taking the
 1845 square-root of the sum.

1846 The figures 5.6 and 5.8 show the breakdown of the total contribution to
 1847 the systematic uncertainty from different sources. We can see that the dom-
 1848 inant contribution comes from the uncertainties in the overall scale factor
 1849 (the cyan band indicated with SF-err in the legend) which is used to normal-
 1850 ize the simulated data to make them comparable with data. One of the big
 1851 part of this uncertainty comes from those in $P_b P_t$ and target size measure-
 1852 ments. Next big contributions seem to come from the model (in particular

1853 the model for the unmeasured A_2) and radiative corrections. Near the Δ -
1854 resonance region, the effect of beam energy uncertainty also seems to be very
1855 pronounced. The breakdown of the different components (but combined be-
1856 tween the two beam energies) of the total systematic uncertainties are also
1857 shown separately in the figures 5.6 and 5.8

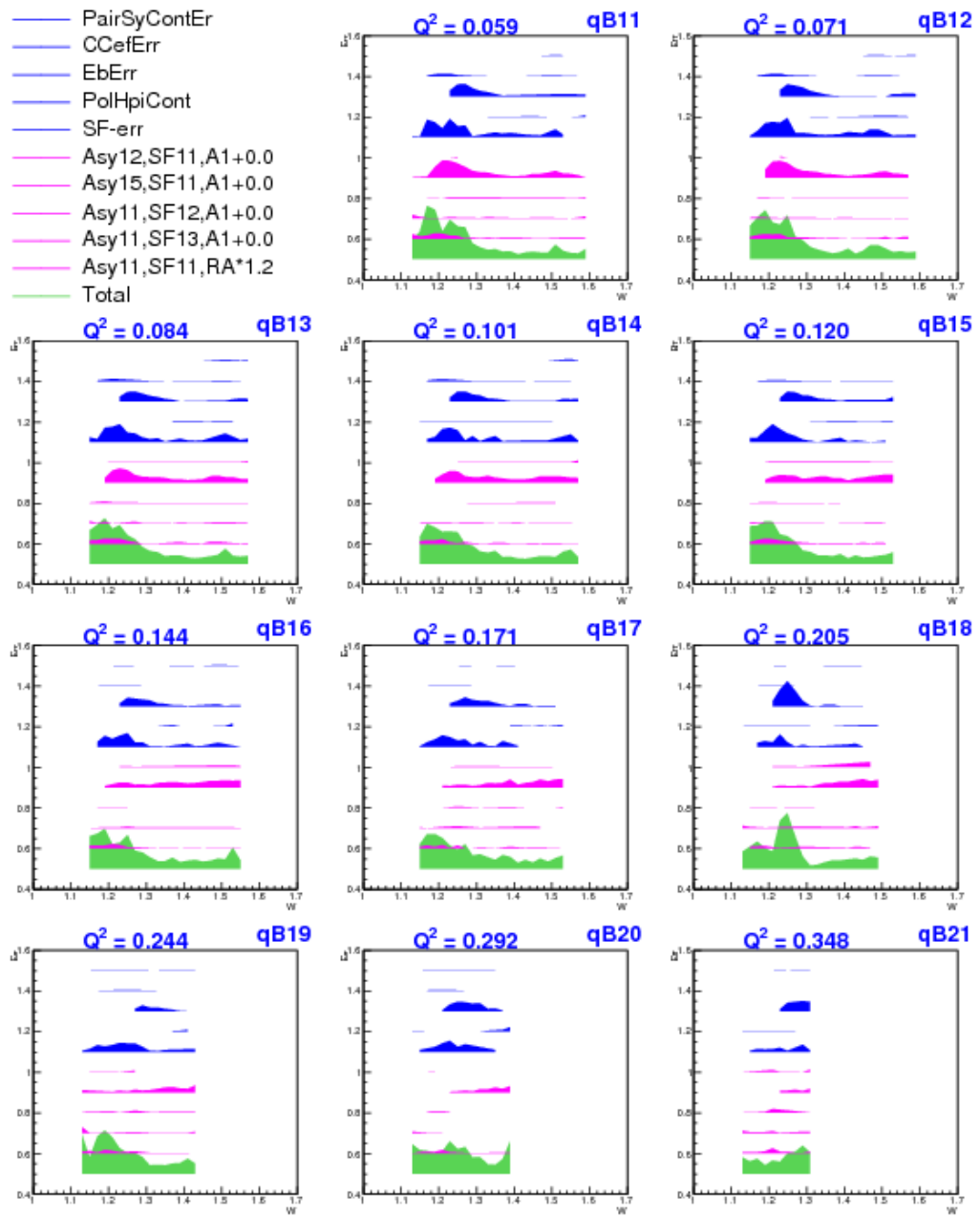


Figure 5.3: Systematic uncertainty components in remaining Q^2 bins (continuation of Fig. 5.2).

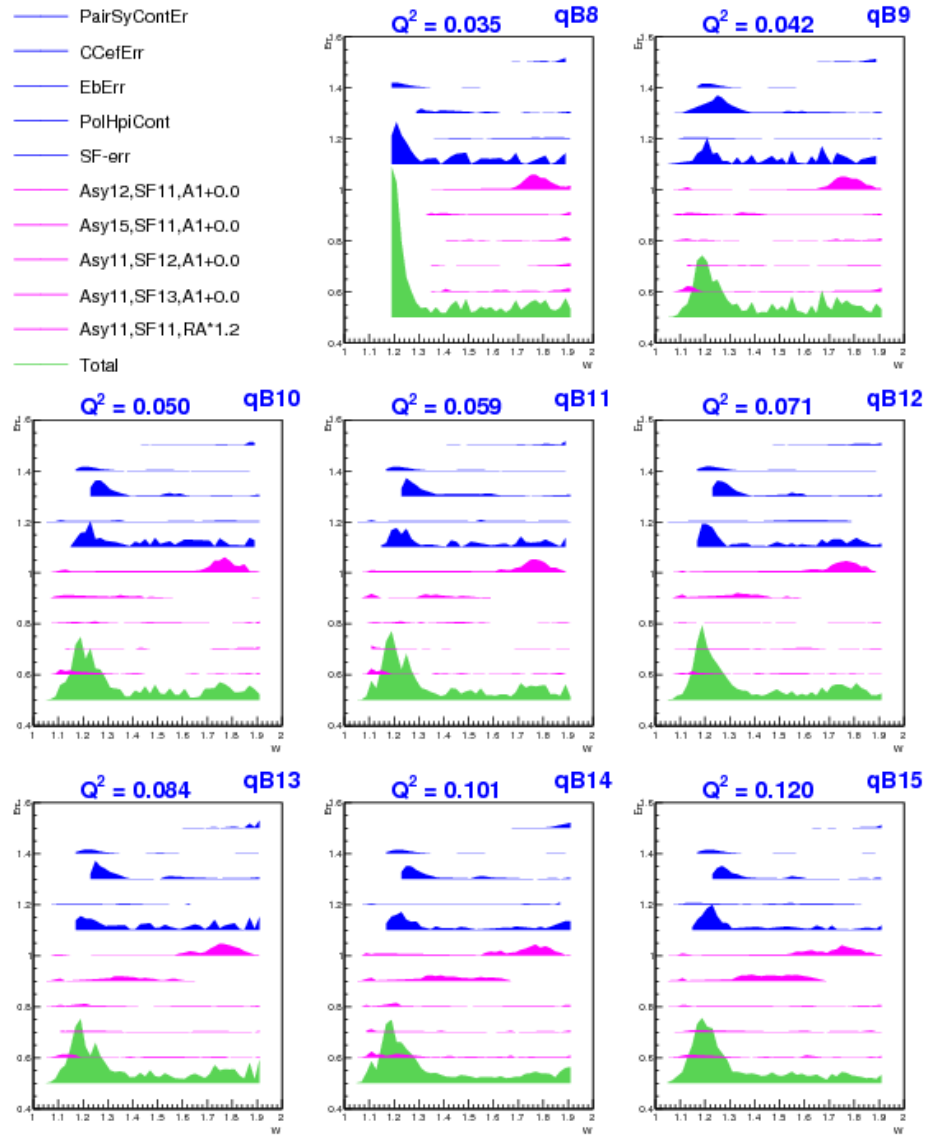


Figure 5.4: Plots similar to those shown in Fig. 5.2 but for 2.0 GeV, showing various components of systematic uncertainty on g_1 plotted against W in different Q^2 bins.

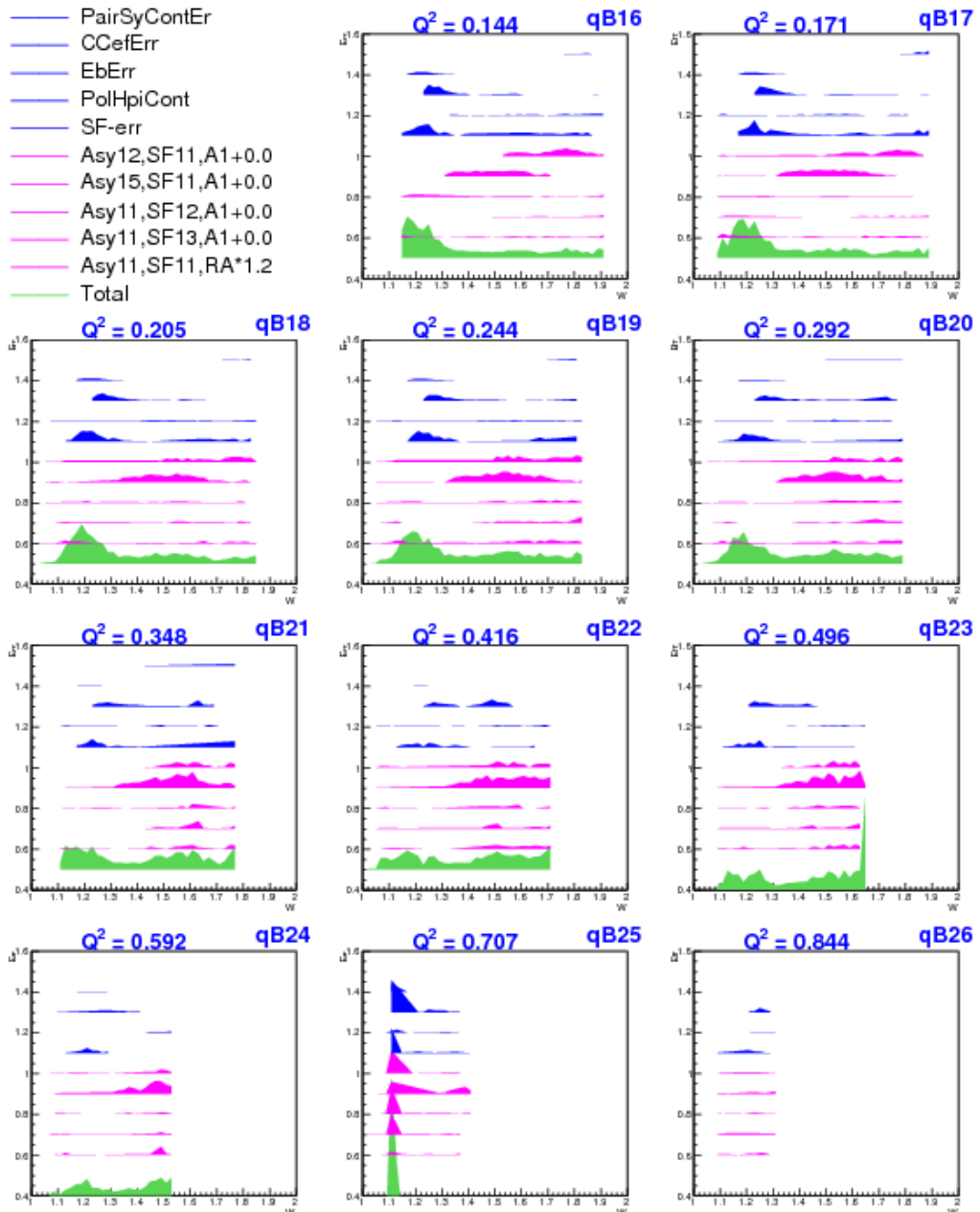


Figure 5.5: Systematic uncertainty components in remaining Q^2 bins (continuation of Fig. 5.4).

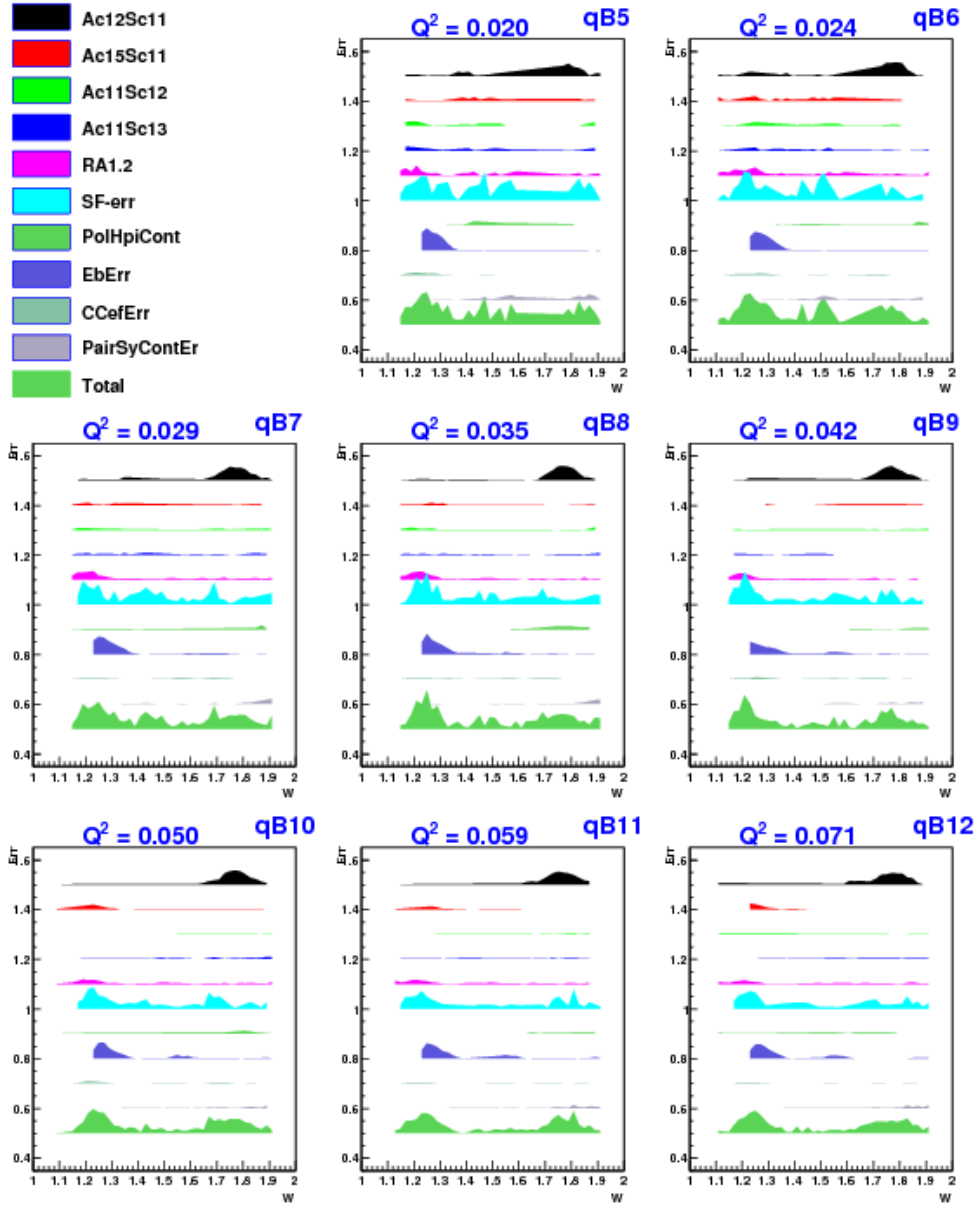


Figure 5.6: Breakdown of systematic uncertainties in g_1 (after combining data from the two energy data sets) in the first few Q^2 bins. See Fig. 5.1 for the description of the different systematic uncertainty components.

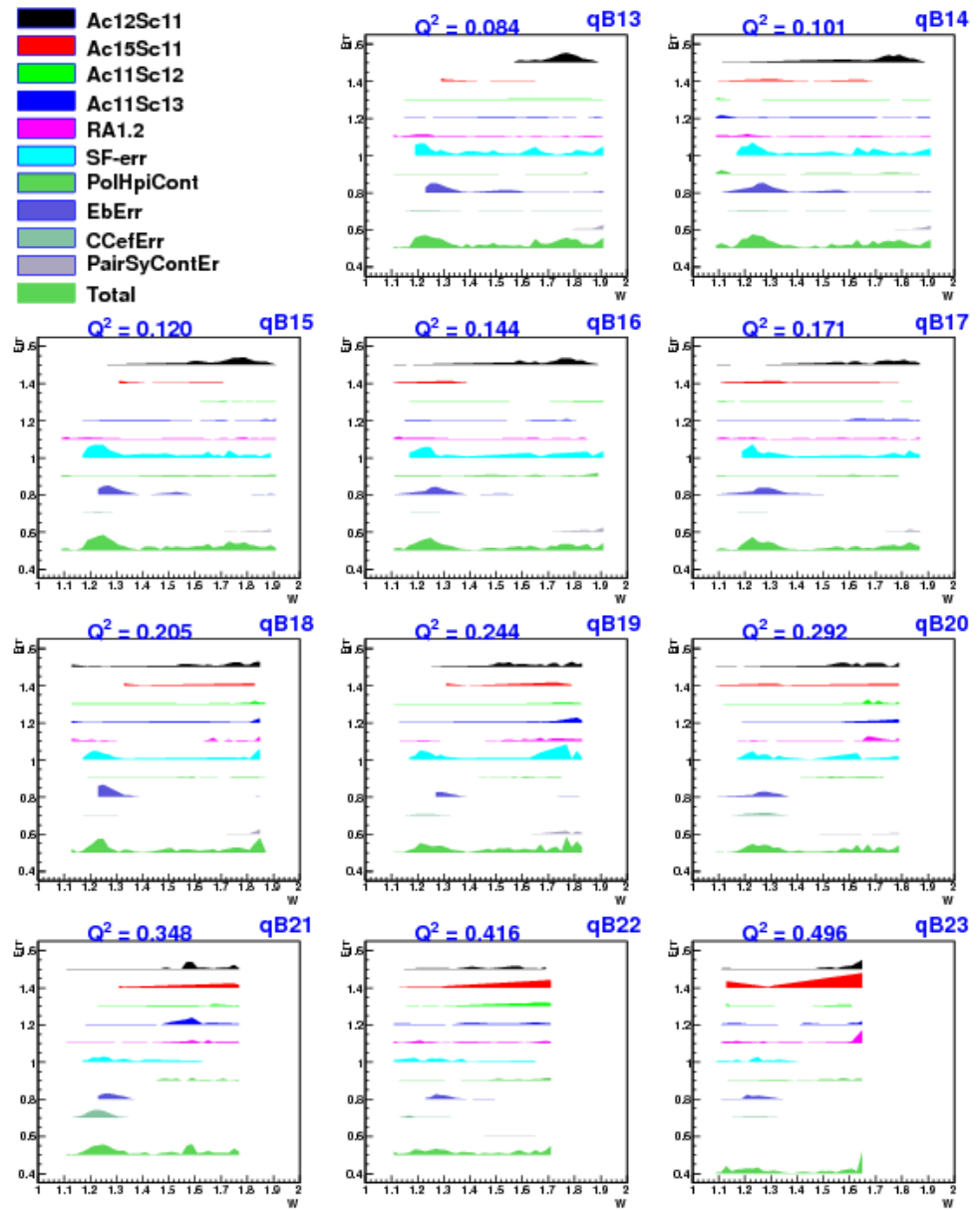


Figure 5.7: Plots as in Fig. 5.6 but in the remaining higher Q^2 bins.

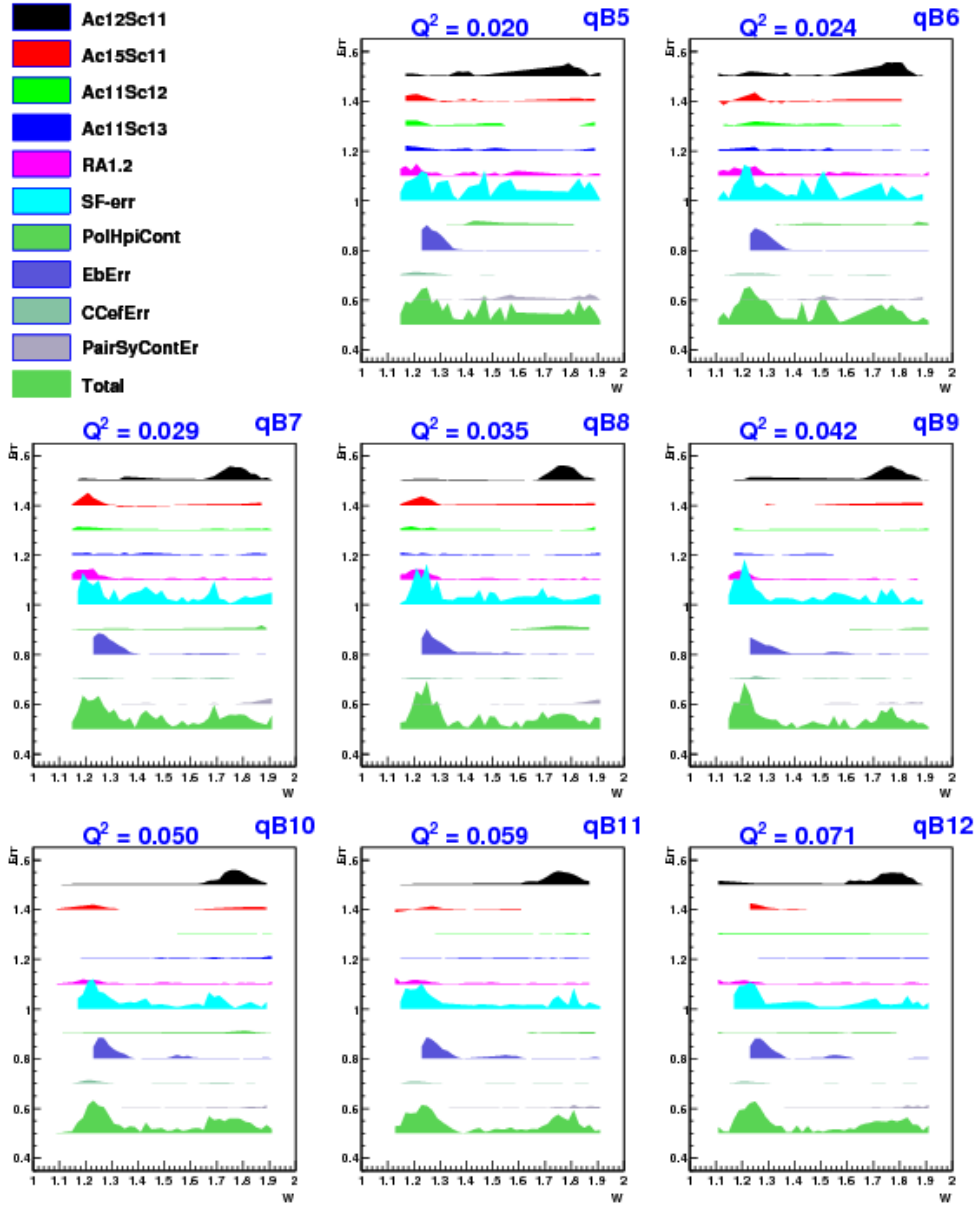


Figure 5.8: Breakdown of systematic uncertainties in $A_1 F_1$ (after combining data from the two energy data sets) in the first few Q^2 bins. See Fig. 5.1 for the description of the different systematic uncertainty components.

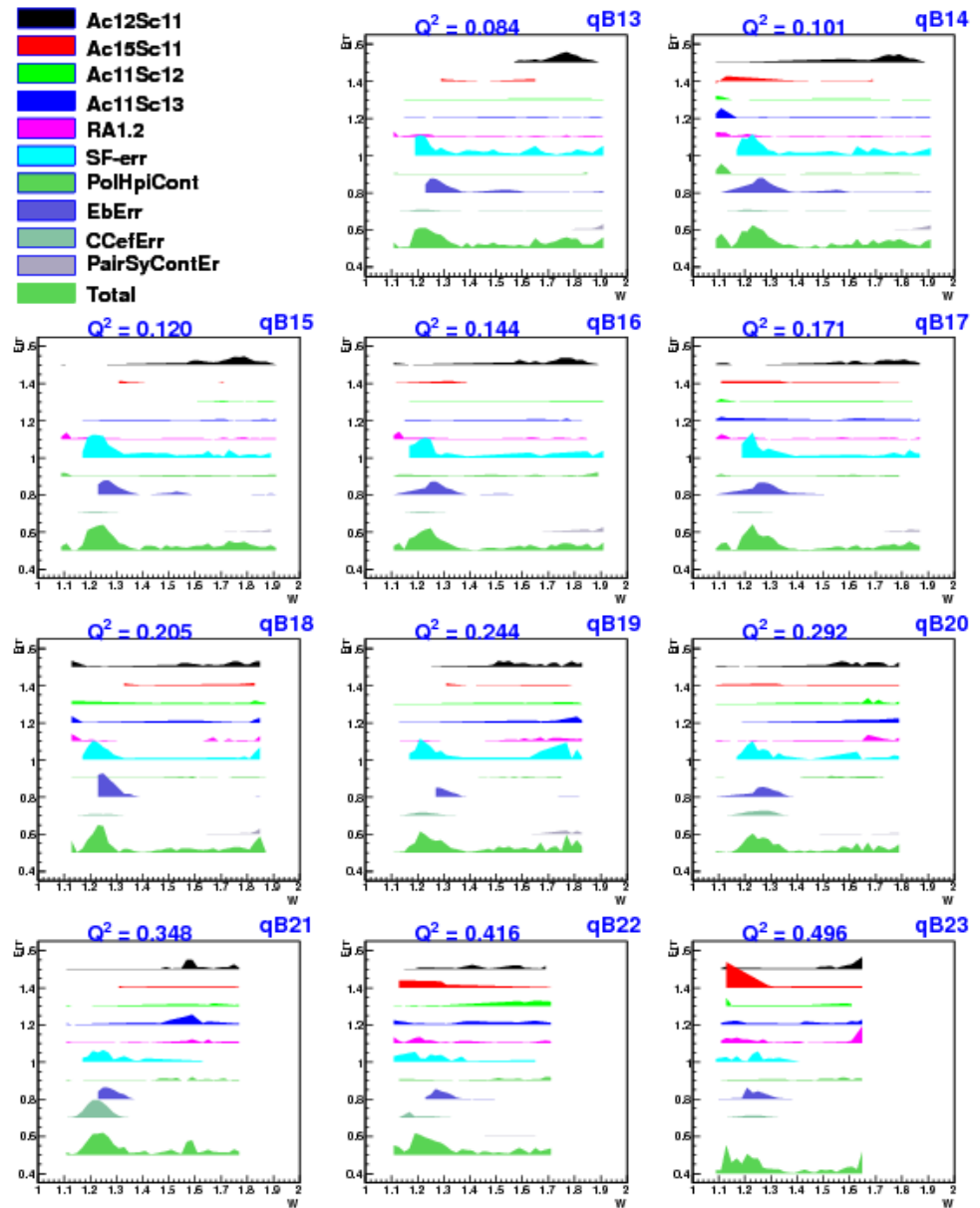


Figure 5.9: Plots as in Fig. 5.8 but in the remaining higher Q^2 bins.

1858 **Chapter 6**

1859 **Results**

1860 Two quantities - g_1 and $A_1 F_1$ and their uncertainties were extracted from the
1861 EG4 deuteron target data using the methods outlined in the previous chapter.
1862 This was done in each of 21 Q^2 bins (between about 0.02 and 0.7 GeV 2 in
1863 Q^2) and several W bins of size 20 MeV each. In the overlapping kinematic
1864 bins where both beam energy data sets contributed, the results were further
1865 combined individually to arrive at a single set of energy independent data
1866 points. Finally, within each Q^2 bin, the newly extracted g_1 and $A_1 F_1$ values
1867 were used to evaluate three different integrals - Γ_1^d , \bar{I}_{TT} , and γ_0^d . All of these
1868 results are presented in the sections below.

1869 **6.1 Extracted g_1 and $A_1 F_1$**

1870 Figures 6.1 and 6.2 show the extracted values of g_1 and their errors from
1871 two different beam energies (1.337 GeV and 1.989 GeV). It can be seen that
1872 the two energies give results that are in good agreement (in the overlapping
1873 kinematic regions).

1874 These results from low Q^2 measurements clearly show the resonant struc-
1875 ture in the region $W \leq 2.0$. Especially, the Δ -resonance stands out through
1876 its strongly negative signal. In addition, in the second resonance region
1877 around $W=1.5$ GeV where $N^*(1520)$ and $N^*(1535)$ (also denoted by D_{11}
1878 and S_{13} respectively) overlap, we see a drastic transition of g_1 (or cross sec-
1879 tion) from strongly negative values (not well described by the model because
1880 it is unconstrained there due to the lack of experimental data) at low Q^2
1881 to clearly positive values at high Q^2 indicating that the dominance of the

1882 spin-flip helicity amplitude $A_{\frac{3}{2}}^T$ on cross section drastically diminishes with
1883 Q^2 and the non-flip amplitude $A_{\frac{1}{2}}^T$ becomes stronger¹. We have pushed the
1884 lower limit on Q^2 in the resonance region with reduced systematic and sta-
1885 tistical errors that will contribute greatly to the world data set. Our data
1886 will help MAID and other phenomenological models to better constrain their
1887 parameters enabling them to make better predictions in the future.

¹The four virtual photoabsorption cross sections σ_T , σ_L , σ_{LT} , and σ_{TT} , are related to the four structure functions F_1 , F_2 , g_1 and g_2 of the target and as a result, g_1 can be expressed as $g_1 = \frac{MK}{8\pi^2\alpha(1+\gamma^2)}(\sigma_{\frac{1}{2}}^T - \sigma_{\frac{3}{2}}^T + 2\gamma\sigma_{LT})$

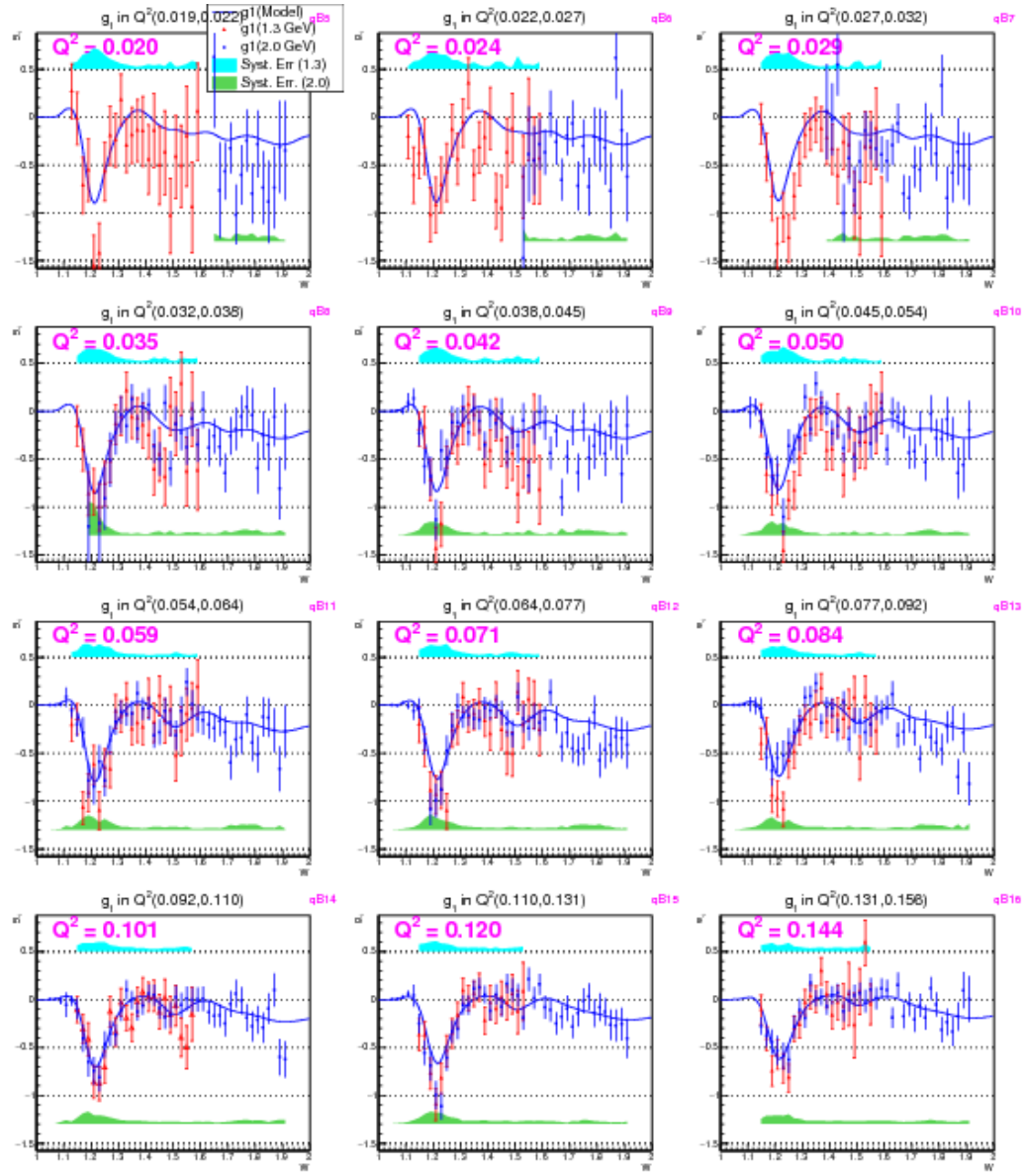


Figure 6.1: Extracted g_1 for deuteron (in the first 12 Q^2 bins) from the two different beam energy data sets. The statistical errors are indicated by error bars, while the systematic uncertainties are given by the bands (cyan, top: 1.3 GeV and green, bottom: 2 GeV).

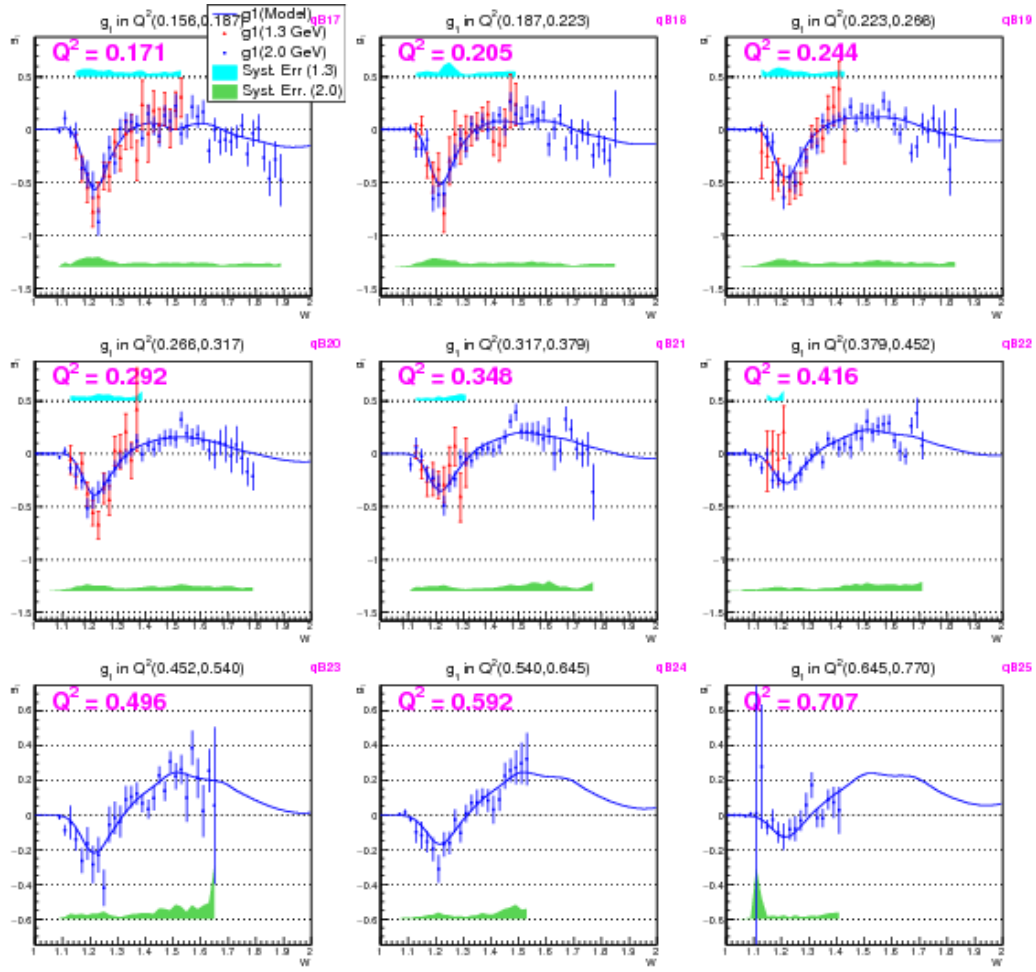


Figure 6.2: Extracted g_1 for deuteron (in the last 9 Q^2 bins (see Fig. 6.1 for the first 12 bins)) from the two different beam energy data sets.

1888 Likewise, Figs. 6.3 and 6.4 shows the extracted values of $A_1 F_1$ and their
 1889 errors from two different beam energies (1.337 GeV and 1.989 GeV). These
 1890 values also show similar behavior as g_1 .

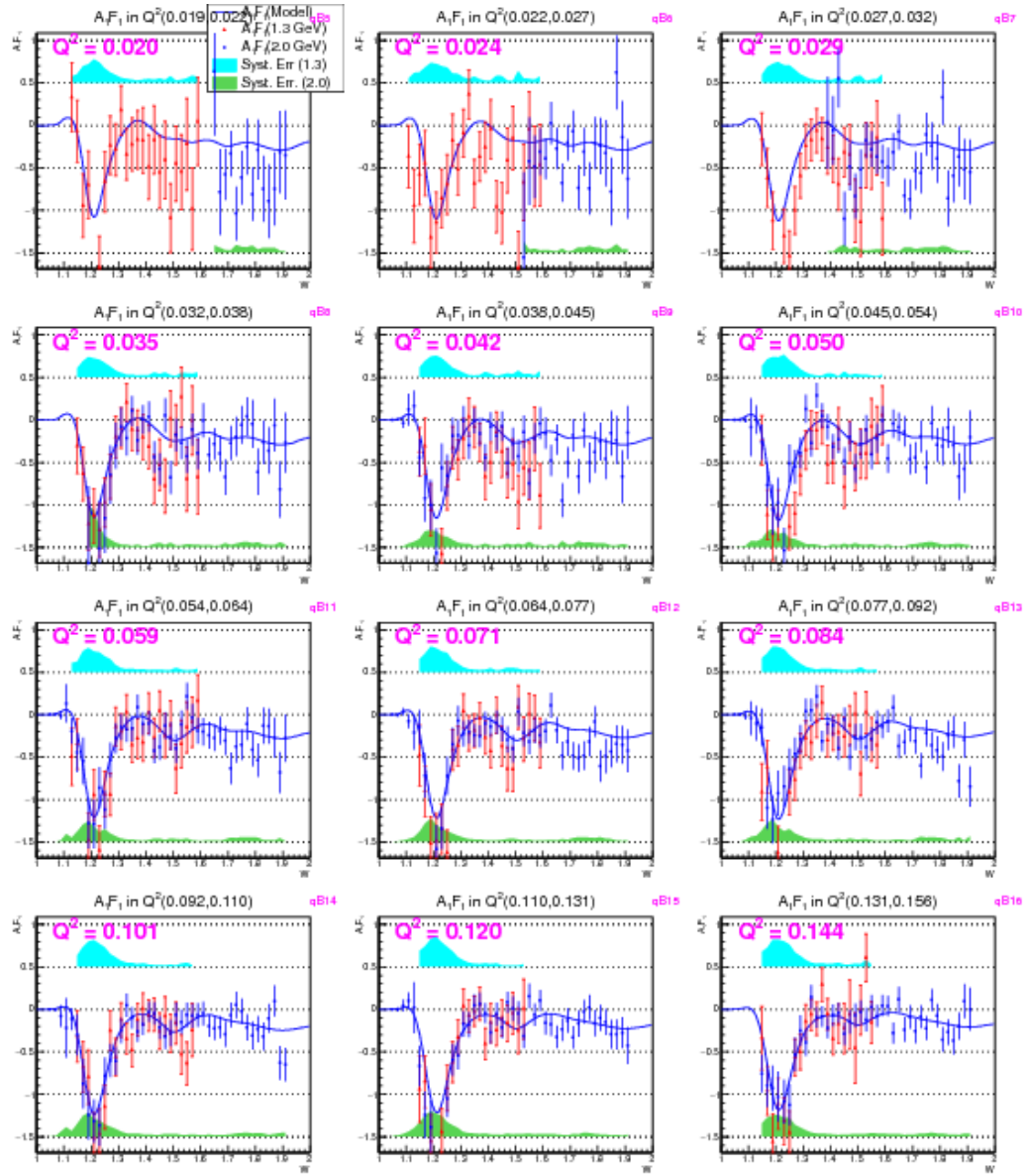


Figure 6.3: Extracted $A_1 F_1$ for deuteron (in the first 12 Q^2 bins) from the two different beam energy data sets. The statistical errors are indicated by error bars, while the systematic uncertainties are given by the bands (cyan, top: 1.3 GeV and green, bottom: 2 GeV).

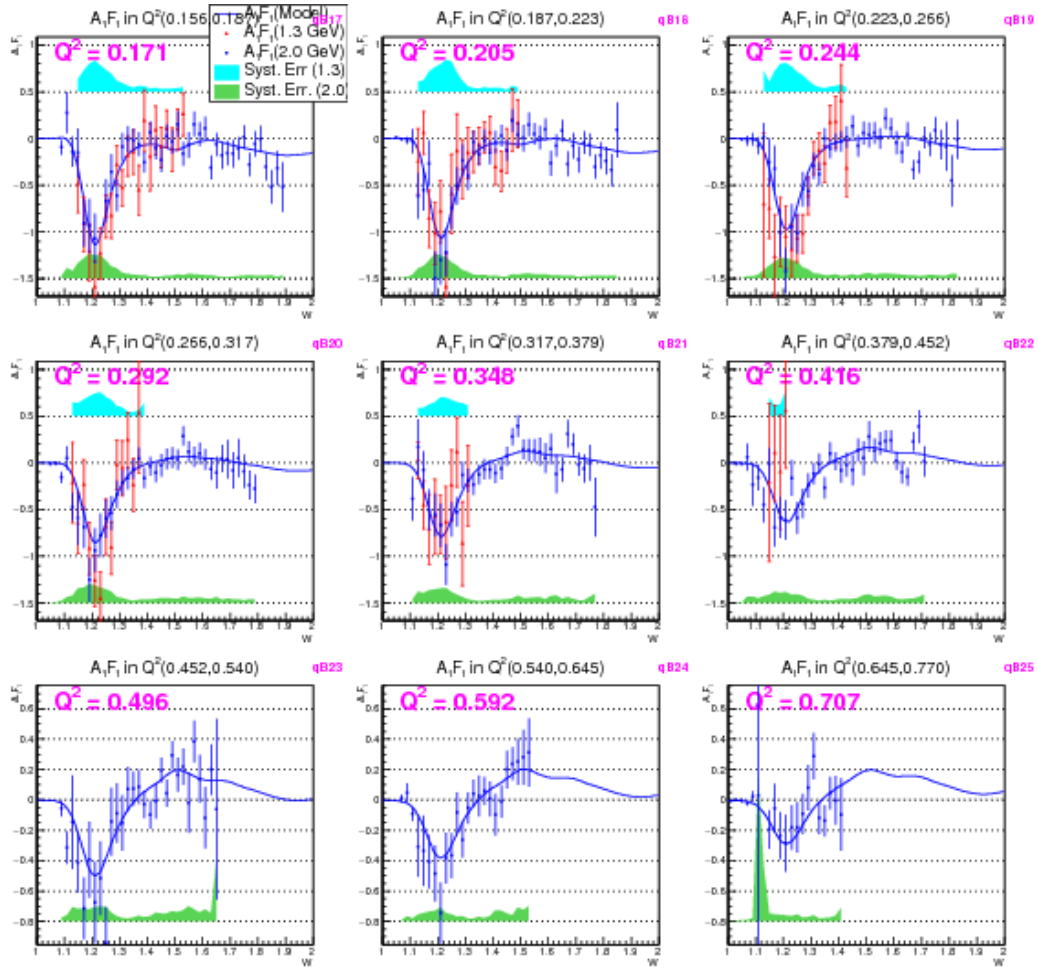


Figure 6.4: Extracted $A_1 F_1$ for deuteron (in the last 9 Q^2 bins (see Fig. 6.3 for the first 12 bins)) from the two different beam energy data sets..

1891 Figs. 6.5, 6.6, 6.7 and 6.8 show the values of g_1 and $A_1 F_1$ and their
 1892 errors after combining the corresponding results from the two different beam
 1893 energies as described in the previous chapter.

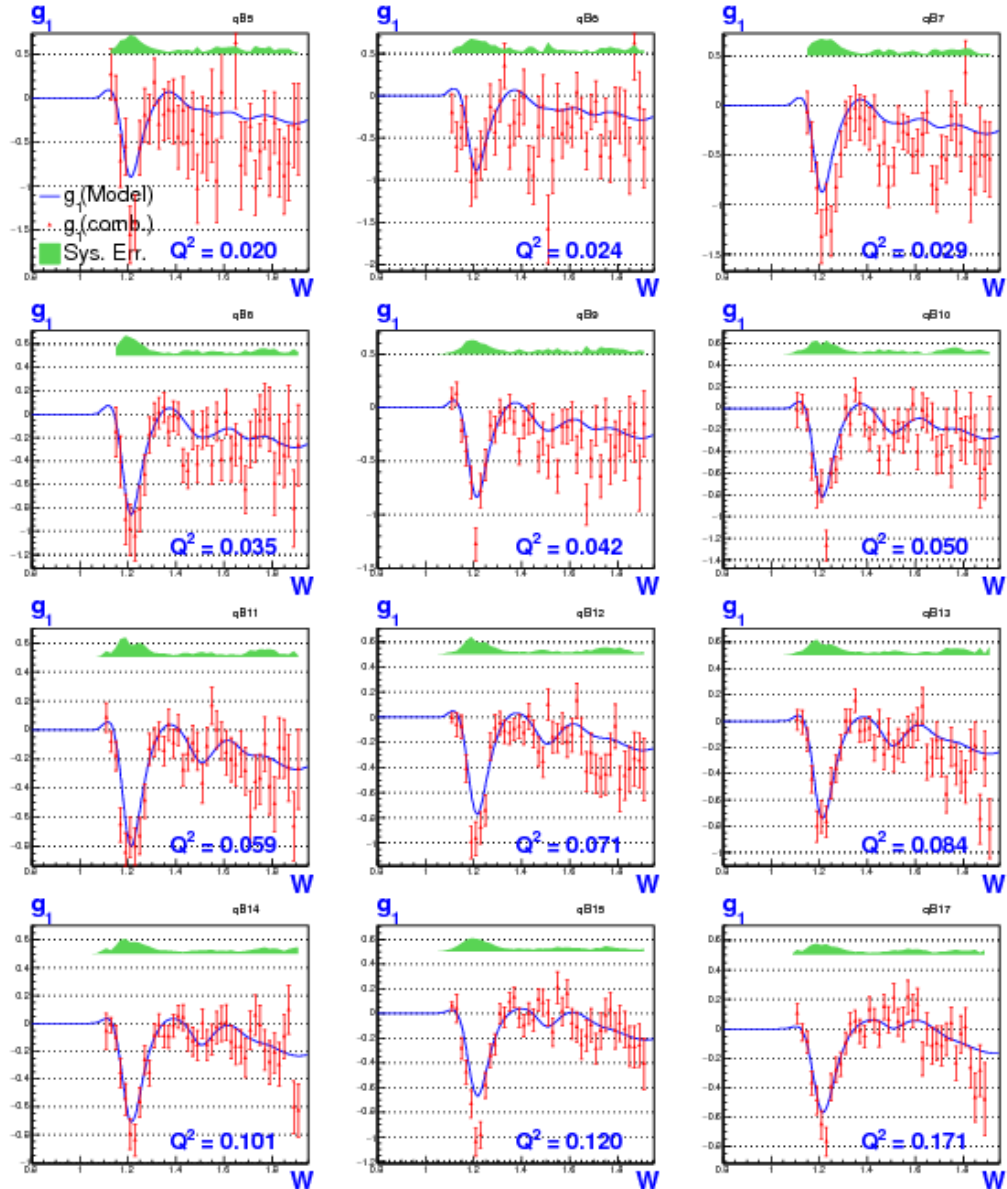


Figure 6.5: Extracted g_1 for deuteron after combining the results from the two beam energies (in the first 12 Q^2 bins). The red data points with error bars in each of the panels are the combined extracted results, the blue continuous line is the used model of g_1 and the green band represents the corresponding total systematic errors.

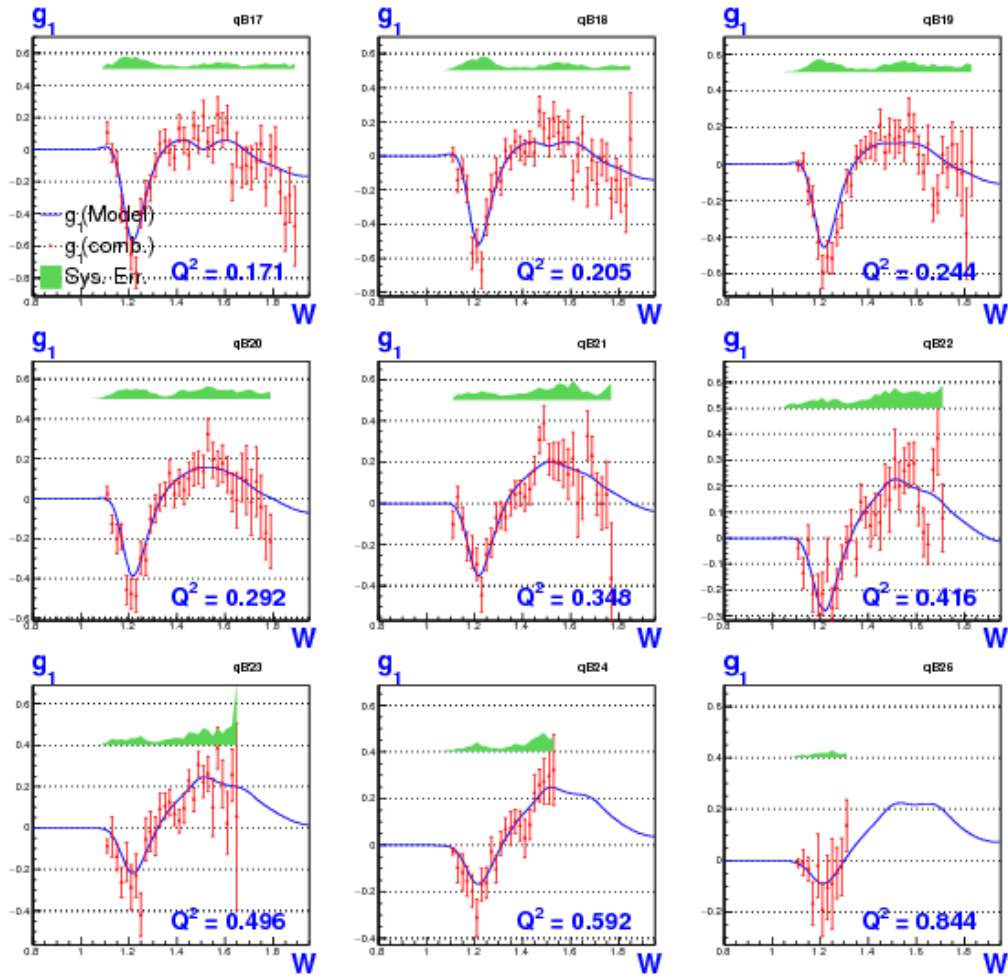


Figure 6.6: Similar plots as in Fig. 6.5 showing the combined results on g_1 in the next 9 Q^2 bins.

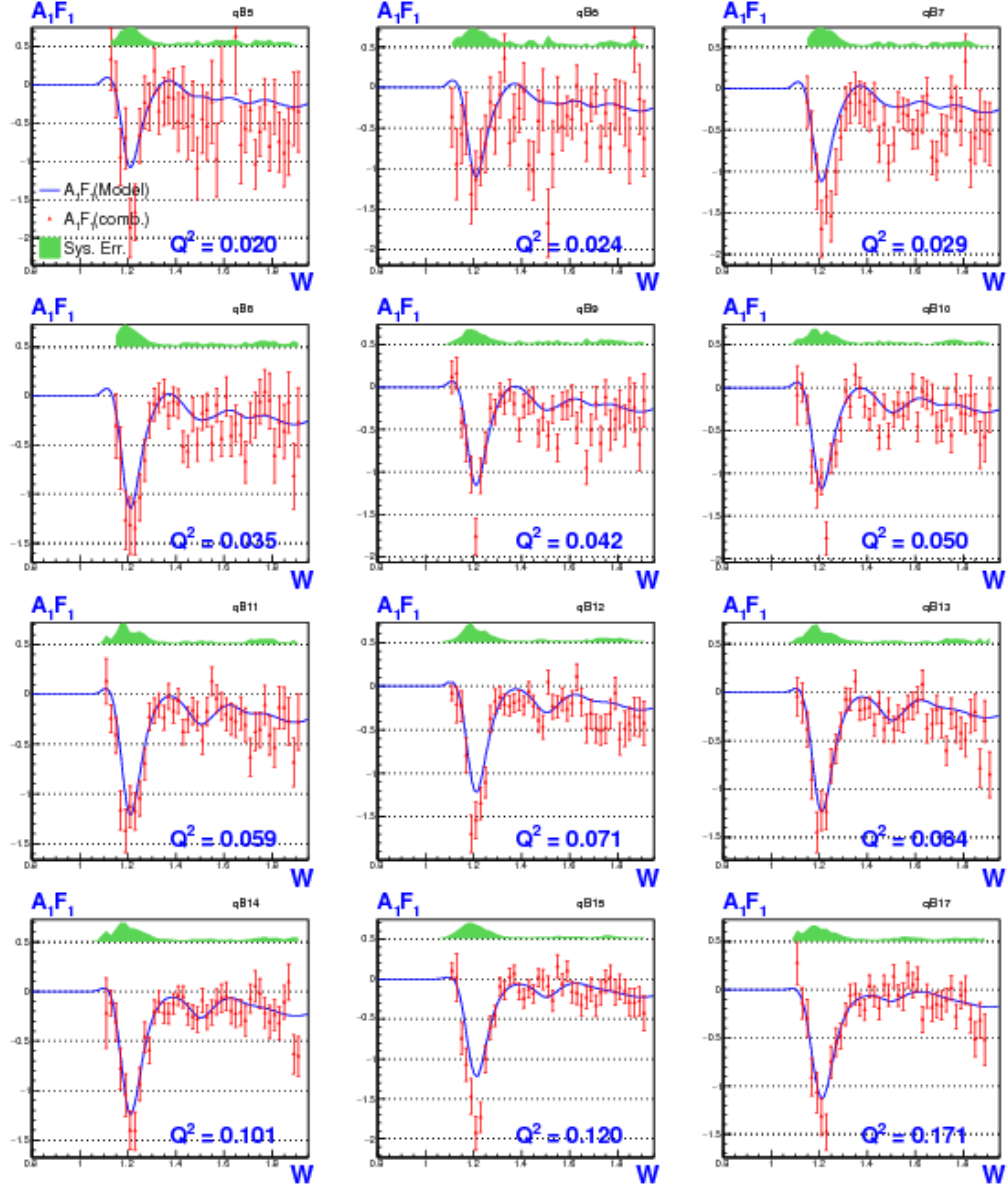


Figure 6.7: $A_1 F_1$ after combining the results from the two beam energies (in the first 12 Q^2 bins). The red data points with error bars in each of the panels are the combined extracted results, the blue continuous line is the used model of g_1 and the green band represents the corresponding total systematic errors.

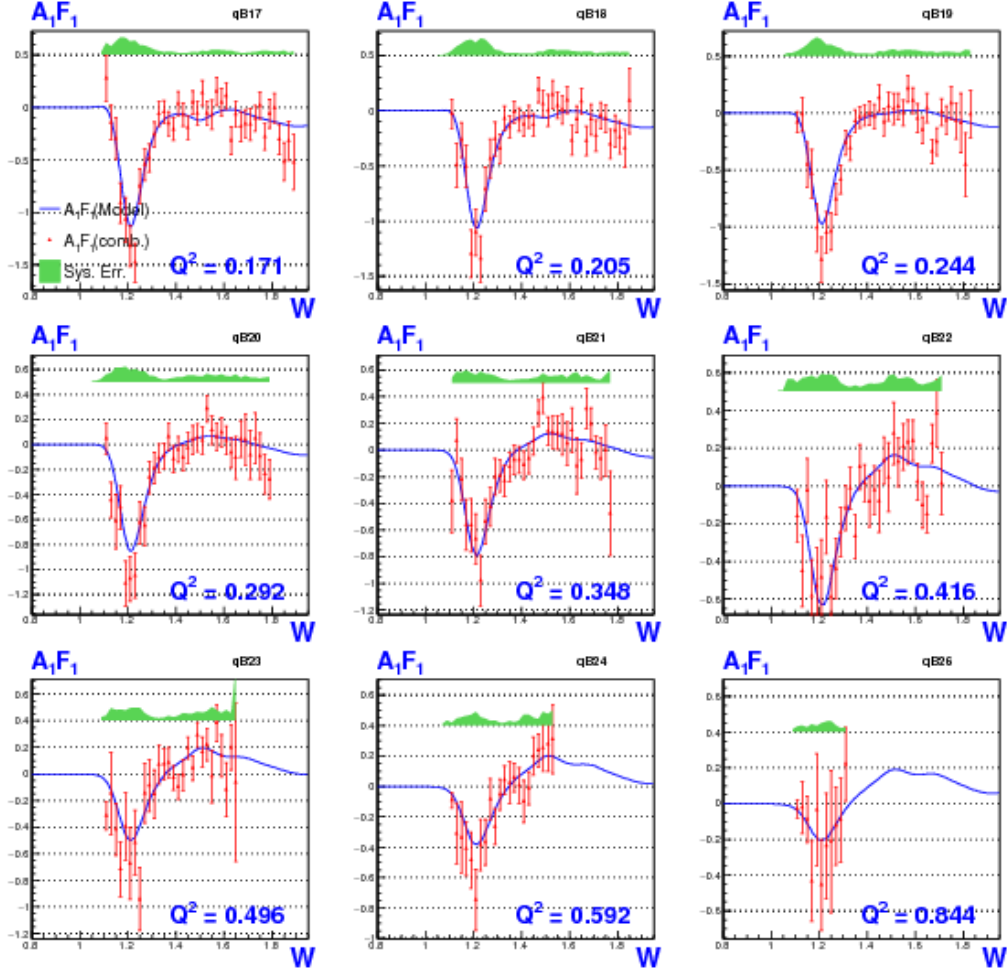


Figure 6.8: Similar plots as in Fig. 6.7 showing the combined results on g_1 in the next 9 Q^2 bins.

1894 **6.2 Moments of Deuteron Spin Structure func-**
 1895 **tions**

1896 Using the measured values of g_1 and A_1F_1 , three integrals were evaluated for
 1897 each of the Q^2 bins in which these data were measured. These integrals have
 1898 been calculated in two ways - using only the new EG4 measurements, and
 1899 adding model contributions to the data for regions not covered by our mea-

surements. The integrals with the model contributions were calculated from $x = 0.001$ to the onset of the resonance region (i.e. to the pion production threshold of $W \approx 1.08$ GeV), dividing the sum into three parts for each Q^2 bin. For example, Γ_1 was evaluated by adding up the product $g_1 \Delta x$ over the following three kinematic regions:

$$\begin{aligned} \Gamma_1(Q^2) &= \int_{x=0.001}^{x(W_{data})} g_1(x, Q^2) dx \quad \text{model} \quad (6.1) \\ &+ \int_{x(W_{data})}^{W=1.15} g_1(x, Q^2) dx \quad \text{data (or model for gaps)} \quad (6.2) \\ &+ \int_{W=1.15}^{W=1.08} g_1(x, Q^2) dx \quad \text{model} \quad (6.3) \end{aligned}$$

where W_{data} indicates the upper edge of the last W bin in which the EG4 data is available in a given Q^2 bin (the W variable was divided into 70 bins of size 20 MeV in the range $W=(0.7,2.1)$ GeV). The first part of the integral as given by Eq. 6.1 is evaluated by using the model values of g_1 and using Δx corresponding to a W bin of size 10.0 MeV (The ΔW is converted to Δx by using $x = Q^2/(Q^2 + W^2 - M^2)$ to evaluate x at the two edges of each W bin and taking the difference.). The second part given by Eq. 6.2 is evaluated similarly but using the EG4 results for g_1 if there is no measurement gap in between. If there is any gap, the same method as in the first part is used to get a model contribution for the gap and added to the data contribution. Lastly, the the third contribution given by Eq. 6.2 again were evaluated from model values (quasi-elastic part turned off from the model in all of these cases) but with finer W bins (1 MeV) because the integrals are very sensitive to the region near the Δ resonance due to the fact that the structure functions show rapid changes in this region. The reason to calculate the third integral using model values rather than data values is to avoid having contributions in the integrals from the quasi-elastic contamination.

The statistical errors are evaluated by adding the statistical error contribution in each W or x bin in quadrature. For example, if the integral is evaluated in a Q^2 bin by calculating the sum $\left(\sum_{W \text{ bins}} g_1 \cdot \Delta x \right)$, then the corresponding statistical error is evaluated by calculating $\sqrt{\sum_{W \text{ bins}} (\sigma g_1)^2 \cdot \Delta x}$. Because the model contribution is assumed to have no statistical uncertainties, the statistical errors in the integrals come solely from the propagation

1928 of the statistical error of the measured g_1 or $A_1 F_1$.

1929 The other two integrals and their errors are evaluated in the same manner,
1930 with g_1 replaced by their corresponding integrands and again calculating the
1931 three parts of the integrals separately.

1932 These integrals are then compared with the latest available predictions
1933 from different theories (mainly χ PT) and phenomenological calculations along
1934 with EG1b or DIS data whenever applicable.

1935 **6.2.1 First moment of g_1 (Γ_1)**

1936 The first integral of interest is the first moment of g_1 i.e., Γ_1 (see Eq. 1.10)
1937 , which was calculated for all Q^2 bins for which the new data are available.
1938 Figs. 6.9 and 6.10 show the two calculations (with and without model in-
1939 put) along with EG1b data and several χ PT and model predictions. One
1940 important observation here is that our measurements provide the only data
1941 points in the very low Q^2 region (i.e for $Q^2 < 0.05 \text{ GeV}^2$) where χ PT is
1942 thought to be able to make rigorous calculations. Therefore, our data will
1943 provide important benchmarks for the future calculations in this kinematics.
1944 Particularly, the latest χ PT prediction by Bernard *et al.* [51] seems to agree
1945 remarkably well in the very low Q^2 region.

1946 While all other higher Q^2 predictions, except that of Ji *et al.*, seem to
1947 be within the uncertainties of our measurements, it can be seen that the
1948 phenomenological predictions of Soffer *et al.* compare slightly better with
1949 data than others (excluding, of course, the Bernard *et al.* prediction).

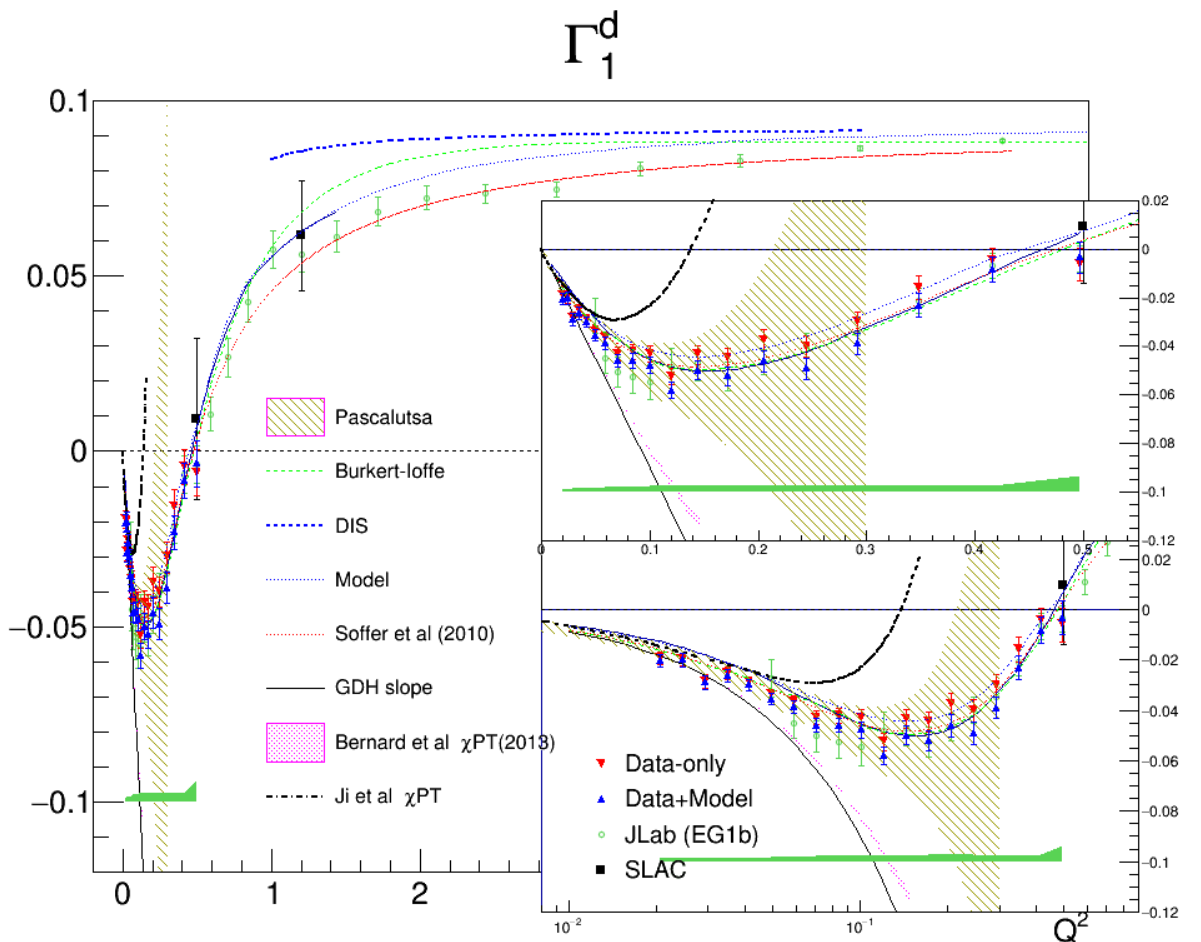


Figure 6.9: Extracted Γ_1 for deuteron compared with some of the past measurements and various theoretical predictions with a linear scale used for Q^2 .

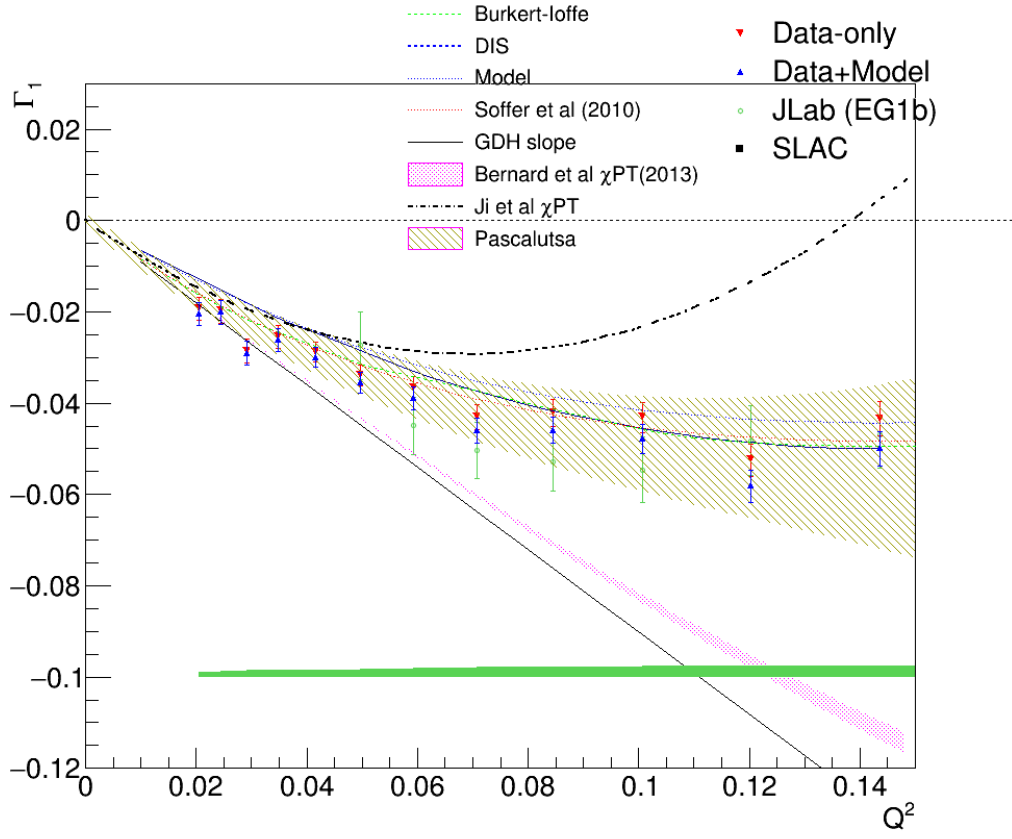


Figure 6.10: Extracted Γ_1 for deuteron compared with some of the past measurements and various theoretical predictions zooming in on the very low Q^2 region.

1950 6.2.2 The extended GDH integral \bar{I}_{TT}

1951 Using the measured values of $A_1 F_1$, the generalized GDH integral $\bar{I}_{TT} =$
 1952 $2M^2/Q^2 \int A_1 F_1(x, Q^2) dx$ was also calculated and compared (see Figs. 6.11
 1953 and 6.12) with the latest χ PT calculation from Bernard *et al.* [51]. We
 1954 can see that at the very low Q^2 , the χ PT prediction and the measurement
 1955 get very close. The χ PT methods determine the higher powers of Q^2 in the
 1956 Taylor expansion of the integral around the photon point $Q^2 = 0$, beyond the
 1957 prediction of the GDH sum rule which determines the lowest order term. Our
 1958 data seem indeed to converge towards the GDH sum rule at our lowest Q^2 .
 1959 However, only one or two higher order terms can be calculated confidently,
 1960 since higher orders require additional (unknown) constants. Therefore, χ PT

¹⁹⁶¹ predictions do reasonably well at ultra-low Q^2 but cannot be expected to
¹⁹⁶² work at the higher Q^2 , where the data show a turn-around and a transition
¹⁹⁶³ towards positive values.

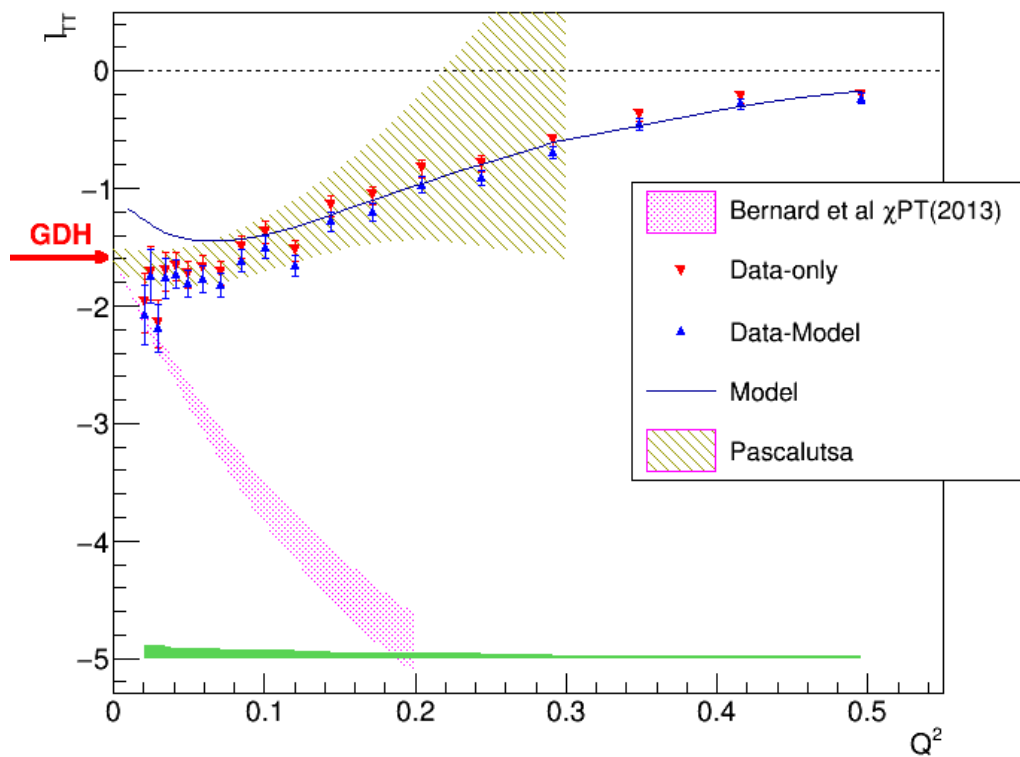


Figure 6.11: Extracted \bar{I}_{tt} for deuteron compared with the used model and a χ PT prediction with a linear scale used for Q^2 .

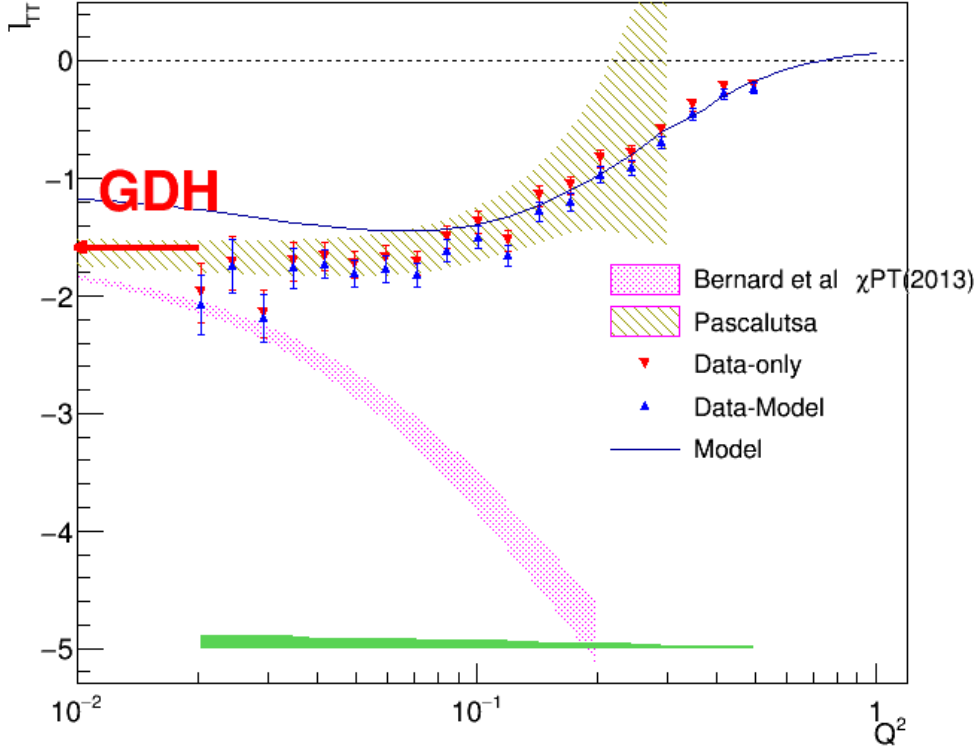


Figure 6.12: Extracted I_{tt} for deuteron compared with the used model and a χ PT prediction with a logarithmic scale used for Q^2 .

1964 6.2.3 The Generalized Forward Spin Polarizability γ_0

1965 Finally, the generalized forward polarizability (as given by Eq. 1.16) for
 1966 the deuteron was also calculated using the measured values of $A_1 F_1$ and
 1967 then compared with various predictions as shown in Figs. 6.13 and 6.14.
 1968 The comparison shows that both χ PT calculations by Bernard *et al.* and
 1969 Kao *et al.* converge with data at the lowest Q^2 bins. However, the χ PT
 1970 calculations by Pascalutsa *et al.* seem to deviate greatly from both the
 1971 current measurement as well as the other χ PT calculations (particularly at
 1972 the very low Q^2 region, indicating that some ingredients might be missing
 1973 from the calculation model). Likewise, the MAID prediction also seems to be
 1974 somewhat off the current results.

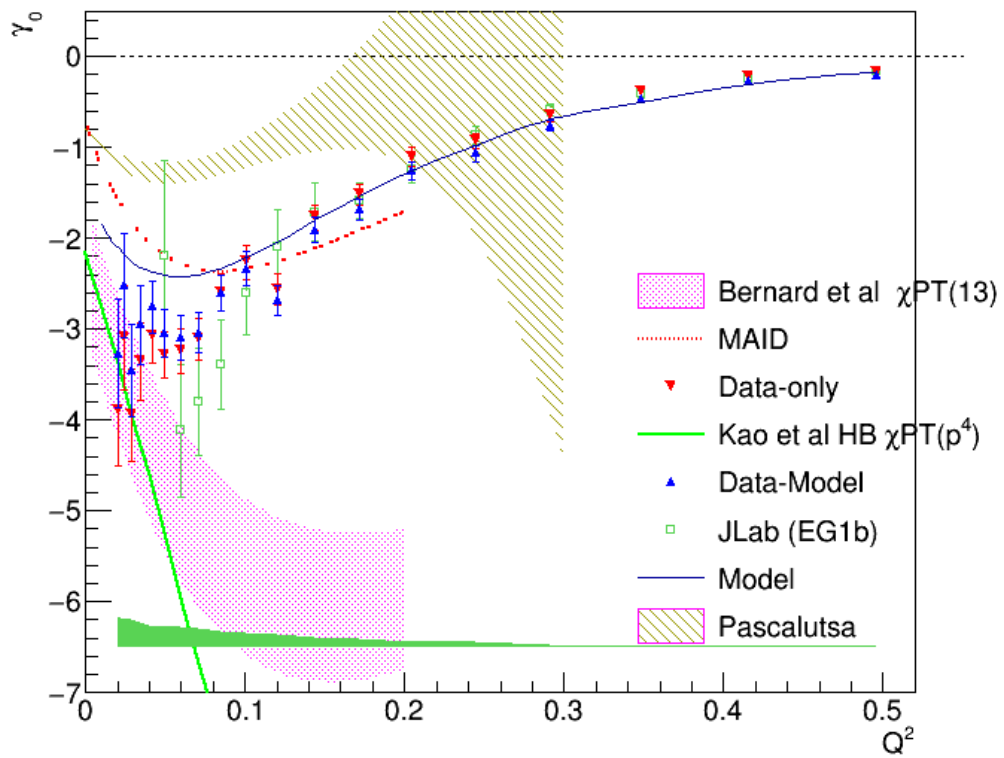


Figure 6.13: Extracted γ_0 for deuteron compared with some of the past measurements and various theoretical predictions with a linear scale used for Q^2 .

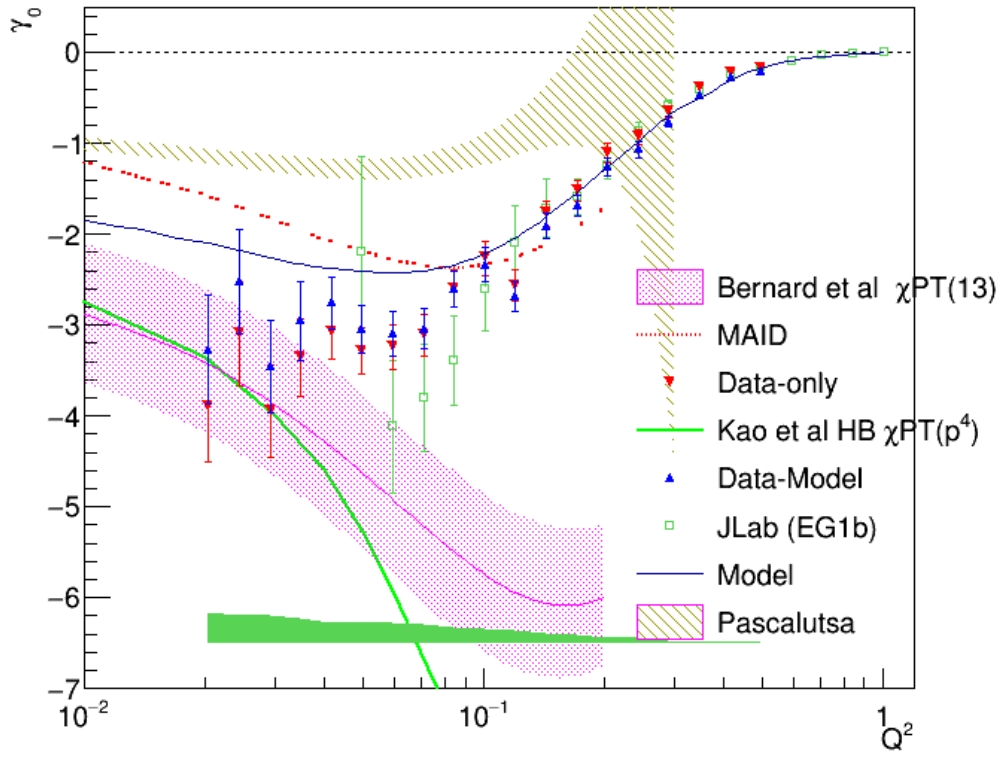


Figure 6.14: Extracted γ_0 for deuteron compared with some of the past measurements and various theoretical predictions with a logarithmic scale used for Q^2 .

¹⁹⁷⁵ **Chapter 7**

¹⁹⁷⁶ **Conclusions**

¹⁹⁷⁷

¹⁹⁷⁸ The very low momentum transfer (Q^2) data from the EG4 experiment
¹⁹⁷⁹ have been analyzed for the helicity dependent inclusive cross section (difference)
¹⁹⁸⁰ for the scattering of longitudinally polarized electrons off longitudinally
¹⁹⁸¹ polarized deuterons (from DNP polarized ND₃ target). The analyzed data
¹⁹⁸² has the kinematic coverage of ($0.02 \text{ GeV}^2 < Q^2 < 0.7 \text{ GeV}^2$) and ($1.08 \text{ GeV} < W < 2.0 \text{ GeV}^2$). Although past measurements from EG1b go as
¹⁹⁸³ low as 0.05 GeV^2 in Q^2 , the new measurements have higher precision (due
¹⁹⁸⁴ to higher statistics and better detection efficiency) in the overlapping region
¹⁹⁸⁵ in addition to new high precision data in the previously unmeasured lower
¹⁹⁸⁶ Q^2 region.
¹⁹⁸⁷

¹⁹⁸⁸ The new deuteron data were used to extract the deuteron's spin structure
¹⁹⁸⁹ function g_1 by comparing the experimental data with simulated data
¹⁹⁹⁰ produced by using a realistic cross section model for the deuteron under similar
¹⁹⁹¹ kinematic conditions. The newly extracted data pushes the lower limit
¹⁹⁹² on Q^2 in the resonance region with reduced systematic and statistical
¹⁹⁹³ uncertainties that will contribute greatly to the world data set. It is observed
¹⁹⁹⁴ that the data from two beam energies give results that are in good agreement
¹⁹⁹⁵ wherever they overlap. The low Q^2 results clearly show resonance structure
¹⁹⁹⁶ in the region $W \leq 2.0$ which smooths out as Q^2 becomes larger. In particular,
¹⁹⁹⁷ the Δ -resonance shows a strongly and consistently negative signal
¹⁹⁹⁸ at all Q^2 , but the second resonance region (around $W=1.5 \text{ GeV}$) shows a
¹⁹⁹⁹ rather rapid transition of g_1 (or cross section) from strongly negative values
²⁰⁰⁰ at low Q^2 to clearly positive values at high Q^2 . This observation in the sec-
²⁰⁰¹ ond resonance region is not well described by the model because the model

2002 is not constrained in the region due to the lack of experimental data (up to
2003 now) and indicates that the spin-flip helicity amplitude $A_{\frac{3}{2}}^T$ dominates the
2004 cross section at low Q^2 while the non-flip amplitude $A_{\frac{1}{2}}^T$ becomes stronger at
2005 higher Q^2 .

2006 The product $A_1 F_1$ of the virtual photon asymmetry A_1 and the unpo-
2007 larized structure function F_1 was also extracted from the same data and
2008 method. The extracted results on g_1 and $A_1 F_1$ were then used to evaluate
2009 three important moments - the first moment Γ_1^d of g_1 , the generalized GDH
2010 integral \bar{I}_{TT}^d and the generalized forward spin polarizability γ_0^d - in each of
2011 the Q^2 bins in which the new g_1 and $A_1 F_1$ have been extracted. The new low
2012 Q^2 measurements of the moments evaluated both with and without model
2013 inputs for the unmeasured kinematic regions were then compared with vari-
2014 ous χ PT calculations, phenomenological predictions and past measurements,
2015 particularly the EG1b or DIS data whenever applicable.

2016 The EG4 results provide the only data points in the very low Q^2 region
2017 (i.e for $Q^2 < 0.05$ GeV 2) where χ PT is thought to be able to make rigorous
2018 calculations. The high precision data will provide important benchmarks for
2019 the future calculations in this kinematics. In the case of the first moment Γ_1^d ,
2020 the EG4 results show remarkable agreement with the latest χ PT prediction
2021 by Bernard *et al.* [51] in the very low Q^2 region. The phenomenological
2022 predictions which have much larger Q^2 coverage also seem to agree within
2023 the uncertainties of our measurements, with the predictions of Soffer *et al.*
2024 showing slightly better comparison than others. Likewise, the very low Q^2
2025 results of the generalized GDH integral \bar{I}_{TT} are indeed observed to converge
2026 towards the GDH sum rule and thus getting very close to the χ PT predictions
2027 by Bernard *et al.* [51]. Finally, the generalized forward polarizability (γ_0^d)
2028 for the deuteron calculated from the EG4 data and the χ PT calculations
2029 by Bernard *et al.* and Kao *et al.* seem to converge at the lowest Q^2 bins.
2030 However, the χ PT based predictions from Pascalutsa *et al.* and the MAID
2031 prediction seems to be well off the current results.

2032 The deuteron data in combination with the EG4 proton data taken un-
2033 der similar conditions (currently being analyzed by another collaborator and
2034 results expected to come very soon) will be useful in extracting neutron
2035 quantities in near future, which is valuable because of the unavailability
2036 of the free neutron targets. Moreover, due to the complexities of the nu-
2037 clear medium effects, neutron data from deuteron will be very important to
2038 enhance confidence in similar neutron results extracted from other nuclear

2039 targets particularly ${}^3\text{He}$.

2040 The work presented in this analysis has improved our understanding of
2041 the field of nucleon spin structure and contributed to more solid foundation
2042 for future advancements. The new data on spin structure functions will help
2043 various χ PT calculations and phenomenological models such as MAID to
2044 better constrain their parameters enabling them to make better predictions in
2045 the future. With the availability of the high precision data in the previously
2046 (largely) unmeasured region that has the potential to help constrain the
2047 theories and models, it is hoped that a unified description of spin structure
2048 functions over all kinematic regions will be possible in future.

2049

Bibliography

- 2050 [1] S.E. Kuhn. Nucleon Structure Functions: Experiments and Models. In *Proceedings of the 12th Annual HUGS at CEBAF*, June 1997. Article
2051 based on six lectures on the subject during the 1997 Hampton University
2052 Graduate Summer School.
- 2053 [2] J.J. Aubert et al. The ratio of the nucleon structure functions {F2N} for iron and deuterium. *Physics Letters B*, 123(34):275 – 278, 1983.
- 2054 [3] Kurt Gottfried. Sum rule for high-energy electron-proton scattering. *Phys. Rev. Lett.*, 18:1174–1177, Jun 1967.
- 2055 [4] M. Arneodo et al. Reevaluation of the gottfried sum. *Phys. Rev. D*, 50:R1–R3, Jul 1994.
- 2056 [5] J. Ashman and other. A measurement of the spin asymmetry and determination of the structure function g_1 in deep inelastic muon-proton scattering. *Physics Letters B*, 206(2):364 – 370, 1988.
- 2057 [6] O. Piguet, G. Pollak, and M. Schweda. The Cancellation of Nonlocal Divergences in Light Cone Theories. *Nucl.Phys.*, B328:527, 1989.
- 2058 [7] K. G. V. G. Dharmawardane. *Spin Structure Functions of the Deuteron Measured with CLAS in and above the Resonance region*. PhD thesis, Old Dominion University, May 2004.
- 2059 [8] D.J. Gross and F. Wilczek. Ultraviolet behavior of non-abelian gauge theories. *Phys. Rev. Lett.*, 30(26):1343–1346, 1973.
- 2060 [9] J. P. Chen and others. The GDH Sum Rule and the Spin Structure of ^3He and the Neutron using Nearly-Real Photons. JLab Hall A Proposal, 1997. PR97-110.

- 2073 [10] S.E. Kuhn, J.-P. Chen, and E. Leader. Spin Structure of the Nucleon -
 2074 Status and Recent Results. *Prog.Part.Nucl.Phys.*, 63:1–50, 2009.
- 2075 [11] S. Gerasimov. *Yad. Fiz.*, 2:598, 1965.
- 2076 [12] S. D. Drell and A. C. Hearn. Exact sum rule for nucleon magnetic
 2077 moments. *Phys. Rev. Lett.*, 16:908–911, May 1966.
- 2078 [13] H. Dutz et al. First measurement of the gerasimov-drell-hearn sum rule
 2079 for ${}^1\text{H}$ from 0.7 to 1.8 gev at elsa. *Phys. Rev. Lett.*, 91:192001, Nov 2003.
- 2080 [14] H. Dutz et al. Measurement of helicity-dependent photoabsorption
 2081 cross sections on the neutron from 815 to 1825 mev. *Phys. Rev. Lett.*,
 2082 94:162001, Apr 2005.
- 2083 [15] Dieter Drechsel and Lothar Tiator. The Gerasimov-Drell-Hearn sum rule
 2084 and the spin structure of the nucleon. *Ann.Rev.Nucl.Part.Sci.*, 54:69–
 2085 114, 2004.
- 2086 [16] S. Hoblit et al. Measurements of $hd(\gamma, \pi)$ and implications for the conver-
 2087 gence of the gerasimov-drell-hern integral. *Phys. Rev. Lett.*, 102:172002,
 2088 Apr 2009.
- 2089 [17] M. Anselmino, B.L. Ioffe, and E. Leader. On Possible Resolutions of the
 2090 Spin Crisis in the Parton Model. *Sov.J.Nucl.Phys.*, 49:136, 1989.
- 2091 [18] A. Deur et al. Measurement of the Gerasimov-Drell-Hearn Integral at
 2092 low Q^2 on the Neutron and Deuteron. CLAS Proposal, December 2006.
 2093 PR06-017.
- 2094 [19] Matthias Burkardt. The $g(2)$ Structure Function. *AIP Conf. Proc.*,
 2095 1155:26–34, 2009.
- 2096 [20] M. Anghinolfi and others. The GDH Sum Rule with Nearly-Real Pho-
 2097 tons and the Proton g_1 Structure Function at Low Momentum Transfer.
 2098 CLAS Proposal, 2003. PR03-006.
- 2099 [21] D. Drechsel, B. Pasquini, and M. Vanderhaeghen. Dispersion relations
 2100 in real and virtual Compton scattering. *Phys. Rept.*, 378:99–205, 2003.
- 2101 [22] N. Guler. *Spin Structure of the Deuteron*. PhD thesis, Old Dominion
 2102 University, December 2009.

- 2103 [23] The eg4 wiki. https://clasweb.jlab.org/rungroups/eg4/wiki/index.php/Main_Page. [Online; accessed 22-Sep-2013].
- 2104
- 2105 [24] R. De Vita. *Measurement of the Double Spin Asymmetry in π^+ electro-*
2106 *production with CLAS*. PhD thesis, University of Genova, 2000.
- 2107 [25] M. Osipenko, A. Vlassov and M. Taiuti. A vxibus based trigger for the
2108 clas detector at cebaf. Technical Report CLAS NOTE 2004-020, JLAB,
2109 2004.
- 2110 [26] X. Zheng. CLAS EG4 Analysis Note - 'Double- and Target Spin Asym-
2111 metries in Pion Electro-production from Polarized NH₃ Targets. 2015.
- 2112 [27] K.S. Egiyan. Determination of electron energy cut due to the clas ec
2113 threshold. Technical Report CLAS-NOTE-1999-007, JLAB, 1999.
- 2114 [28] The eg4 collaboration. <http://clasweb.jlab.org/shift/eg4/>. [On-
2115 line; accessed 22-Sep-2013].
- 2116 [29] S. E. Kuhn. Private communications, 2013.
- 2117 [30] P. Bosted. Private communications, 2010.
- 2118 [31] Beam energies during the eg4 run. http://www.jlab.org/deurpam/e03006/eg4_energy.pdf. [Online; accessed 05-Jan-2017].
- 2119
- 2120 [32] A. Klimentko and S. Kuhn . Momentum Corrections for E6. Technical
2121 Report CLAS-Note 2003-005, JLAB, 2003.
- 2122 [33] William R Leo. *Techniques for nuclear and particle physics experiments: a how-to approach*. Springer, 1994.
- 2123
- 2124 [34] R. G. Fersch. *Measurement of Inclusive Proton Double-Spin Asymme-*
2125 *tries and Polarized Structure Functions*. PhD thesis, The College of
2126 William and Mary, August 2008.
- 2127 [35] P. Bosted. Pair-symmetric and pion backgrounds for eg1b. Technical
2128 Report CLAS-NOTE-2004-005, JLAB, 2004.
- 2129 [36] S. P. Phillips. http://clasweb.jlab.org/rungroups/eg4/wiki/index.php/October_14%2C_2011. [Online; accessed 22-Sep-2013].
- 2130

- 2131 [37] Peter Bosted. Nh3 correction for nd3 target: Eg1-dvcs technical note
 2132 17. Technical report, November 2011.
- 2133 [38] Suman Koirala. EG1-DVCS Part-C Target Contamination. Technical
 2134 report, May 2012.
- 2135 [39] S.E. Kuhn and K. Adhikari. Data Analysis for EG4 - extraction of g_1
 2136 from data. 2013.
- 2137 [40] K. Abe et al. Measurements of the proton and deuteron spin structure
 2138 functions g_1 and g_2 . *Phys. Rev. D*, 58:112003, Oct 1998.
- 2139 [41] T.V. Kuchto and N.M. Shumeiko. Radiative effects in deep inelastic
 2140 scattering of polarized leptons by polarized nucleons. *Nuclear Physics B*,
 2141 219(2):412–436, 1983.
- 2142 [42] L. W. Mo and Y. S. Tsai. Radiative corrections to elastic and inelastic
 2143 ep and up scattering. *Rev. Mod. Phys.*, 41:205–235, Jan 1969.
- 2144 [43] P.E. Bosted and M.E. Christy. Empirical fit to inelastic electron-
 2145 deuteron and electron-neutron resonance region transverse cross-
 2146 sections. *Phys.Rev.*, C77:065206, 2008.
- 2147 [44] R. G. Fersch et al. Precise Determination of Proton Spin Structure
 2148 Functions at Low to Moderate Q^2 with CLAS. To be published, October
 2149 2012.
- 2150 [45] N. Guler et al. Precise Determination of Deuteron and Neutron Spin
 2151 Structure Functions at Low to Moderate Q^2 with CLAS. To be pub-
 2152 lished, October 2013.
- 2153 [46] Yonatan Kahn, W. Melnitchouk, and Sergey A. Kulagin. New method
 2154 for extracting neutron structure functions from nuclear data. *Phys. Rev.*,
 2155 C79:035205, 2009.
- 2156 [47] M. Holtrop. GSIM: CLAS GEANT Simulation. http://nuclear.unh.edu/~maurik/gsim_info.shtml. [Online; accessed 22-Sep-2013].
- 2158 [48] Brooks, W. *CLAS - A large acceptance spectrometer for intermediate*
 2159 *energy electromagnetic nuclear physics*. Jun 1999.

- 2160 [49] B. Dey. *Differential cross section and polarization extractions for $\gamma p \rightarrow$*
2161 *$K^+ \Sigma^0$ and $\gamma p \rightarrow \phi p$ using CLAS at Jefferson Lab, towards a partial wave*
2162 *analysis in search of missing baryon resonances.* PhD thesis, Carnegie
2163 Mellon University, July 2011.
- 2164 [50] J. Zhang. *Exclusive π^- Electro-production from the Neutron in the Res-*
2165 *onance Region.* PhD thesis, Old Dominion University, May 2010.
- 2166 [51] Veronique Bernard, Evgeny Epelbaum, Hermann Krebs, and Ulf-G.
2167 Meissner. New insights into the spin structure of the nucleon. *Phys.*
2168 *Rev.*, D87:054032, 2013.

₂₁₆₉ **Appendix A**

₂₁₇₀ **FFREAD cards used by GSIM**

Table A.1: Some of the ffreac cards & their values which are used as GSIM input parameters.

Cards	Values
MAGTYPE	2
MAGSCALE	-0.5829 0.0 (for 1.337 GeV)
MAGSCALE	-0.3886 0.0 (for 1.993 GeV)
GEOM	'ALL'
NOMC	'EC' 'SC' 'CC' 'DC'
NOGEOM	'MINI' 'ST' 'TG2' 'TG' 'SOL'
NOGEOM	'PTG' 'FOIL'
NOMATE	'PTG' 'FOIL'
PTGIFIELD	1
TMGIFIELD	1
TMGIFIELDM	1
TMGFIELDM	51.0
TMGSCALE	0.979
PTGMAXRAD	300.0
MGPOS	0.0 0.0 -100.93
BAFF	3. 9. 165.3 9. 180.5 9. 195.8
RUNG	50556
AUTO	1
KINE	1